Faculty of Mathematics and Physics
Charles University, Prague

Doctoral thesis

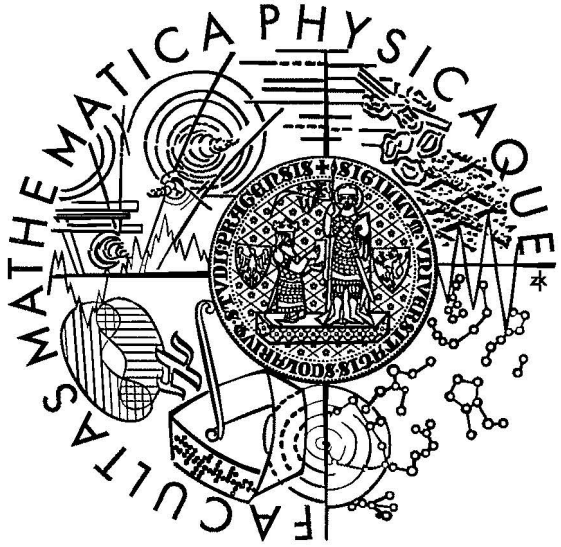

Martina Boháčová

Pierre Auger Fluorescence Detector Study of the Air Fluorescence

Advisor RNDr. Jiří Grygar CSc.

Institute of Physics
Academy of Sciences of the Czech Republic

PRAGUE 2006

"So remarkably has science extended our powers of perception that we have virtually acquired a set of new senses. As a matter of fact, the sense organs with which the nature has provided us are useful in a very limited domain; and indeed many kinds of phenomena escape us altogether, since they produce no perceptible effects."

PIERRE AUGER

Acknowledgment

First of all I would like to thank Jan Řídký and Jiří Grygar for giving me this exclusive scientific opportunity to be part of a top class experiment - the Pierre Auger Project.

I am grateful to Paolo Privitera for conducting my work on the AIRFLY experiment and for his kind advice during the thesis preparation.

I thank my colleagues Petr Trávníček, Michael Prouza and Radek Šmída for providing a friendly and inspiring environment to work in.

I am deeply indebted to Petr Tobiška, whose expertise was of immense help and whose tremendous patience and boundless support I shall never be able to pay off.

Finally I would like to thank my parents for the diligence and perseverance that they instilled in me. This proved to be a crucial prerequisite for this work to become a reality.

Contents

1 Introduction

Cosmic rays (or more appropriately cosmic particles) have been studied for the past hundred years, yet many questions regarding their nature and origin remain unsolved. They span many orders of magnitude in energy and flux.

The all particle differential spectrum of cosmic ray flux shown in Fig. 1 can be described by a broken power law. Up to about 4×10^{15} eV the spectral index α is equal to 2.7. Then, a steepening, called knee occurs, which could be associated with the fact that some accelerating mechanisms have reached their maximum energy or that the galactic magnetic field is not strong enough to detain particles of higher energies. The flux at this point reaches about 1 particle per m^2 per year. The spectral index above the knee rises about 3. Another feature appears around 5×10^{18} eV, called the ankle of the spectrum. It is being interpreted as the onset of cosmic-ray sources of an extra Galactic origin. The flux of cosmic particles around the ankle amounts to only 1 particle per km^2 per year.

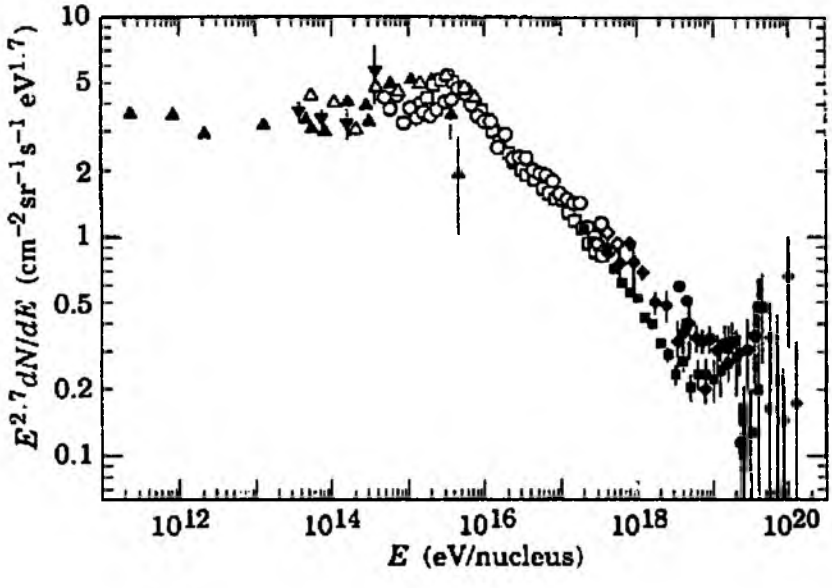

Fig. 1. *The all-particle differential energy spectrum [PDG04]. The spectrum was multiplied by the factor $E^{2.7}$ to enhance the observed structure.*

Above tens of TeV the flux of cosmic rays becomes insufficient for direct observations. However, the atmosphere can be used as a calorimeter for indirect observations on the ground. In the following, only the high energy part of the spectrum will be considered,

i.e. around and above the ankle. The cosmic rays above 10^{18} eV are usually denoted as Ultra High Energy Cosmic Rays (UHECR).

Two main methods are used to observe UHECR: secondary particle detection on the ground using an array of particle detectors and a fluorescence technique, where the light produced by secondary particles in the atmosphere is observed.

Pierre Auger Observatory represents a new generation of cosmic ray experiments featuring a large detecting area and combining the two techniques to significantly improve the measurement precision. The model dependence of the surface detector technique can be largely reduced using the fluorescence detector calorimetric energy determination, which in turn relies on the precise knowledge of the air fluorescence yield. In the framework of this major experiment arose the need for revision of the parameters of the air fluorescence technique leading to the realization of the experiment AIRFLY (AIR FLuorescence Yield).

1.1 Thesis overview

The thesis is dedicated to measurements of the air fluorescence yield in dependence on the atmospheric conditions, which is a key parameter in the energy reconstruction of cosmic ray experiments using the atmospheric fluorescence technique.

The first part presents a review of aspects of cosmic ray detection, focused on the UHECR. It begins with the history of cosmic ray observations, followed by description of the possible sources of UHECR. The next part deals with atmospheric shower formation. Chapter 5 gives a brief account on the Pierre Auger Observatory design and function, followed by the description of the air fluorescence technique.

The second part is dedicated to the experiment AIRFLY. It starts with a brief theory of the fluorescence process followed by a description of the experimental setup and the detector response simulations. Chapter 10 gives description of auxiliary measurements, which are than used in chapter 11, dedicated to the main results of the experiment.

The last chapter summarizes major achievements and outlines future prospects of the experiment.

CGS units are used whenever appropriate – according to common practice.

2 Early days of cosmic ray research

At the beginning of the 20th century scientists were perplexed by omnipresent radiation that was discharging electroscopes even out at sea, far from all radioactive materials. No matter how they shielded their detectors, some radiation still penetrated indicating a new type of radiation of immense power of an unknown origin. In 1910 a Jesuit priest Theodor Wulf brought his improved model of electroscope to the top of the Eiffel Tower and there, 300 m above the ground, measured 3.5 ions/cm^3, about a half of what was measured on the ground. If the radiation was gamma, the most penetrating radiation known at that time, originating on the Earth surface, it should decrease by half already at the height of 80 metres [Ros66]. Theodor Wulf came with the idea of a cosmic origin of the radiation and suggested to prove it with the aid of balloons. Already Gockel after his balloon flights in 1910 pointed out that the penetrating radiation not only did not disappear above 1 km of altitude but it even started to grow. He suggested two explanations - either the radiation originates in the atmosphere itself or it is coming from the outer space [Goc11].

Austrian scientist Victor Hess made ten ascents in 1911–13 and reached the height of 5300 m. Part of his electroscopes were airtight so the speed of discharging could not be affected by changed air pressure. His results confirming Gockel's observations were published in [Hes12]. Hess concluded that the easiest explanation would be, that the radiation is originating in the outer space, enters the atmosphere and diminishes as it passes towards the ground. His argument was later further strengthened by Kohlhöster at the altitude of 9 km.

For the Czech reader it is interesting to note that, as Hess was taking off from Vienna, he often landed in different parts of Bohemia or Moravia. Moreover, the highest and the most important flight was started from Ústí nad Labem (Aussig an der Elbe, northern Bohemia) and the hydrogen filled balloon was called "Böhmen". In Vienna only coal-gas was available with far less lifting power.

However, the cosmic origin of the radiation was yet far from being established - the atmospheric origin was not convincingly excluded and the War time had interrupted the observations.

Ten years later Robert Millikan's group at Caltech developed an electroscope capable of recording measurements on a film without the need of a human attendance. This device in an unmanned balloon could reach much higher altitudes. Millikan doubted Hess's claim

about extraterrestrial origin of the radiation and his measurements of a decrease in higher layers of atmosphere were again suggesting the atmospheric origin (extensive air showers were proposed much later).

Fig. 2. *Victor Hess after one of his balloon flights. The person with a hat to the very right is Jara Cimrman who happened to be passing his summer vacations near Pieskow [Fie66].*

The convincing argument came in 1925 when Millikan was able to measure the penetrating power of this radiation in a lake 15 m deep and realized that there were rays capable to traverse the atmosphere several times over. He came with the name 'cosmic radiation' and in 1926 even with his own theory of its origin. He believed it to be quanta gamma arising from nucleosynthesis in stars. A personal account of this era is given in Millikan's book [Mil47].

In 1929, the new invention – Geiger-Müller counter, brought the possibility of more precise measurements. Electrometers were just about capable of demonstrating the presence of the low intensity radiation. The new device could detect each particle separately. Walther Bothe and Werner Kolhöster placed two of the counters one above the other and thus were capable to measure the moment of discharge with precision of 0.01 s. They found surprisingly many coincidences. To cause a discharge in both detectors, the quantum gamma would have to give enough energy to two electrons to trigger each of them. The probability of this is quite low. Another possibility was that the gamma knocks an electron hard enough to pass through both detectors. To rule out the latter possibility, they inserted a golden block between the counters. 75 % of rays were still firing both counters. The next experiment with three counters excluded the possibility of accidental coincidences or multiple Compton scattering. The researchers were forced to conclude that the same highly penetrating charged particle passes the detectors. According to their knowledge of ionization losses the energy was estimated to 1 GeV.

The results inspired Italian physicist Bruno Rossi [Ros66]. He placed three detectors in a triangle so that a single particle could not pass through all of them and he placed a lead shielding above the apparatus. By measuring the coincidences he proved that cosmic ray particles interact in a medium and produce secondary particles capable of ionizing the air. The result was fully appreciated with the first pictures of showers from cloud

chambers. Rossi went on to study cosmic rays in detail. His best known measurement is the dependence of the number of coincidences on the thickness of inserted lead layer in which the shower was produced.

Time resolution of the devices affects strongly the number of coincidences. Increasing the number of G-M counters lowers the probability of accidental coincidences. A certain number of coincidences was recorded even if the shielding was removed. After several measurements Pierre Auger in 1938 found out that origin of these coincidences cannot be accidental and that they must be caused by showers of secondary particles produced in the atmosphere [Aug38]. Soon after the showers were seen on photographs from cloud chambers.

Further investigation of cosmic rays was aimed at global characteristics. As geomagnetic field affects the trajectories of charged particles, the intensity of radiation should change with latitude. At late twenties Millikan was trying to measure this difference but without success. This was confirming his first idea that the cosmic particles are neutral. Carl Störmer tried to calculate the influence of the earth magnetic field on the incident cosmic rays. Determining the trajectories of particles coming from different directions, he was trying to explain a remarkable phenomena seen sometimes in the northern sky, Aurora Borealis. He was right in supposing that they are caused by charged particles from the Sun eruptions but he did not know that the geomagnetic field curves their trajectories so that they may arrive from completely the opposite direction.

However, his calculations were correctly describing the trajectories of higher energy particles from more distant sources. He found that there are cones in which all the directions are forbidden. The apex angle of the cone depends on the arrival latitude of the particle as well as on its energy. This phenomenon is called the east-west effect. Compton verified this effect by further measurements in 1933-36 [Ros66]. As most of the particles were coming from the west the dominance of positively charged particles was inferred. Apart from this the latitude effect is observed which is caused by charged particles spiraling along the lines of force of the geomagnetic field. As a consequence more particles are observed on poles. Also, particles of lower energy can not reach the atmosphere of lower latitudes so that relative intensity of cosmic rays is different for different places on earth. Though secondary particles which are produced with lower energy obscure a bit these effects, the fact that they do not wipe it out completely, indicates that secondary particles follow closely the arrival direction of the primary particle.

2.1 Boom of particle physics

Investigation of precise composition as well as the processes employed in cosmic radiation meant a real boom for particle physics.

In his further measurement Rossi found a strong dependence of the number of coincidences on the material of shielding. Ionization and Compton scattering, which were the processes believed to be responsible for the energy losses were almost independent of the proton number of the material. The new process, called bremsstrahlung, was already known from electromagnetic theory of radiation but no great importance was attached to it. Bethe and Heitler [Bet34] recalculated this phenomenon with relativistic corrections of quantum theory and proved that bremsstrahlung is dominant in high energies.

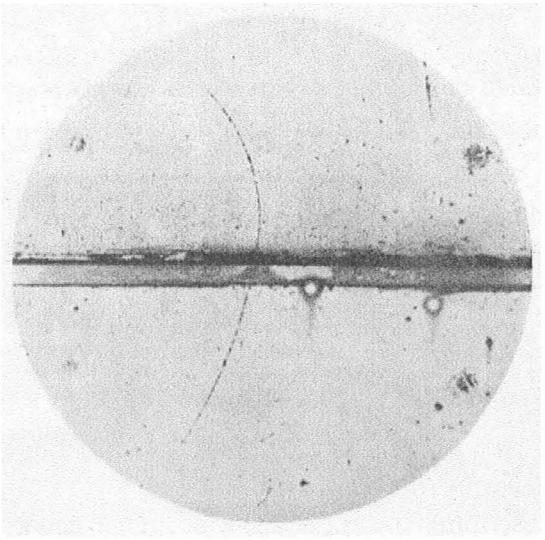

Fig. 3. *First picture of a positron from a cloud chamber*

In 1933 Anderson [And33] noticed that a part of positively charged cosmic ray particles has mass close to that of electron and assumed that it could be the particle predicted by Dirac — positron. Cloud chamber photographs confirmed yet another of Dirac's theories that quantum gamma of high enough energy may interact with the environment and produce electron-positron pair. The two effects, creation of a photon by a charged particle via bremsstrahlung and creation of a pair of charged particles from this photon, were used by Bethe and Heitler in their theory of electromagnetic cascades, a theory explaining the existence of atmospheric showers observed by Auger.

A part of cosmic rays producing ionization similar to that of electrons was penetrating even through thick layers of absorber, which was in contradiction with the theory of bremsstrahlung. The idea of a new particle was coinciding with the Yukawa's prediction of a particle with a mass of several hundreds electrons. This particle should be unstable, which was explaining the fact that thin air in the top of the atmosphere was absorbing the particles better than the same amount of dense air. The decay is more probable on longer distances. However, some features of this particle were not corresponding to Yukawa's predictions.

The detection of low ionizing particles progressed in the 40s thanks to the development of photographic emulsions. Short living particles leave in nuclear emulsions a path visible under a microscope. So it was found that mesons π created in a nucleus decay into a bit lighter leptons μ, thus explaining why the strongly interacting negative pions are not captured back by nuclei of the opposite charge. The muons escape and decay into electrons and neutrinos instead. Thus, the particles observed in the cosmic rays were not pions but

weakly interacting muons.

Later, mesons K and heavier hadrons were also identified in nuclear emulsions. As all of these particles are unstable they belong to the secondary cosmic rays, strongly interacting component. Muons represent the penetrating component. Primary particles are mostly protons. Helium nuclei are ten times less abundant but still hundred times more than Li, B, Be. More frequent is a group of heavier nuclei from C to Fe and than the number of nuclei drops rapidly with increasing proton number. Elements with even number of protons are more abundant than those with odd one.

Electromagnetic component forms just a small part of primary cosmic rays. In the energy band bellow 1 TeV electrons amount to 0.4 %, positrons to 0.04 % and quanta gamma to 0.1 %. Occurrence of higher energy charged particles is suppressed by emission of synchrotron radiation in the interstellar magnetic field. The only unstable particles present in the primary cosmic rays are energetic neutrons. Thanks to relativistic effects their halflife is long enough to cover significant distances.

Based on this knowledge it is possible to build the model of production of secondary cosmic rays. The primary particle (usually proton) interacts in the top of the atmosphere with the atoms of air. Dependent on the energy of the particle numerous hadrons are produced, mostly pions. Some of them can again interact with nuclei and produce hadronic shower. However, unstable particles decay rapidly. The main decay modes, their percentages as well as mean lives of pions and kaons are written in the following list:

$$
\begin{array}{lll}
\pi^{\pm} \longrightarrow \mu^{\pm} + \nu_{\mu}\ (\bar{\nu}_{\mu}) & (99.99\ \%) & \tau = 2.6 \times 10^{-8}\ \mathrm{s} \\
\pi^{0} \longrightarrow \gamma + \gamma & (98.80\ \%) & \tau = 8.4 \times 10^{-17}\ \mathrm{s} \\
K^{\pm} \longrightarrow \mu^{\pm} + \nu_{\mu}\ (\bar{\nu}_{\mu}) & (63.43\ \%) & \\
\quad \longrightarrow \pi^{\pm} + \pi^{0} & (21.13\ \%) & \tau = 1.2 \times 10^{-8}\ \mathrm{s} \\
K^{0}_{s} \longrightarrow \pi^{+} + \pi^{-} & (68.95\ \%) & \\
\quad \longrightarrow \pi^{0} + \pi^{0} & (31.05\ \%) & \tau = 8.9 \times 10^{-11}\ \mathrm{s} \\
K^{0}_{l} \longrightarrow \pi^{0} + \pi^{0} + \pi^{0} & (21.05\ \%) & \\
\quad \longrightarrow \pi^{+} + \pi^{-} + \pi^{0} & (12.59\ \%) & \\
\quad \longrightarrow \pi^{\pm} + \mu^{\mp} + \nu_{\mu}\ (\bar{\nu}_{\mu}) & (27.19\ \%) & \\
\quad \longrightarrow \pi^{\pm} + e^{\mp} + \nu_{e}\ (\bar{\nu}_{e}) & (38.81\ \%) & \tau = 5.2 \times 10^{-8}\ \mathrm{s}
\end{array}
\qquad (1)
$$

Muons and neutrinos form the penetrating component. Energetic muons can easily reach the ground. The less energetic decay via

$$
\mu^{\pm} \longrightarrow e^{\pm} + \nu_{e}\ (\bar{\nu}_{e}) + \bar{\nu}_{\mu}\ (\nu_{\mu}) \qquad \tau = 2.2 \times 10^{-6}\ \mathrm{s} \qquad (2)
$$

This process adds to the electromagnetic component. Electromagnetic component dominates $5 - 15$ km above the sea level.

A part of secondary cosmic rays is formed by thermal neutrons, which give rise to an important reaction with nitrogen. They are slowed down in collisions with nuclei and subsequently absorbed by nitrogen. Created nucleus is unstable and decays via

$$^{14}N + n \longrightarrow {}^{14}C + p$$

Resulting nucleus is β-radioactive and decays into ^{14}N with the halflife of 5700 years. Radioactive carbon reacts with oxygen and forms CO_2 and sinks to lower altitudes where enters biological processes. A well known archaeological method is based on the fact that it is possible to determine the age of a sample (or the time when it stopped exchanging the carbon with the atmosphere) by the the content of undecayed ^{14}C nuclei. This is an example of practical application of cosmic ray effects.

A new era of particle physics started in 1953, when the accelerator called Cosmotron able to produce particles of 3.3 GeV energy was put into operation in Brookhaven. The cosmic rays were overshadowed by man-made radiation.

2.2 Cosmic rays of ultra high energy

The attention was turned back to the cosmic ray observations, when the first particle with the energy above 10^{20} eV was observed at the Volcano Ranch Array (in 1961) and it was realized that such an energy cannot ever be prepared in a man-made accelerator.

The Volcano Range experiment was operational in 1959 – 1963 and consisted of 19 plastic scintillators, each of 3.3 m^2 detecting surface, viewed by 5 inch photomultiplier. With 884 m spacing of the stations the array covered an area of 8 km^2. Observation of the particle with energy of about 1.4×10^{20} eV (with corrections added later) was reported by Linsley in [Lin63].

Another scintillation array, called SUGAR, was build in Australia and operated 1968 to 1979. The 54 stations spread on the area of 54 km^2 were buried 1.7 m below the surface with the aim of detecting the penetrating muons (see for example [Win86]). This was the only experiment observing the southern sky until the construction of the Pierre Auger Observatory that will be described in detail in the following chapters.

The use of an array of Čerenkov water tanks as the surface detector was pioneered by Haverah Park group, UK in 1968 to 1987 [Law91]. It was formed by several subarrays in an irregular grid, complemented in the last years by 8 scintillators used for cross-calibration with other experiments.

Another scintillator array started taking data in 1970 in Yakutsk and is still operational. It has a sophisticated layout of smaller and larger station separations to increase the dynamic range of the detector.

The last and largest scintillator array was operational in 1990 through 2004 in Akeno, Japan. The AGASA array was formed by 111 scintillators of 2.2 m^2 each, spaced about

1 km apart covering 100 square kilometres. 27 muon detectors were also added to the scintillation array.

Finally, a new technique was implemented in 1981 by the Fly's Eye experiment, observing directly the passage of the shower through the atmosphere. The first part, Fly's Eye I consisted of 67 mirror segments 1.5 m in diameter with total of 880 photomultipliers covering the whole sky (5.5° field of view each). Fly's Eye II was build 3.4 km apart looking towards the Fly's Eye I. It had 36 mirrors and 464 phototubes. The only event with energy above 10^{20} eV detected by this experiment happened to be the largest ever observed. The energy assigned to it was 3.2×10^{20} eV (51 J). The next generation of the detector - HiRes (or High Resolution Fly's Eye) started operation in 1997. It also consists of two parts separated by 12.6 km. The first part is formed by 21 mirrors and 256 phototubes per mirror in one ring covering $3° - 17°$ in elevation and almost all azimuthal angles. The second part has two rings with double the the amount of mirrors covering $3° - 31°$ in elevation. Each phototube is viewing a 1° by 1° segment of the sky.

The cosmic ray flux measured by the last two experiments came as something of a surprise. The AGASA flux seems to continue beyond the $10^{19.4}$ eV virtually unchanged, while the HiRes flux exhibits a significant cut-off (see Fig. 4).

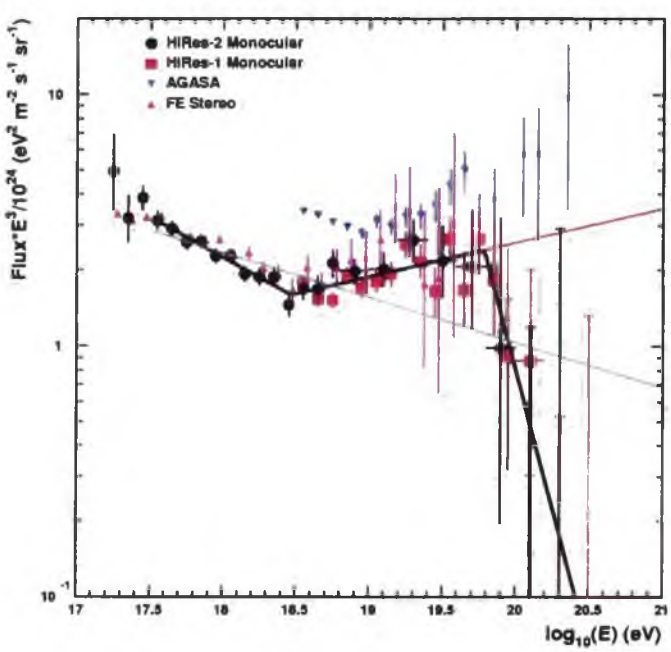

Fig. 4. *Comparison of the energy spectra measured by AGASA and HiRes given in [Abb05]. The solid lines fits of the data by single power law (turquoise), two power laws (red) and three power laws (black).*

The disagreement of the results of the two latest experiments together with large uncertainties of the high end of the energy spectrum were calling for a new generation detector with even larger collecting area and an improved detection technique.

3 Astrophysical considerations

GZK limit

Soon after the first particle with the energy above 10^{20} eV was reported by Linsley another important discovery brought about by Penzias and Wilson, the cosmic microwave background (CMB) [Pen65]. Shortly after this, Greisen [Gre66] and independently Zatsepin and Kuzmin [Zat66] predicted that UHECR particles traversing the universe should loose their energy in interactions with the CMB. For example a proton should undergo one of the processes

$$\begin{aligned} p + \gamma_{2.7K} &\longrightarrow \Delta^+ \longrightarrow n + \pi^+ \\ &\longrightarrow \Delta^+ \longrightarrow p + \pi^0 \\ &\longrightarrow \Delta^+ \longrightarrow p + e^+ + e^- \end{aligned} \quad . \tag{3}$$

The threshold energy for pion production (the first equation) is $10^{19.6}$ eV and the mean free path about 6 Mpc. The energy loss is about 20 % in each interaction [Nagoo].

Similarly, heavy nuclei of mass A would interact with CMBR via photodisintegration or pair-production

$$\begin{aligned} A + \gamma_{2.7K} &\longrightarrow (A-1) + N \\ &\longrightarrow (A-2) + 2N, \\ &\longrightarrow A + e^+ + e^- \end{aligned} \tag{4}$$

where N is neutron or proton. Therefore an UHECR particle should not reach the Earth unless it is coming from a nearby source. This limitation became known as the GZK cutoff.

3.1 Conventional sources

When looking for possible sources of UHECR a simple consideration is taken into account, that the size of the accelerating region should be comparable to the Larmor radius of the particle in the magnetic field of the accelerator. Larmor radius (in SI units) is defined as

$$R_L = \frac{m\, v_\perp}{|q|B}, \tag{5}$$

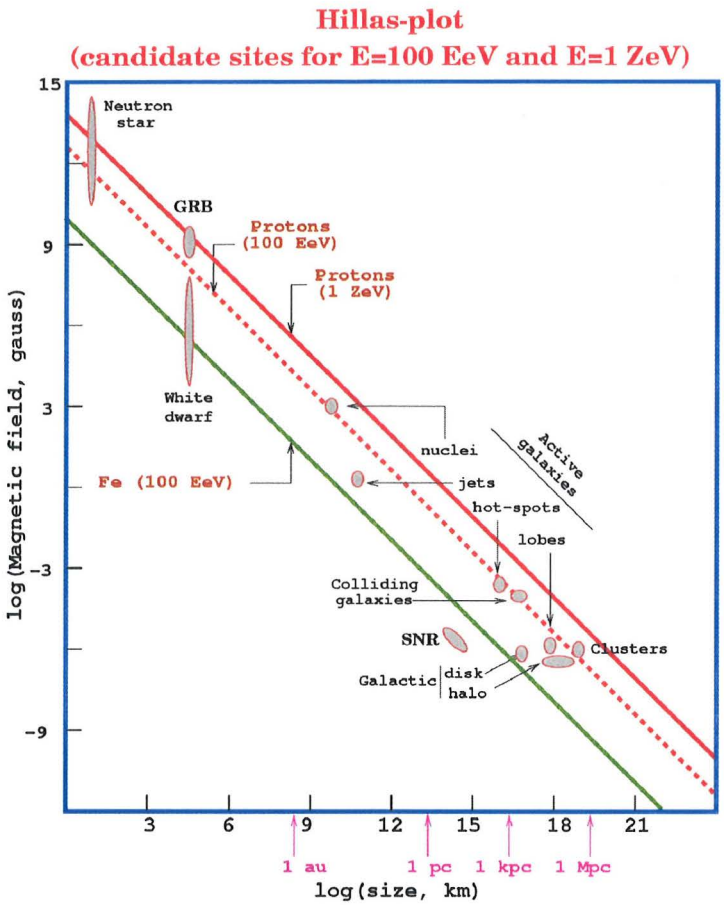

Fig. 5. *Plot of the possible conventional sources of UHECR considering their dimensions and magnetic field.*

where m and q are the mass and the charge of the particle, $v_\perp$ is the velocity component perpendicular to the direction of the magnetic field and B is the magnetic field of the accelerating region.

Using this criterion the Fig. 5 was compiled [Hil84]. Few astrophysical objects come into question. In our Galaxy, young neutron stars have a sufficient magnetic field strength ($\sim 10^{13}$ G) to accelerate the particles to UHECR energies. However, the particles would have to be heavy nuclei in order to be isotropized enough not to show any correlation with the Galactic plane.

Radio galaxy hot spots could be another possible source of the ultra high energy particles. They are interpreted as a termination shock of a jet shooting from the central active galactic nucleus. The typical size of the hot spot is several kiloparsecs with the magnetic field reaching some hundreds of μG.

BL Lac objects are active galactic nuclei with the jet pointing towards us. A correlation of the observed UHECR directions with this subset of active nuclei was reported

recently (see for example [Goro6]). The estimated maximum energy could indeed reach 10^{20} eV.

Gamma-ray bursts (GRB) are also possible sources of UHECR particles - both have an unclear origin and an isotropic distribution. However, the recent observations of gamma-ray bursts show that a large portion is located in cosmological distances and would be therefore liable to GZK limit.

3.2 Top-down scenarios

As can be seen from Fig. 5, none of the conventional sources mentioned above is convincingly capable to accelerate particles to the extreme energies in question, let alone the fact that particles are likely to loose their energy when escaping the accelerating region or during propagation through the universe.

Exotic scenarios are therefore being proposed. The first such mechanism (also called Z-bursts) would be an extremely energetic neutrino arriving from any cosmological source interacting with a background relic neutrino via Z^0 boson. The resonance energy for this process is 4×10^{21} eV. The Z boson decays producing nucleon-antinucleon pairs, which, after several subsequent decays of secondary particles, result in many photons and neutrinos.

Other possibilities include the decay of relic superheavy particles, which are supposedly part of the cold dark matter, or a new neutral hadron could be observed. Also magnetic monopoles accelerated in the Galactic magnetic field and topological defects, left over from the early stages of the universe have been suggested.

4 Extensive Air Showers

In the energy range above 10^{14} eV the flux of primary particles becomes so small that a direct observation is no longer possible. At very high energies the cosmic ray detection is confined to the ground using the atmosphere as a vast calorimeter, where extensive air showers (EAS) are produced. When a very energetic particle reaches the atmosphere, it collides with molecules of air producing secondary particles energetic enough to collide again so that a shower of secondary particles develops in consecutive interactions. The cascading process continues until the energy of the fragments becomes insufficient for further production of secondaries. The first interaction typically occurs at the height of $20 - 30$ km depending on the energy and type of the primary particle. Most abundant components of a developed EAS are photons, electrons and positrons.

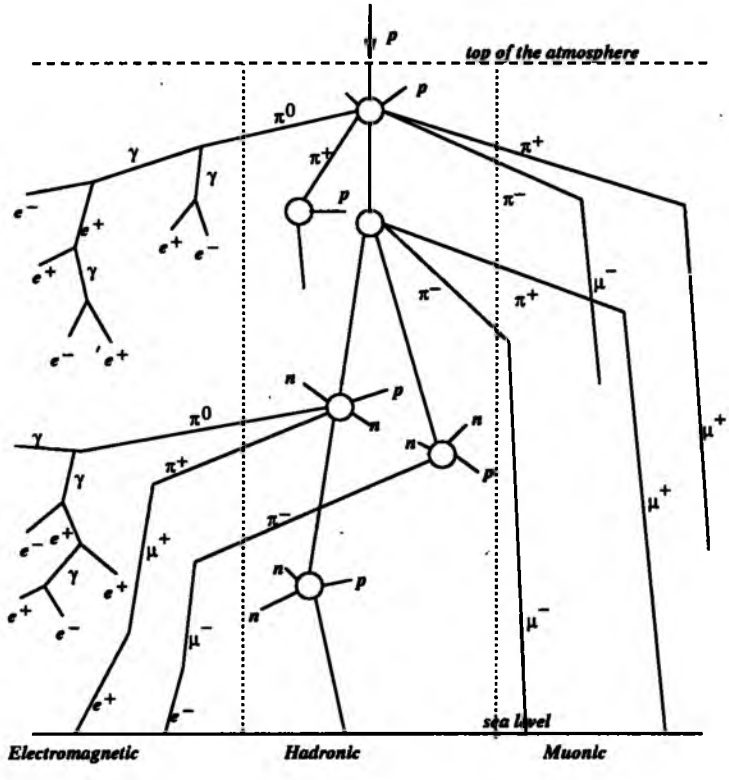

Fig. 6. *Scheme of a hadronic cascade*

4.1 Hadronic showers

Primary cosmic ray particles are mostly hadrons, therefore hadronic showers, sketched in Fig. 6, are the most frequent type of EAS. Hadronic shower reaches the ground approximately after 12 interaction steps.

The particles produced in the first interaction with a molecule of air are predominantly charged and neutral pions but also heavier mesons and hadrons appear. The charged pions decay and give rise to the muonic component of the shower via

$$\pi^{\pm} \longrightarrow \mu^{\pm} + \nu_{\mu}\,(\bar{\nu}_{\mu}) \qquad \tau = 2.6 \times 10^{-8}\,\mathrm{s}, \tag{6}$$

where τ is the mean life. A list of other particles and their decay schemes can be found in (1). Also the muons are unstable and contribute to the electromagnetic component via

$$\mu^{\pm} \longrightarrow e^{\pm} + \nu_{e}\,(\bar{\nu}_{e}) + \bar{\nu}_{\mu}\,(\nu_{\mu}) \qquad \tau = 2.2 \times 10^{-6}\,\mathrm{s}. \tag{7}$$

Owing to the relatively long mean life, muons often penetrate the whole atmosphere and form a major part of cosmic rays observed at the see level.

The electromagnetic component of a hadronic shower is generated mainly in decays of neutral pions

$$\pi^{0} \longrightarrow \gamma + \gamma \qquad \tau = 8.4 \times 10^{-17}\,\mathrm{s}. \tag{8}$$

The nucleonic core of the shower initiates further cascades until the energy falls below the threshold for multiple pion production. The core is surrounded by electromagnetic showers originating in pion decays. As the hadron component gets weaker, electromagnetic cascades are formed just around the core and tens of metres from the shower axis only muons produced in charged pion decay and their decay products - electrons and neutrinos (and eventually photons from the neutral pion decay) are to be found.

4.2 Electromagnetic cascades

The development of electromagnetic cascades (initiated by primary or secondary photon, electron or positron) is far simpler than that of hadronic ones. Their description is limited to only three types of particles: photons, electrons and positrons (the production of a muon pair is suppressed by a factor of $\left(\frac{m_e}{m_\mu}\right)^2 \approx 2 \times 10^{-5}$ and a direct photoproduction is 300 times less probable). Also, for high energies (above 100 MeV), only two processes are dominating: bremsstrahlung (for electrons and positrons) and pair production (for photons).

The basic idea of a photon induced cascade is sketched in Fig. 7. A primary gamma enters the field of a nucleus and produces an electron-positron pair. After approximately

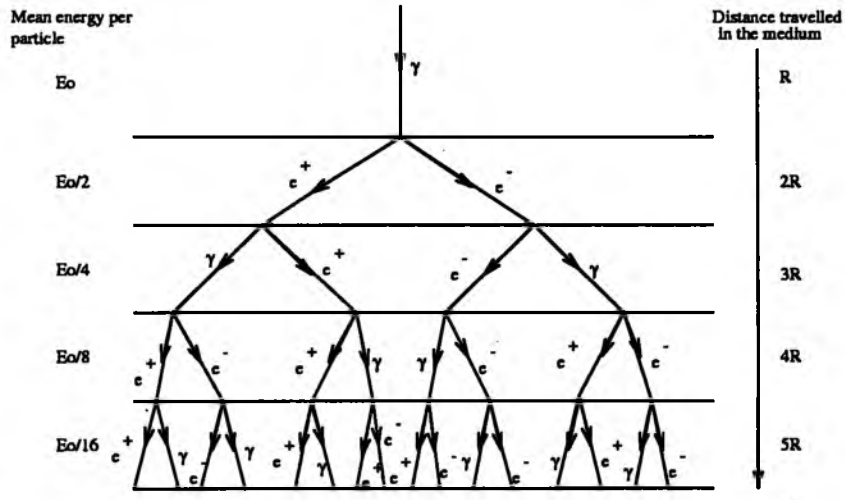

Fig. 7. *A simple model of an electromagnetic cascade*

one radiation length electrons and positrons will interact with another nucleus and emit bremsstrahlung photons, which can subsequently produce another pair. The number of particles doubles after each generation until the average energy of the particles reaches the critical value E_c that is when the ionization losses become more important than radiation losses ($E_c \sim 84$ MeV in air). From this point the number of particles absorbed is greater than number of created ones and the cascade diminishes.

It can be also seen from the Fig. 7, that development of electron or positron induced showers is much the same as for a photon, only it is shifted by one radiation length.

The cascade development can be characterized by Greisen formula [Gre56]:

$$N_e(t) = \frac{0.31}{\sqrt{y}} \exp\Big(t\,(1-\frac{3}{2}\ln s)\Big), \tag{9}$$

which gives the mean number of electrons as a function of atmosphere depth t expressed in radiation lengths ($X_0 \sim 37$ g/cm^2) and primary energy E_0. In this formula $y = \ln\left(\frac{E_0}{E_c}\right)$ and s is the age parameter of the shower defined as

$$s = \frac{3}{1+\frac{2y}{t}}. \tag{10}$$

The number of particles is maximal for $s = 1$, i.e. in the depth $t_m = y = \ln\left(\frac{E_0}{E_c}\right)$. As the particles are relativistic and momentum of each particle is shared by the two newly generated, the shower is very directional.

The energy E_{em} imparted to the electromagnetic components can be estimated as

$$E_{em} = \frac{E_c}{X_0}\int_0^\infty N_e(t) X_0 dt, \tag{11}$$

where the integral represents a total track length of electromagnetic particles.

In hadronic showers at 10^{19} eV the electromagnetic component forms $80-90\%$ of the total energy depending on the primary energy and the type of particle. A correction for unseen energy has to be determined from simulations. The final primary energy estimation according to [Hil91] is obtained as

$$E_0 = 2.65\ \mathrm{MeV} \int_0^\infty N_e(t) X_0 dt, \tag{12}$$

Lateral distribution of the shower particles on the ground is then sampled by an array of ground detectors, while the longitudinal development of the shower can be observed by fluorescence telescopes.

Derivation of the number of electromagnetic particles by the air fluorescence technique is discussed in chapter 6.

5 Pierre Auger Observatory

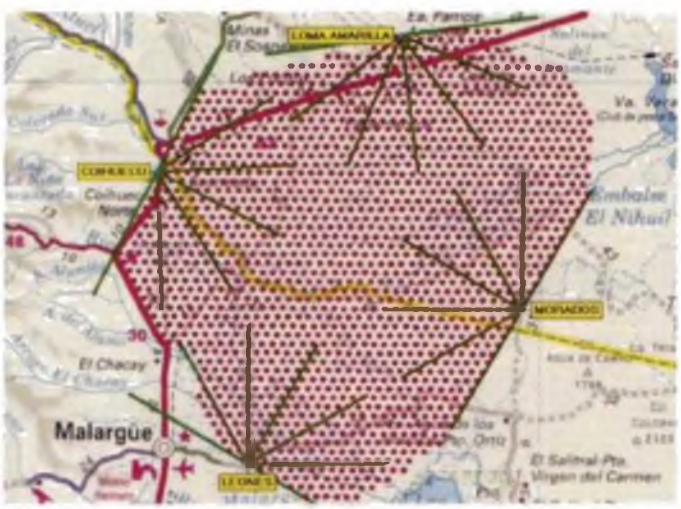

Fig. 8. *Layout of the Pierre Auger observatory: 1600 water-tanks over-looked by 4 fluorescence detectors [TDR02].*

The Auger Project is an international effort to clarify the many unsolved aspects of the highest energy cosmic rays. It was designed to combine two established detection techniques — the surface array of particle detectors and air fluorescence telescopes. Hybrid (simultaneous) operation of the two detectors allows to cross-calibrate the two methods and to better understand their systematic uncertainties. As the ultrahigh energy cosmic rays are extremely rare (about one particle with the energy above 10^{19} eV per square kilometre per year strikes the Earth) the detector has to cover an enormous area in order to provide an adequate statistical power in a reasonable amount of time. Moreover, in order to be able to cover the whole sky, two such observatories are envisaged - one in the southern and one in the northern hemisphere.

Southern site of the Pierre Auger Observatory is located near the small town of Malargüe in Mendoza province, Argentina. Hidden behind the Andes this location has good meteorological conditions. Flat terrain and an ideal altitude, close to the vertical shower maximum (1450 m above sea level) together with a low light pollution make the Argentinian pampa a suitable site for both detection techniques.

5.1 Surface array

Ground arrays sample the lateral distribution of shower particles reaching the ground. The Auger surface detector consists of 1600 plastic tanks, placed 1.5 km appart in a regular grid (see Fig. 8) covering an area of 3000 km^2. Each tank is 1.2 m deep, 3.6 m in diameter and it contains 12 000 litres of purified water sealed in a highly reflective Tyvec liner.

Čerenkov photons produced by shower particles traversing the water volume are reflected off the walls of the tank into three 9-inch Photonis XP1805 phototubes. Timing is provided by a GPS Motorola unit and data are sent to the data acquisition centre via a custom build wireless communication system. Two solar panels power the tank and charge the two 12 V batteries used during nights or cloudy days. The total power budget of a tank is less than 10 watts. Each tank is therefore independent and can start operation immediately after installation. Duty cycle of the surface array is almost 100%. A picture of a Čerenkov water tank is shown in Fig. 9.

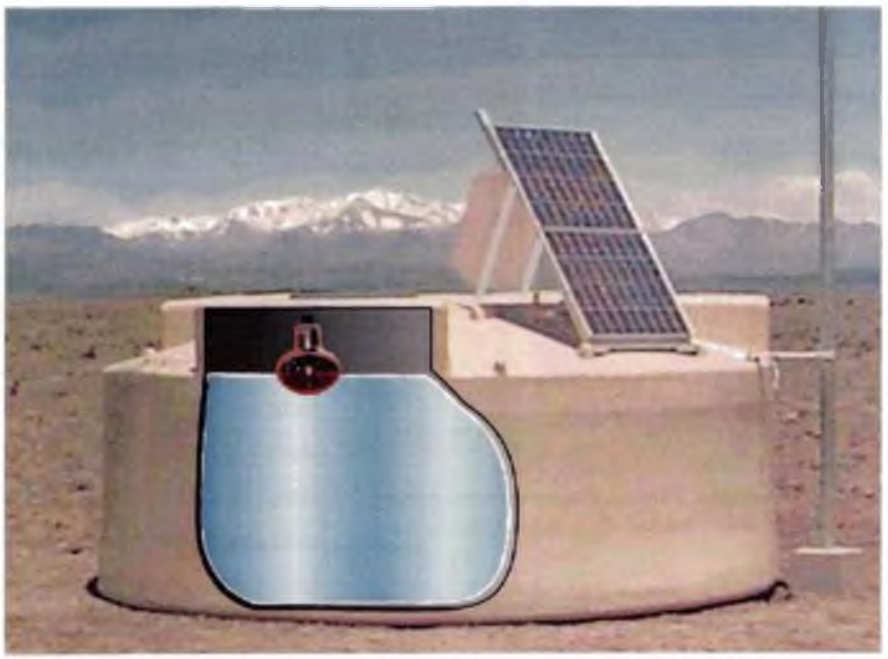

Fig. 9. *Čerenkov water tank of the Pierre Auger surface array.*

5.2 Fluorescence telescopes

The surface stations are overlooked by fluorescence detectors located in four buildings on the perimeter of the array. Each building contains 6 telescopes with 30° by 30° field of view (see Fig. 8). Each telescope consists of 3.8 by 3.8 m (with the radius of curvature of 3.4 m) segmented spherical mirror focusing the light onto a camera in the focal surface (see Fig. 10). The camera is formed by 440 hexagonal phototubes with 4.5 cm in diameter and 1.5° field of view each. Light concentrators in the form of a "Mercedes" star are covering the gaps between the phototubes to improve the light collection efficiency.

The telescopes are using modified Schmidt optics with a corrector ring (in place of a corrector plate) of inner diameter 1.7 m and an outer diameter matching the aperture, i.e. 2.2 m. This system allows to control the spherical aberration keeping the light spot

reflected on the camera within an angular size of 0.5°. To improve the signal-to-noise ratio the system is complemented by an M-UG6 filter limiting the passing light to the region, where most of the fluorescence is emitted, i.e. $300 - 400$ nm. Timing is again provided by a GPS system. Status of the electronics, atmospheric conditions and other relevant aspects are monitored and in case of an emergency the shutters in front of each aperture close automatically and the detector is shut down.

Fluorescence detector measures longitudinal development of the cosmic ray shower in the atmosphere by recording the near UV light produced in interactions of shower particles with the nitrogen molecules. As the fluorescence light is quite faint the operation is limited to clear moonless nights and the duty cycle reaches about 10 %. Energy threshold of the fluorescence technique is being quoted at 10^{17} eV, however only close showers can be seen at this energy. Full coverage of the surface detector area should be reached at $\sim 10^{19}$ eV.

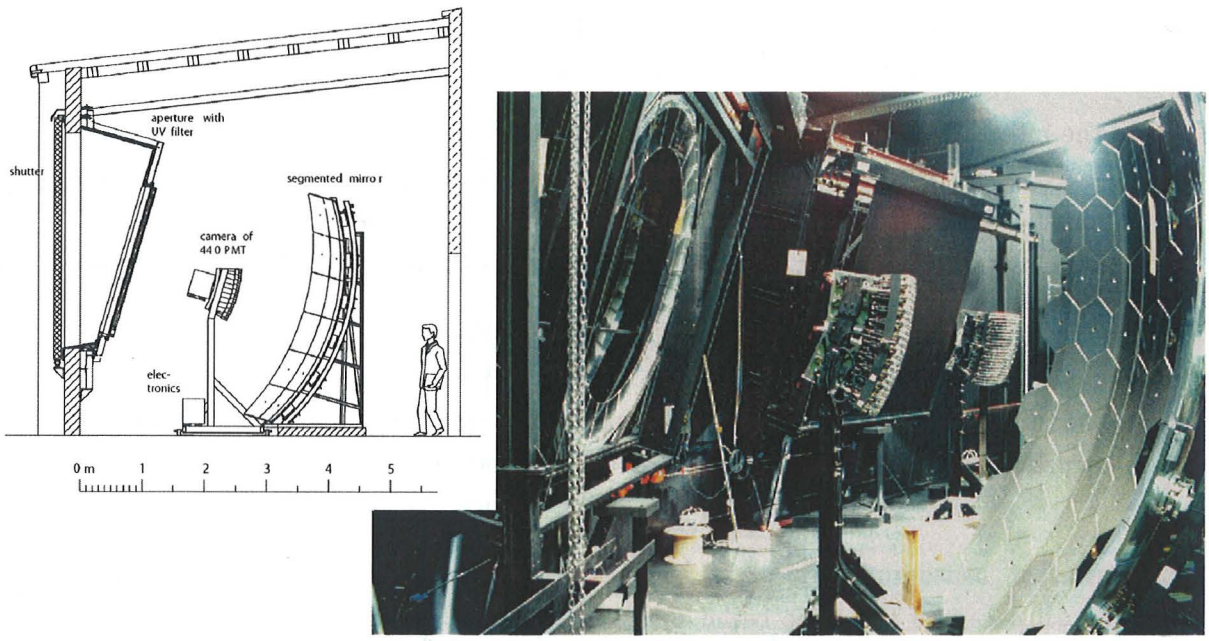

Fig. 10. *Fluorescence telescope of the Pierre Auger observatory.*

5.3 Fluorescence technique

The fluorescence detection of cosmic ray air showers exploits the fact that charged secondary particles (mostly electrons and positrons) passing through the atmosphere are exciting and ionizing the nitrogen molecules, which then, on their return to the ground state emit photons mainly in the near UV region ($300 - 400$ nm).

Simulations [Riso4] show that most of the energy released in the atmosphere should be attributed to electrons and positrons with energies bellow 1 GeV. It is commonly assumed

that the number of emitted fluorescence photons is proportional to the energy deposited in the atmosphere, from which the primary energy can be deduced. The coefficient of the proportionality is the air fluorescence yield Y_{fl} (in the units of photons/MeV).

The number of fluorescence photons registered by the fluorescence detector $\mathrm{d}N_d$ created in a layer of atmospheric depth $\mathrm{d}X$ can be generally expressed as

$$\frac{\mathrm{d}N_d}{\mathrm{d}X} = \sum_{\lambda_i} \frac{\mathrm{d}N_f(\lambda_i)}{\mathrm{d}X} P(\lambda_i, X, \Theta), \tag{13}$$

where the summation runs over fluorescence bands λ_i, $\mathrm{d}N_f(\lambda_i)$ is a number of created fluorescence photons and P is a probability that the photon will be detected, X is atmospheric depth of the point of emission and Θ comprises all other geometrical factors. The probability P includes, apart from the geometrical factors also the atmospheric transmission and the detector efficiency.

The number of emitted fluorescence photons can be written as

$$\frac{\mathrm{d}N_f(\lambda_i)}{\mathrm{d}X} = \int \mathrm{d}E_1 \frac{\mathrm{d}N_1(E_1)}{\mathrm{d}E_1} \frac{\mathrm{d}E}{\mathrm{d}X}(E_1)\, Y_{fl}(\lambda_i, T, p, E_1), \tag{14}$$

where the integration runs over the secondary particle energies E_1 with the distribution $\frac{\mathrm{d}N_1(E_1)}{\mathrm{d}E_1}$, $\frac{\mathrm{d}E}{\mathrm{d}X}(E_1)$ is energy deposit and Y_{fl} is the fluorescence yield in the units of number of photons per MeV of deposited energy.

Assuming that Y_{fl} does not depend on the energy E_1 the integral (14) can be simplified to

$$\frac{\mathrm{d}N_f(\lambda_i)}{\mathrm{d}X} = Y_{fl}(\lambda_i, T, p) \frac{\mathrm{d}E_{tot}}{\mathrm{d}X}, \tag{15}$$

where the total deposit $\frac{\mathrm{d}E_{tot}}{\mathrm{d}X}$ denotes the remaining integral. Inserting (15) into (13) leads to the expression for the number of detected fluorescence photons

$$\frac{\mathrm{d}N_d}{\mathrm{d}X} = \frac{\mathrm{d}E_{tot}}{\mathrm{d}X} \sum_{\lambda_i} Y_{fl}(\lambda_i, T, p) P(\lambda_i, X, \Theta).$$

As can be seen, it is possible to asses the energy deposited in the atmosphere by measuring the fluorescence light. However, the assumption of energy independence of the fluorescence yield has not yet been experimentally proven. Moreover, large uncertainties quoted so far for the absolute fluorescence yield propagate into the primary energy determination.

Growing number of cosmic ray experiments using the fluorescence technique in the recent years stimulated many groups around the world to work on this topic. To one of these efforts, the AIRFLY experiment, will be devoted the following chapters.

5.4 Atmosphere

The last topic that has to be mentioned before delving into the details of the fluorescence measurements is the description of the atmosphere in order to asses the ranges of pressure and temperature relevant for air shower observations.

The atmosphere can roughly be characterized as the region from sea level to about 1000 km altitude around the globe. Below 50 km the atmosphere can be assumed to be homogeneously mixed and can be treated as an ideal gas. Above 80 km the hydrostatic equilibrium gradually breaks down as diffusion and vertical transport become important. The major species in the upper atmosphere are N_2, O, O_2, H, He. Temperature-oriented nomenclature differentiates the strata of the atmosphere as follows: the troposphere, from sea level up to about 11 km, where the temperature decreases; the stratosphere, from 11 km up to about 47 km, where the temperature increases; the mesosphere, from 47 km up to about 95 km, where the temperature decreases again; the thermosphere, from 95 km to about 400 km, where the temperature increases again; and the exosphere, above about 400 km, where the temperature is constant.

h_1 [km]	h_2 [km]	dT/dh [K/km]
0	11	−6.5
11	20	0.0
20	32	1.0
32	47	2.8
47	51	0.0
51	71	−2.8
71	86	−2.0

Tab. 1. *US Standard Atmosphere parametrization.*

Widely used model is the 1976 US Standard Atmosphere published in [USA76]. It was established by 30 U.S. organizations and it is based on rocket and satellite data and the ideal gas theory. The U.S. Standard Atmosphere 1976 is a series of models that define values for atmospheric temperature, density, pressure and other properties over a wide range of altitudes from sea level up to 1000 km.

Within this model the lower part of the atmosphere, relevant for the study of air showers is described by seven layers (see Tab. 1) corresponding to the nomenclature mentioned above.

Using the sea level values of pressure ($p_0 = 1013.25$ hPa), temperature $T_0 = 288.15$ K and the hydrostatic constant $k_h = 34.163$ K/km the atmosphere can be defined. Examples of typical values of pressure, temperature and density in altitudes relevant for shower creation are given in Tab. 2.

h [km]	T [K]	p [hPa]	ρ [kg m^{-3}]
0	288.15	1013.25	1.225
1	281.65	898.74	1.112
2	275.15	794.95	1.006
4	262.15	616.4	0.819
8	236.15	356.0	0.525
16	216.65	102.9	0.165
32	228.65	86.8	0.013
64	234.25	1.1	0.0002

Tab. 2. *Typical values of the US Standard Atmosphere variables in the altitudes of air shower creation.*

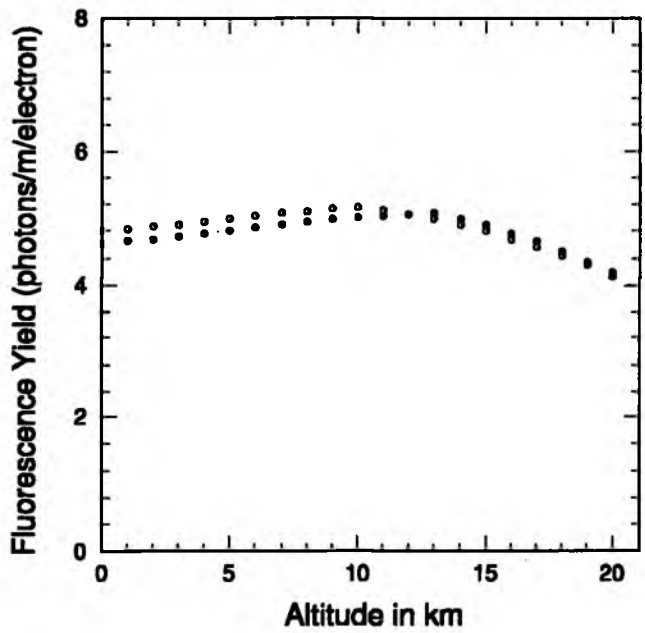

Fig. 11. *Fluorescence yield profile of an* 80 MeV *electron calculated fora typical summer (*296 K, *closed circles) and winter (*273 K, *open circles) atmosphere [Kak*96*].*

Fluorescence profile of the atmosphere calculated for an 80 MeV electron (close to the critical energy in air) using US winter and US summer atmosphere model is illustrated in Fig. 11 for the fluorescence yield data from [Kak96]. The decrease of temperature from the surface up to the tropopause causes a slight increase of the fluorescence yield. Beyond the tropopause the temperature remains almost constant but the pressure further decreases, which results in a decreasing fluorescence yield.

These differences have to be estimated accurately and taken into account in the analysis of cosmic ray showers.

6 Measurement of the fluorescence yield

6.1 Introduction

As was already illustrated in the previous chapters the fluorescence technique relies on the precise knowledge of the air fluorescence yield and its dependence on the atmospheric conditions.

This emission is called air fluorescence for historical reasons (scintillation would be more technically correct as the emission is induced by charged particles rather than photons). Nitrogen belongs to the most thoroughly studied diatomic molecules. As a major constituent of air it participates in atmospheric effects such as aurora or air fluorescence but it is also studied in gas discharges or in laser physics. N_2^+ bands can be found in the spectrum of comet tails. First studies of the molecular nitrogen spectrum date back to 1850s. In 1885 Deslandres started to publish a series of investigations on the vibrational structure of the nitrogen spectrum, where he developed a system that is now known as the Deslandres table of band heads. A thorough description of diatomic molecular spectra including data on nitrogen is given by Herzberg [Her50]. A concise compilation of the published data on molecular nitrogen spectrum was given by Lofthus & Krupenie [Lof77].

Electron excitations of nitrogen and air at high pressures were examined by Davidson & O'Neil [DaO64], Hesser [Hes67], Hirsh [Hir70], Brunet [Bru73] and many others. Laboratory measurements in the context of the detection of cosmic ray showers were performed by Bunner [Bun67]. The quoted systematic error for the fluorescence method at that time was 30 %.

More recent works by Kakimoto [Kak96], Nagano [Nag04] or Gilmore [Gil92] helped to reduce this value to about 15 %. However, this is still quoted as the largest source of systematic errors by the latest cosmic ray experiments with their improved detection techniques and large statistics.

Experiment AIRFLY is one of the recent laboratory activities striving to improve the knowledge of the fluorescence process. The scientific programme of the AIRFLY experiment includes investigations of the effects of atmospheric conditions (pressure, temperature, humidity), the primary energy dependence as well as the spectral distribution and the absolute fluorescence yield.

6.2 Theory of the fluorescence process

States of molecular nitrogen

States of molecular nitrogen can be described in terms of its electronic, vibrational and rotational structure. Transitions between two particular electronic states form a system of lines. Position of the lines within the system is given by transitions between vibrational states of the initial and final electronic state. Rotational levels create a fine structure of the lines, see Fig. 12, which may appear as a broadening of lines in devices with lower resolution.

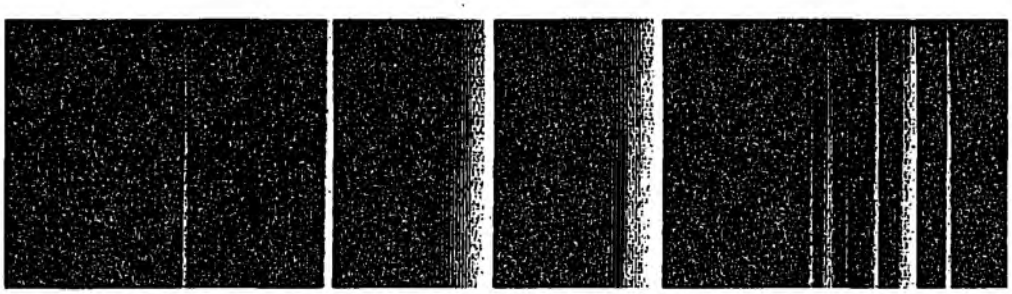

Fig. 12. *Photograph of the nitrogen spectrum showing the rotational structure of the lines [Bar62].*

Electronic states of a molecule are determined by a particular occupation of molecular orbitals formed by merging of the atomic orbitals. The atomic s states are transformed into the molecular σ orbitals. In the case of two atomic p states a σ orbital is created when the two p orbitals are parallel to the molecular axis and a π orbital is formed when they are orthogonal. The idea is depicted in Fig. 13. In each case the energy levels are split according to bonding or antibonding character of the orbital. In terms of spacial symmetry the two wave functions can combine symmetrically or antisymmetrically, which, in spectroscopic notation, is marked by g and u, respectively ($g - gerade = even, u - ungerade = odd$). Merging of the states $d, f, \ldots$ is further complicated and is not relevant in the case of nitrogen so it will not be discussed here.

There are two distinct approaches to the designation of orbitals of diatomic molecules. One is called a limit of *united atoms*, where the idea is that the atoms are spatially overlapping so that their wave functions couple symmetrically or antisymmetrically. The molecular orbitals retain these characteristics when the atoms are drawn apart to the molecular distance. This approach gives a correct ordering of energy levels in molecules with shorter bond, i.e. H_2. The other idea is that of *separated atoms*. When the atoms are drawn together from infinity, the orbitals start to deform in the direction of the molecular axis. This approach is more appropriate in the case of longer bonds, i.e. N_2. The two

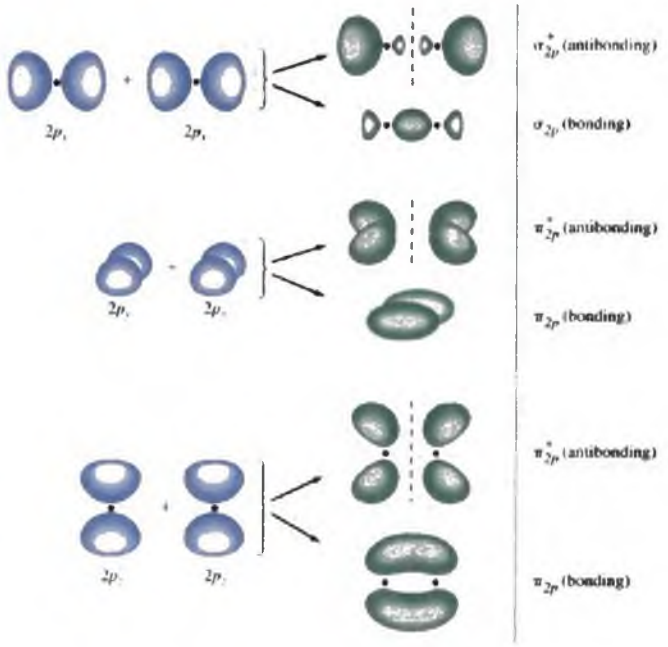

Fig. 13. *Diagram indicating the formation of molecular orbitals from atomic p orbitals.*

atomic orbitals	united atoms	separated atoms	bond/antibond
$1s_a + 1s_b$	$\sigma_g 1s$	$1\sigma_g$	σ_{1s}
$1s_a - 1s_b$	$\sigma_u 1s$	$1\sigma_u$	$\sigma^\star_{1s}$
$2s_a + 2s_b$	$\sigma_g 2s$	$2\sigma_g$	σ_{2s}
$2s_a - 2s_b$	$\sigma_u 2s$	$2\sigma_u$	$\sigma^\star_{2s}$
$2p\pi_a + 2p\pi_b$	$\pi_u 2p$	$1\pi_u$	π_{2p}
$2p\sigma_a + 2p\sigma_b$	$\sigma_g 2p$	$3\sigma_g$	σ_{2p}
$2p\pi_a - 2p\pi_b$	$\pi_g 2p$	$1\pi_g$	$\pi^\star_{2p}$
$2p\sigma_a - 2p\sigma_b$	$\sigma_u 2p$	$3\sigma_u$	$\sigma^\star_{2p}$

Tab. 3. *Notations of molecular orbitals.*

approaches are connected by correlation diagrams [Her50]. The notations are summarized in the following table Tab. 3:

In the first column, indices a and b denote the atoms, numbers 1, 2 refer to the main quantum number n and s or p correspond to the orbital quantum number $l = 0$ or $l = 1$, respectively. In the second column, the Greek letters σ or π distinguish the type of the molecular orbital created. In the third column, g and u describe the inversion symmetry and the numbers simply count the orbitals. Finally, the fourth column emphasizes bonding or antibonding character of the orbitals and relates to Fig. 13.

Electronic state of a molecule is given by a particular occupation of the orbitals

discussed above. The electronic arrangement of the molecule is well characterized by the component of the electronic orbital angular momentum along the internuclear axis Λ and the total electron spin S. Therefore, a notation of molecular states is derived from these quantum numbers. The value $\Lambda = 0, 1, 2\ldots$ is indicated by writing a term symbol Σ, Π, $\Delta, \ldots$. The total spin angular momentum is indicated by a left superscript giving the multiplicity of the state. The symbols g and u now describe the total inversion symmetry, i.e. electronic state is even and labeled with a g if the number of u electrons is even and the state is odd and labeled with a u if the number of u electrons is odd. The $+$ or $-$ superscript appears at Σ states created by two π orbitals and relates to the symmetry of the state with respect to the plane of the molecular axis. To further distinguish states with the same multiplicity letters $a, b, c, \ldots$ and $A, B, C, \ldots$ are used. X usually identifies the ground state.

Occupation of molecular orbitals in the ground state $X^1\Sigma_u^+$ and the first excited state $A^3\Sigma_u^+$ are shown in Tab. 4:

	$1\sigma_g$	$1\sigma_u$	$2\sigma_g$	$2\sigma_u$	$1\pi_u$	$3\sigma_g$	$1\pi_g$	$3\sigma_u$
$B^2\Sigma_u^+$	2	2	2	1	4	2	0	0
$X^2\Sigma_g^+$	2	2	2	2	4	1	0	0
$C^3\Pi_u$	2	2	2	1	4	2	1	0
$B^3\Pi_g$	2	2	2	2	4	1	1	0
$A^3\Sigma_u^+$	2	2	2	2	3	2	1	0
$X^1\Sigma_g^+$	2	2	2	2	4	2	0	0

Tab. 4. *Occupation of relevant orbitals in nitrogen molecules an ions.*

The nitrogen spectrum is formed by numerous systems spanning from far ultraviolet to infrared wavelengths. The Fig. 14 shows energy levels of the most dominant transition systems. At normal pressure the nitrogen emission takes place predominantly in the range between 300 and 400 nm and consists almost entirely of only two systems - the so-called second positive system (denoted as 2P) of N_2 molecule and the first negative system (1N) of the ion N_2^+. In the second positive system transitions between the electronic states $C^3\Pi_u$ and $B^3\Pi_g$ are involved, the first negative system is formed by transitions between the states $B^2\Sigma_u^+$ and $X^2\Sigma_g^+$. However, in both cases, the electron transits between the orbitals $2\sigma_u$ and $3\sigma_g$.

Within the system, position of each line is determined by vibrational levels of initial and final state. Spectrum of 2P system together with a scheme of transitions is shown in Fig. 15. Fine structure of the lines is caused by transitions between various rotational levels of each vibrational state.

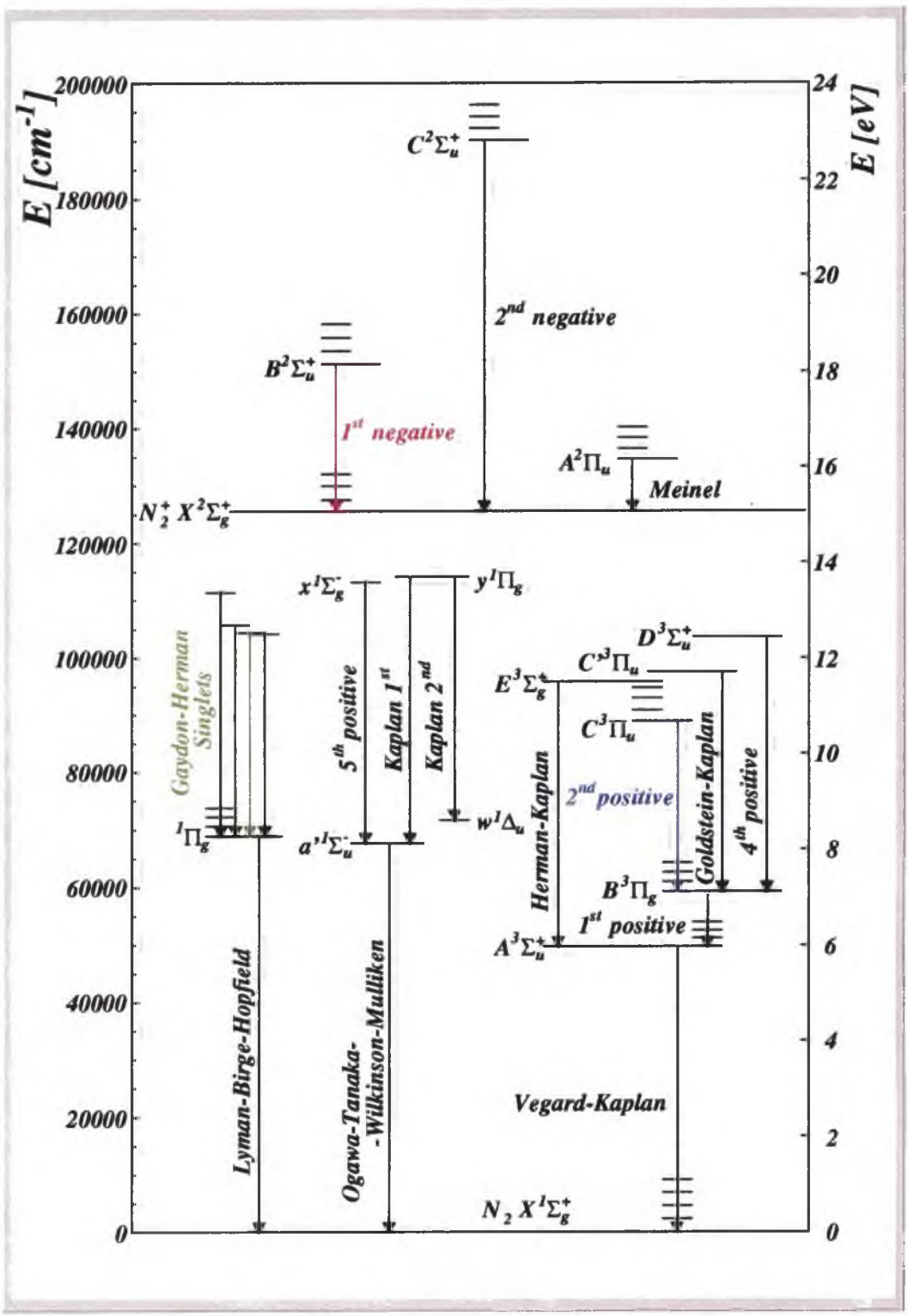

Fig. 14. *Energy levels of the nitrogen molecule.*

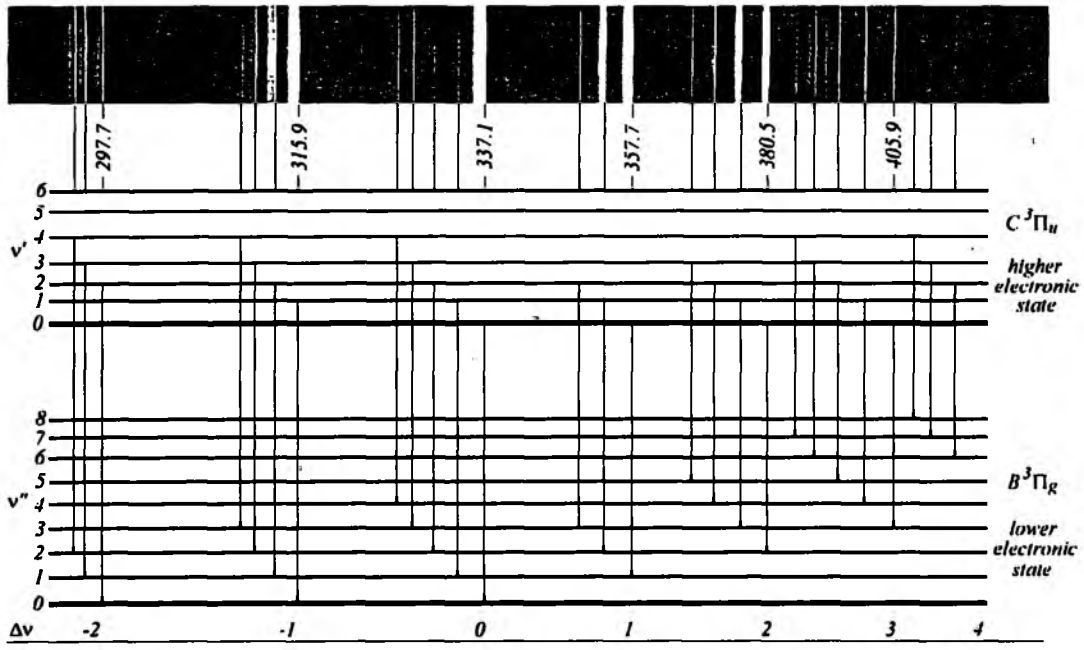

Fig. 15. *Scheme of the formation of the Nitrogen spectrum [Bar62].*

Transition probabilities and Franck-Condon principle

Transitions between particular vibrational levels within a band system can be described by the Franck-Condon principle. It states that the transition between two electronic states occurs so fast that the internuclear distance remains the same. Thorough discussion of the principle can be found in reference [Her50]. The probability of the transition (or the Einstein coefficient) is proportional to the square of the corresponding matrix element of the electric moment (transition moment).

$$R = \int \psi'^* \mathcal{M} \psi'' d\tau, \tag{16}$$

where $\mathcal{M}$ is an operator of electric moment. The wavefunction ψ can be decoupled into electronic and vibrational functions $\psi = \psi_e \psi_v$. Equation (16) can be factorized into

$$R = \int \psi'_v \psi''_v dr \int \mathcal{M}_e \psi'^*_e \psi''_e d\tau_e. \tag{17}$$

The second integral represents the electronic transition moment, which depends negligibly on the internuclear distance. The first integral is called the Franck-Condon factor and determines the intensity of the line.

The principle is demonstrated in the Fig. 16. The curves A, B represent the system energy as a function of the internuclear distance R of two electronic states. Each energy level ($\nu = 0, 1, 2, \ldots$) corresponds to eigenvalues and eigenfunctions ψ_v. In analogy to

the harmonic oscillator ψ_v is localized in the center of the potential well for $\nu = 0$ while for higher ν values it moves towards the edges of the well. Obeying the Franck-Condon principle corresponds to vertical transitions in Fig. 16. Transition probability is high when the integral $\int \psi'_v \psi''_v dr$ is large i.e. when the function maxima in the figure lay above each other.

There are no strict selection rules for vibrational transitions just some of the transitions are more probable than the others.

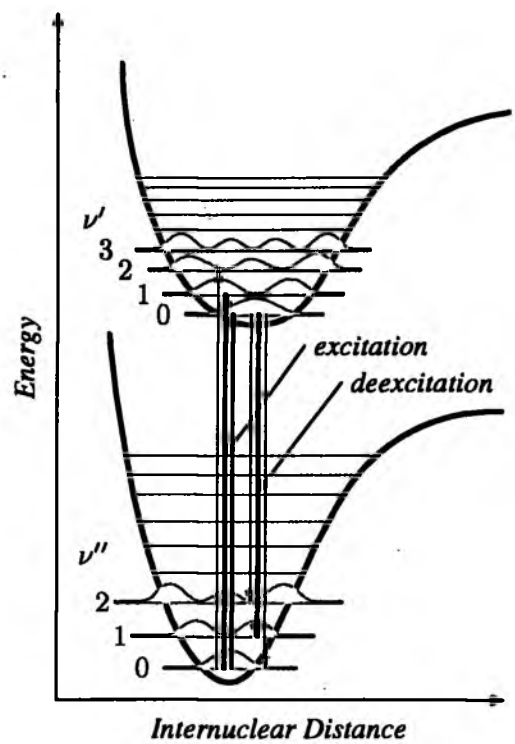

Fig. 16. *Frank-Condon principle.*

Selection rules

Electronic transitions are allowed if their dipole matrix element is nonzero

$$\int \mathcal{M}_e \psi_e'^* \psi_e'' d\tau \neq 0.$$

The following general rules can be deduced [Her50]:

1. for the quantum number J of the total angular momentum it holds that

$$\Delta J = 0, \pm 1$$

with the restriction that $J = 0 \rightarrow J = 0$ is not allowed.

2. Even electronic states combine only with odd ones, i.e. $g \leftrightarrow u$.
3. For the quantum number Λ there is a selection rule

$$\Delta\Lambda = 0, \pm 1$$

   Further, in transitions between Σ states (i.e. $\Lambda' = \Lambda'' = 0$) the symmetry with respect to the plane reflection is preserved, i.e. $\Sigma^+ \not\leftrightarrow \Sigma^-$.
4. If the spin-orbital coupling can be neglected, the spin S does not change, i.e. $\Delta S = 0$.

Transitions breaking these rules occur due to other effects (e.g. spin-orbital coupling) however generally they will be strongly suppressed.

There are no strict selection rules regarding the vibrational and rotational states — their constraint is given by the Franck-Condon principle given above or by the Hönl-London principle in case of rotational states [Her50].

Excitation of nitrogen

Ways of creation of the upper states of the systems 2P and 1N differ. The upper level of the N_2^+ 1N system can be reached directly via ionization by a high energy particle, e.g.

$$N_2 + e^- \rightarrow N_2^{+\star} + e^- + e^- \ .$$

Direct excitation of the N_2 2P system upper level from the ground state is suppressed as it does not allow a spin change. However, these levels can be excited by collisions with low energy electrons involving spin change

$$N_2 + e(\uparrow) \rightarrow N_2^{\star}(C^3\Pi_u) + e(\downarrow)$$

or via cascading from higher levels, for example following recombination, i.e.

$$N_2^+ + e \rightarrow N_2^{\star}(C^3\Pi_u).$$

Under normal conditions most of the nitrogen molecules are in their ground electronic state and zeroth vibrational level.

Fluorescence emission

De-excitation can proceed in radiative — fluorescence, or nonradiative way — internal or collisional quenching. It is convenient to define the *fluorescence yield* Y_{fl} as the number of fluorescence photons n_{fl} generated per unit of energy deposit E_{dep}, i.e.

$$Y_{fl} = \frac{n_{fl}}{E_{dep}} = \frac{n_{ex}\,\varepsilon_{fl}}{E_{dep}}, \tag{18}$$

where n_{ex} is the number of excited nitrogen molecules and ε_{fl} is the *fluorescence efficiency* defined as the ratio of the rate of de-excitation via fluorescence to the total de-excitation rate. In terms of the lifetimes of the excited states for radiation τ_ν, collisional quenching τ_c and internal quenching τ_i the fluorescence efficiency can be expressed as

$$\varepsilon_{fl} = \frac{\frac{1}{\tau_\nu}}{\frac{1}{\tau_\nu} + \frac{1}{\tau_c} + \frac{1}{\tau_i}}. \tag{19}$$

The only pressure and temperature dependent process is the collisional quenching. Rate of collisional de-excitation can be written as

$$\frac{1}{\tau_c} = \sum_X \sigma_{NX}\, n_X\, \overline{u}_{NX} \tag{20}$$

where the summation runs over all the colliding constituents of air $X = \mathrm{N_2}, \mathrm{O_2}, \mathrm{Ar}, \ldots$, σ_{NX} are cross-sections of their collisions, n_X are concentrations of these constituents and

$$\overline{u}_{NX} = \sqrt{\frac{8kT}{\pi}\frac{M_X + M_{N_2}}{M_X\, M_{N_2}}} \tag{21}$$

is the mean relative velocity of the nitrogen molecule and a constituent X; M_X and M_{N_2} are masses of the molecules. From the state equation of the ideal gas the concentration is expressed as

$$n_X = \frac{p}{kT} f_X, \tag{22}$$

where f_X is relative concentration of component X. Inserting (22) and (21) into the expression (20) it is possible to rewrite the fluorescence efficiency (19) in the form

$$\varepsilon_{fl} = \frac{\frac{\tau_i}{\tau_i + \tau_\nu}}{1 + \frac{p \sum_X \sigma_{NX}\, f_X \sqrt{\frac{8}{\pi kT}\frac{M_X + M_N}{M_X\, M_N}}}{\frac{1}{\tau_i} + \frac{1}{\tau_\nu}}}. \tag{23}$$

It is convenient to separate the pressure and temperature dependence introducing the characteristic pressure $p'(T)$ as

$$p'(T) = \sqrt{T}\,\frac{\frac{1}{\tau_i} + \frac{1}{\tau_\nu}}{\sum_X \sigma_{NX} f_X \sqrt{\frac{8}{\pi k}\frac{M_X + M_N}{M_X\, M_N}}}, \tag{24}$$

so that the final expression describing the pressure dependence of the fluorescence efficiency reads

$$\varepsilon_{fl} = \frac{\frac{\tau_i}{\tau_i + \tau_\nu}}{1 + \frac{p}{p'(T)}}. \tag{25}$$

The temperature dependence can be studied in two special cases. When the number of particles is kept constant, the pressure is proportional to the temperature and (25) leads to

$$\varepsilon_{fl} \approx \frac{1}{1 + C_1\sqrt{T}}, \tag{26}$$

i.e. the efficiency increases with decreasing temperature. In the second case the pressure is kept constant so that (25) leads to

$$\varepsilon_{fl} \approx \frac{1}{1 + \frac{C_2}{\sqrt{T}}}, \tag{27}$$

i.e. the efficiency decreases with decreasing temperature.

Dependence on energy of the primary particle

To describe the energy dependence of the fluorescence it is only necessary to consider the number of excitations. De-excitation is not affected by the primary energy. The primary particle can either excite or ionize creating secondary electrons, which can themselves excite and ionize so that a cascade of secondary particles is developed. The total excitation cross-section is then given by the sum of contributions of all the particles. Major contribution comes from low energy secondaries. The number of created secondary electrons is proportional to the energy deposit described by the Bethe-Bloch formula [PDG04].

Nota bene, in all practical cases energy deposit is not the same as energy loss. Depending on the detector geometry and primary particle energy some of the δ-electrons may be energetic enough to escape the observed volume. Assuming that all particles with energy greater than T_{cut} will escape the detector, the corresponding energy deposit can be obtained by

$$\left.\frac{-\mathrm{d}E}{\mathrm{d}x}\right|_{T<T_{cut}} = Kz^2\frac{Z}{A}\frac{1}{\beta^2}\left[\frac{1}{2}\ln\frac{2m_ec^2\beta^2\gamma^2T_{cut}}{I^2} - \frac{\beta^2}{2}\left(1+\frac{T_{cut}}{T_{max}}\right) - \frac{\delta}{2}\right], \tag{28}$$

where the quantities are

r_e	classical electron radius
m_ec^2	electron mass-energy
K	$2\pi r_e^2 m_e c^2$
A	atomic number of the material
γ	E/mc^2
β^2	$1 - 1/\gamma^2$
I	mean excitation energy of the material
T_{max}	maximum energy transferable to an electron
δ	density effect parameter
z	incident particle charge number
Z	material charge number

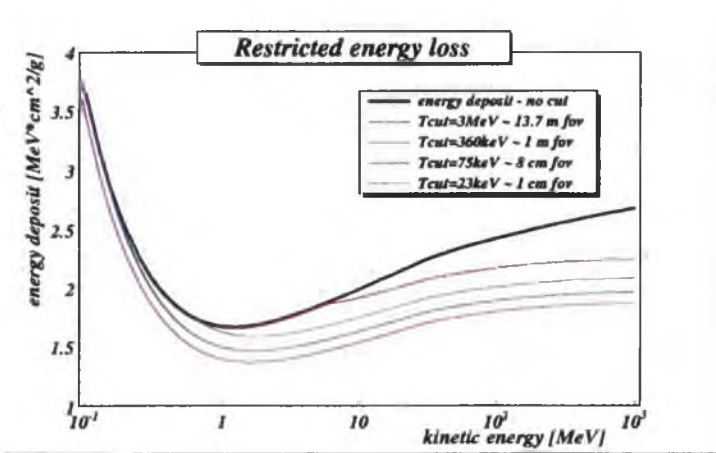

Fig. 17. *Maximum energy that will be deposited inside the detector. Particles with higher energy will escape the observed region.*

This equation is referred to as the restricted energy loss [PDG04]. Fig. 17 plots the formula for T_{cut} corresponding to several detector sizes. This form approaches the normal Bethe-Bloch function when $T_{cut} \rightarrow T_{max}$.

6.3 Theory of the Čerenkov effect

Another (and far stronger) blue-light producing effect may take place, when charged relativistic particles pass through a transparent medium — Čerenkov radiation. It appears when the phase velocity of the particles exceeds the speed of light in this medium.

Bluish light coming from transparent substances near radioactive sources was observed by many scientists already at the beginning of the century. Being very faint it was easily mistaken for other effects such as fluorescence and phosphorescence. It was not until the late twenties that this phenomenon was deliberately studied by Mallet [Mal29] and later still was it plausibly explained by Čerenkov [Cer34], Frank and Tamm [Fra37]. A thorough description of the Čerenkov effect in the context of the atmospheric showers is given in reference [Jel58].

Let us discuss the principle qualitatively. An electron moving relatively slowly through a transparent medium will polarize the medium along its trajectory. The polarized atoms will be distorted into a little dipoles (see the Fig. 18). When the electron moves into another point the atoms will relax to their normal shape. Owing to the complete symmetry the field around the particle cancels and there will be no resultant field at large distances from this region.

If the speed of the electron is comparable to the speed of light the field stays symmetrical in the plane perpendicular to the direction of flight but is no longer symmetrical along the axis so that each element of the track is radiating. However, generally the elementary

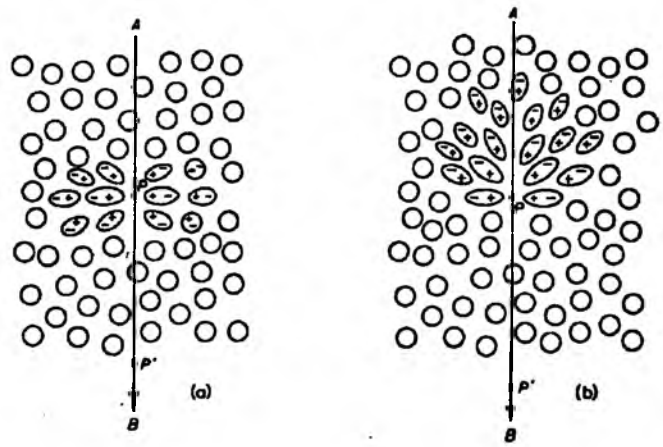

Fig. 18. *Polarization of a dielectric by a charged particle passing at a) nonrelativistic b) relativistic velocity. [Jel58]*

waves interfere destructively and there will still be no field at a distant point. Only when the velocity of the particle is higher than the phase velocity of the light in the medium will all the small waves be in phase to produce a resultant field in a distant point. Waves from different points of the track combine to form a plane wavefront. The radiation can only be observed in a narrow cone along the track. As can be deduced from the Fig. 19, for the apex angle θ of this cone it holds

$$\cos\theta = \frac{1}{\beta n}, \qquad \beta = \frac{v}{c}; \tag{29}$$

n is the refractive index of the medium, v is the velocity of the particle and c is the speed of light in vacuum.

There is a threshold velocity $\beta_{min} = 1/n$ for the production of Čerenkov radiation, for which the photons are emitted at the same direction as the flying particle. The radiation can be observed only in the regions of the spectrum where $n > 1$, that means mainly in the visible region, while in the X-ray region the radiation is impossible (mostly $n < 1$).

According to the calculations of Frank and Tamm [Fra37] the intensity of the light (energy $\mathrm{d}E$ emitted into the frequency interval $\mathrm{d}\omega$ per an element of the path $\mathrm{d}l$) can be expressed as

$$\frac{\mathrm{d}E}{\mathrm{d}l\mathrm{d}\omega} = \frac{z^2e^2}{4\pi\varepsilon_0 c}\,\omega\sin^2\theta = \frac{z^2\alpha\hbar}{c}\,\omega\left(1-\frac{1}{\beta^2n^2}\right) \tag{30}$$

where ze is the charge of the particle and α is the fine structure constant.

A quantity of interest is the number of photons emitted in a certain waveband defined by λ_{min} and λ_{max} :

$$\frac{\mathrm{d}N}{\mathrm{d}l} = \int_{\omega_{min}}^{\omega_{max}} \frac{\mathrm{d}E}{\hbar\omega\mathrm{d}l\mathrm{d}\omega}\mathrm{d}\omega = 2\pi z^2\alpha\left(\frac{1}{\lambda_{min}}-\frac{1}{\lambda_{max}}\right)\left(1-\frac{1}{\beta^2n^2}\right) \tag{31}$$

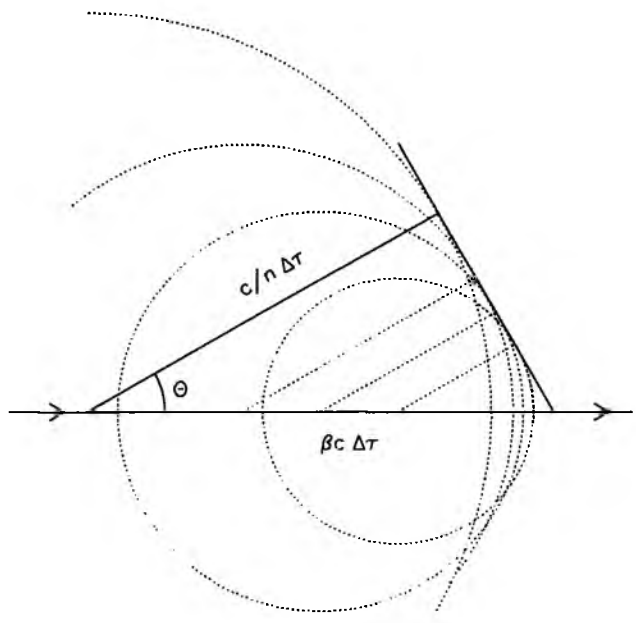

Fig. 19. *Huygens construction illustrating coherence*

For relativistic particle is

$$\beta \approx 1 - \frac{1}{2}\left(\frac{m_0 c^2}{E}\right)^2. \tag{32}$$

For materials with a small refractive index such as air, where $n = 1 + \eta$ and η is small the term can be simplified to

$$1 - \frac{1}{\beta^2 n^2} = 2\eta - \left(\frac{m_0 c^2}{E}\right)^2. \tag{33}$$

Finally, substituting this term into (31) the resulting expression reads

$$\frac{\mathrm{d}N}{\mathrm{d}l} = 2\pi z^2 \alpha \left(\frac{1}{\lambda_{min}} - \frac{1}{\lambda_{max}}\right)\left(2\eta - \left(\frac{m_0 c^2}{E}\right)^2\right), \tag{34}$$

where η is proportional to the density $\eta = \eta_0 \frac{\rho}{\rho_0}$ and the values $\eta_0 = 2.85 \times 10^{-4}$ and $\rho_0 = 1.2\ \mathrm{mg/cm^3}$ were taken at temperature 15 °C and pressure 1000 hPa for the wavelength 350 nm [ESO02]. In the wavelength interval transmitted by filters commonly used on fluorescence detectors, i.e. 300 – 400 nm, there will be 20 Čerenkov photons emitted per metre of path of an electron with critical energy in air, i.e. $E_c = 80\ \mathrm{MeV}$.

For the threshold of the Čerenkov light production it holds that $\beta\, n = 1$ and $\theta = 0$.

The threshold kinetic energy derived from (33) will then be given by

$$E_t = \frac{m_0\ c^2}{\sqrt{2\eta}}, \tag{35}$$

which for electrons in air at atmospheric pressure equals to 21 MeV.

The maximum of the Čerenkov angle (when β approaches 1) is of the order $\theta \approx \sqrt{2\eta}$, which gives 1.3° for air at atmospheric pressure.

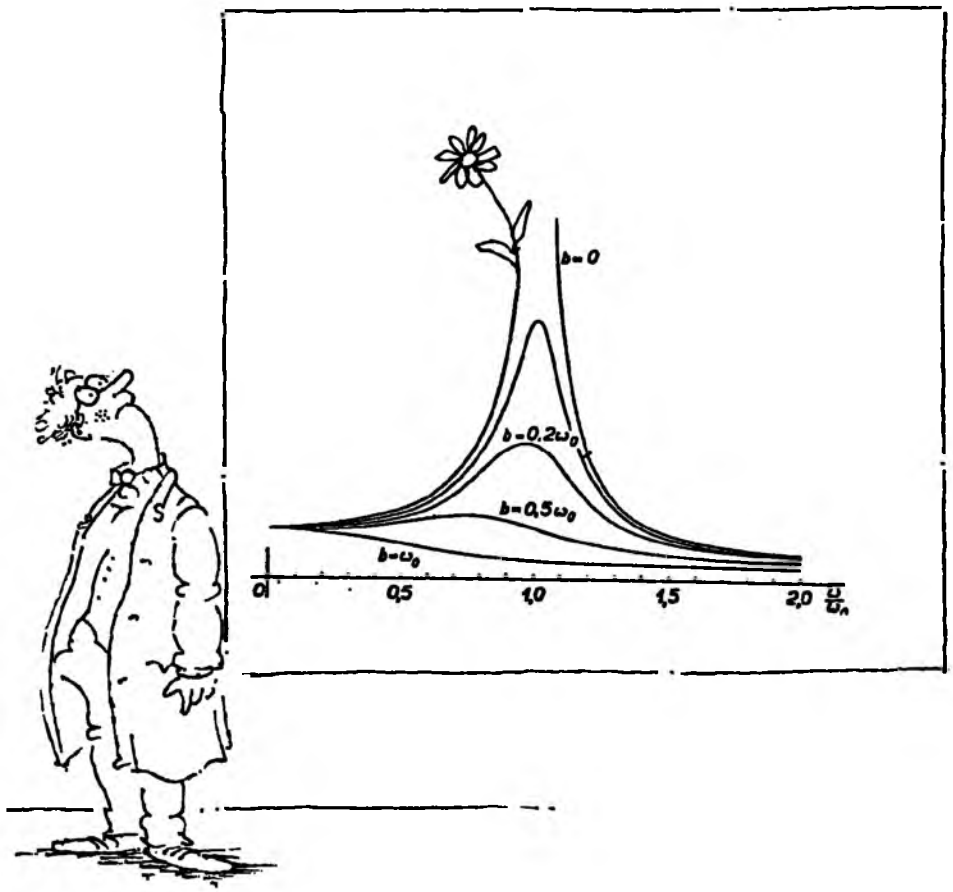
b=0
b=0.2ω0
b=0,5ω0
b=ω0
0
0,5
1,0
1,5
2,0
ω/ωn

7 Experiment AIRFLY

The scientific programme of the AIRFLY experiment consists of the measurement of the dependence of the air fluorescence yield on the thermodynamic variables (pressure, temperature, humidity, etc.), dependence on the energy of the incident particles in a wide energy range and also the measurement of the nitrogen spectrum. A new method is introduced to determine the absolute fluorescence yield of the most prominent line to better than 10 % precision. This number is used to normalize the intensity of all the lines in the nitrogen spectrum.

The AIRFLY experiment has been taking data in 2003–2005 at the BTF (Beam Test Facility), which belongs to the DAΦNE accelerator complex of the Laboratori Nacionali di Frascati, Italy, where the relative measurements were performed together with the absolute measurement of the 337 nm line.

The measurement of the spectrum was done in 2005 in the Argonne National Laboratory (ANL), USA using the Van de Graaff accelerator of the Chemical Division.

7.1 Experimental apparatus

The BTF in Frascati is optimized to provide a defined number of particles in a wide range of multiplicities and energies. It is capable to deliver electrons of energy 50 to 800 MeV and positrons 50 to 550 MeV with the intensity from single particle up to 10^{10} particles per bunch at the repetition rate up to 50 Hz. The typical pulse duration is 10 ns (1 ns can be selected). Variable depth target and a system of vertical and horizontal slits allows to select the desired energy and beam intensity.

The experimental setup used for the pressure, energy and absolute measurements is sketched in Fig. 20. To minimize the beam spread, the experimental chamber was connected directly to the beam pipe by a flange with 0.5 mm beryllium window. The chamber was followed by a fiber profilometer monitoring the beam position and a plastic scintillator or calorimeter to monitor the beam intensity.

The chamber of AIRFLY is of cylindrical shape, 400 mm long and 200 mm in diameter, made of 3 mm thick aluminium (see Fig. 21.a). Four viewports for placing light detectors are located perpendicular to the beam direction. Two 50 mm diameter Hamamatsu H7195P PMTs were used together with a DEP PP0475B Hybrid Photo Diode (HPD) capable of single photoelectron counting. Each detector was equipped by a 50 mm diameter

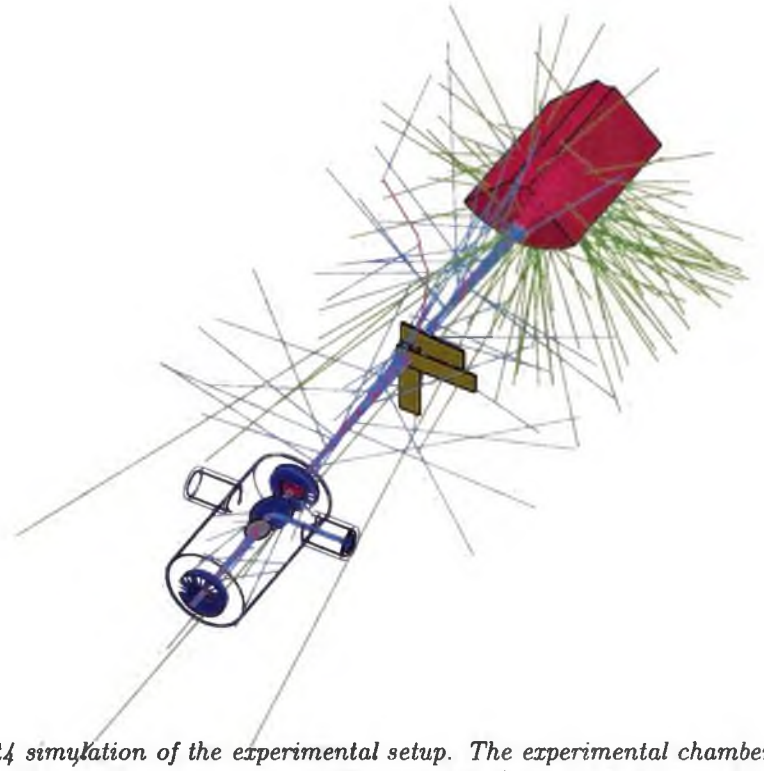

Fig. 20. *Geant4 simulation of the experimental setup. The experimental chamber is followed by the x-y fiber profilometer and a scintillator palette(close behind the profilometer). Semicylindrical NaI(Tl) calorimeter forms the last component of the beam line.*

narrow-band interference filter corresponding to the most prominent nitrogen emission line (see section 10.1 for the transmittance curve) and a remotely controlled iris shutter for background measurements. The photocathode was placed at 202 mm from the beam and the optical path was baffled to avoid any reflections off the housing walls. As the transmittance of the 337 nm interference filter depends strongly on the angle of incidence, the aperture was limited to 40mm at 60mm perpendicular distance from the beam to allow only up to 20° angle of incidence. For calibration purposes a thin mylar aluminium coated mirror could be remotely inserted at 45° into the beam thus redirecting the Čerenkov light into the photodetector. A thin black screen was permanently placed 60 mm in front of the mirror to define the Čerenkov light path length. The details of the optical system can be seen in Fig. 29. The detectors were surrounded by lead shielding in order to minimize the background.

The beam position was monitored by two scintillating fiber modules mounted at 90° and placed 500 mm behind the chamber. Each module consists of 16 bundles of fibers (12 fibers of 1 mm diameter in a bundle) optically glued together and wrapped in a thin aluminium foil. Each bundle is connected to one of the 16 pixels of a multianode PMT. The readout pitch is 3 mm.

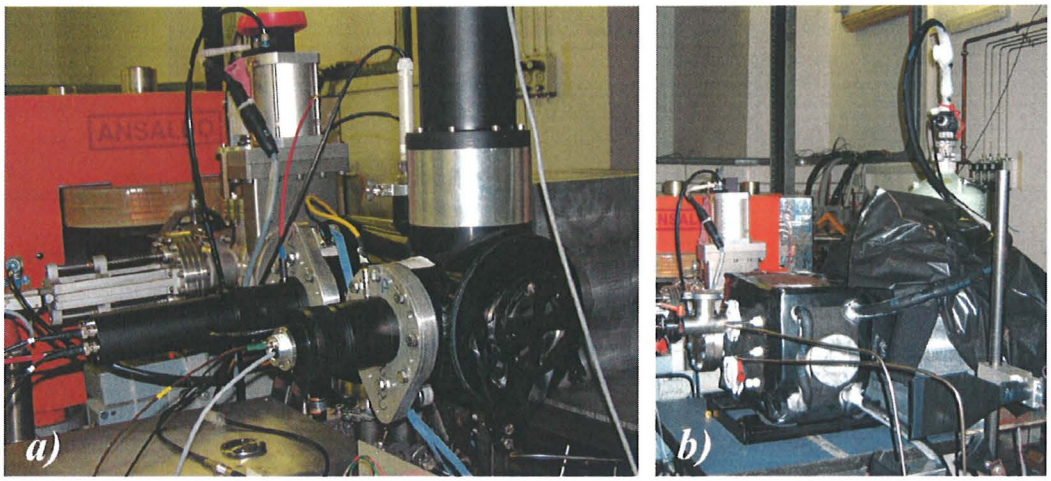

Fig. 21. *Chambers used for the fluorescence measurements a) thin-wall chamber used for the energy and pressure studies and for the absolute FLY, b) thick-wall chamber for the temperature measurement.*

The beam intensity (up to $\sim$ 1000 particles/bunch) was monitored by NaI(Tl) semi-cylindrical calorimeter with excellent single electron resolution. The calorimeter was placed at the end of the beam line 500 mm behind the profilometer and it was used mainly for testing purposes. For higher beam intensity monitoring a fast plastic scintillator (100 mm by 100 mm, 5 mm thick) was used.

Remotely controlled gas system allowed to evacuate the chamber and refill again during the measurement.

The data acquisition system was based on VME standard. The signal from PMTs and from the scintillating palette was processed by dual range 16 channel charge-to-digital converter QDC (CAEN V965). The HPD signal was send to ORTEC 450 research amplifier and then to 8 channel peak sensing ADC module (CAEN V556). Also the calorimeter signal was digitized by the peak sensing module. The 16 + 16 analog signals from the profilometer multianode PMTs were send to a 32 channel charge integrating ADC (V792). The 100 ns triggering gate signal was provided by the LINAC timing circuit for each beam pulse. The detailed scheme of the data acquisition system is given in Fig. 24. The VME controller was a VMIC 7740 Pentium III CPU with Tundra VME-PCI bridge chip, running Red Hat Linux 7.2. The DAQ programs were developed using the LabVIEW 6.0 environment [Maz03].

7.2 Temperature measurement chamber

A dedicated chamber with 30 mm aluminium walls was constructed for the temperature dependence measurement Fig. 21.b. It was equipped by several flanges for insertion of pressure, temperature and humidity probes and covered by insulation. A simple liq-

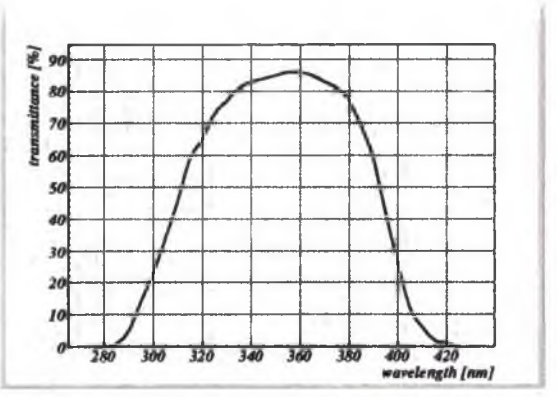

Fig. 22. *UG6 filter transmittance curve.*

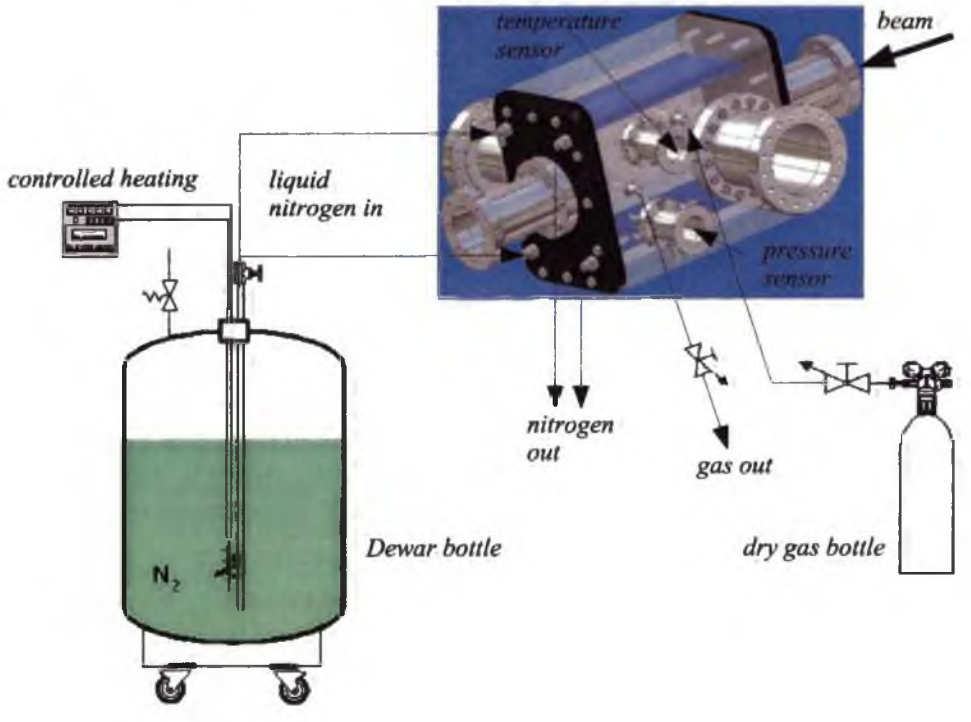

Fig. 23. *Scheme of the temperature measurement setup.*

uid nitrogen cooling system was chosen allowing to cool the chamber to −35 °C. The liquid nitrogen (boiling temperature −196 °C) was forced through heat exchangers, made of 8 mm copper tubes, at the top and at the bottom of the chamber. The viewport for fluorescence observation was covered by a quartz window and the photodetector together with a motorized filter holder was placed in front of the window with a minimum contact to minimize the heat convection. To avoid condensation on the photodetector or on the quartz window the system was constantly flushed by dry nitrogen. The whole setup

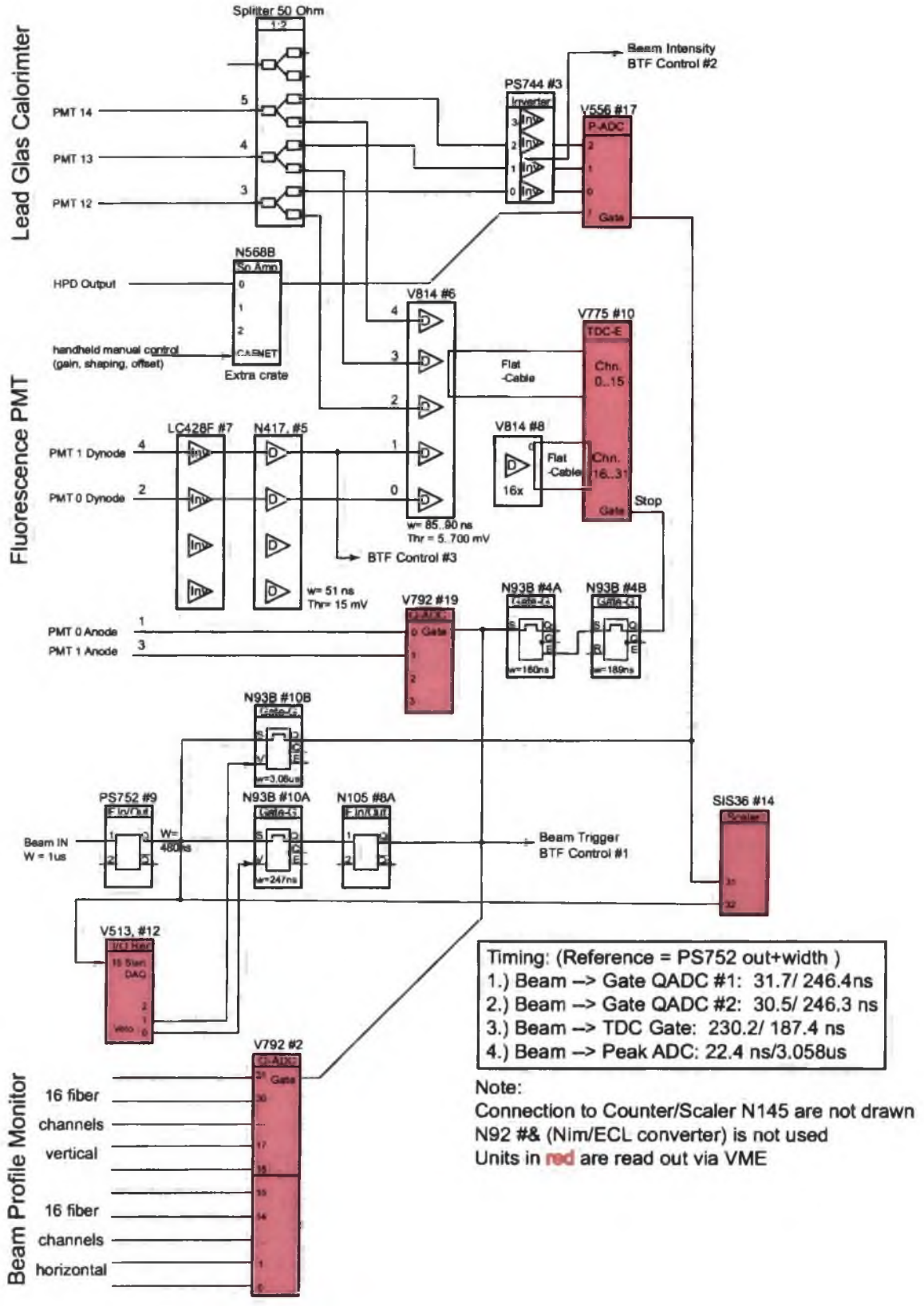

Fig. 24. *Scheme of the* AIRFLY *data acquisition circuit [Kle04].*

was surrounded by a lead shield. The following procedure was adopted: the chamber was evacuated, flushed for a while and then refilled by the desired gas to approximately normal pressure and closed, then the chamber was cooled down to the lowest achievable temperature. The measurement was done during the slow spontaneous reheating of the chamber. Remotely controlled filter-wheel allowed to insert 337 nm , UG6 (see Fig. 22 for the UG6 filter transmittance curve) or a blind (measurement of background) filter during the measurement. Scheme of the temperature measurement setup is shown in Fig. 23.

Hybrid Photo Diode of AIRFLY

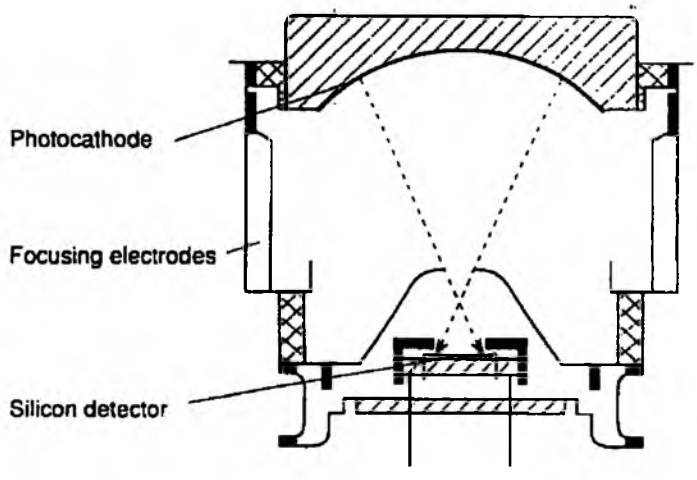

Fig. 25. *Scheme of a cross focused HPD.*

As the the main photodetector the AIRFLY experiment uses a HPD. It is essentially a vacuum tube with a photocathode on the entrance window and an electron lens that focuses the photoelectrons onto a Silicon PIN diode creating a number of electron-hole pairs. The charge is amplified by a low noise build-in pre-amplifier. Detailed discussion of HPD functioning and analysis is given in chapter 9.

AIRFLY experiment uses DEP cross focused HPD PP0475B with 40 mm S20UV photocathode on quartz window allowing observations in the near UV region. A sketch of a cross focused HPD is given in Fig. 25. The photocathode quantum efficiency given by the manufacturer is plotted in Fig. 26. The operating high voltage range is -10 to -15 kV and the whole interval was used in order to accommodate the dynamic range required. HPD features high photoelectron resolution (up to 14 resolved photoelectron peaks) allowing single and multi photon counting.

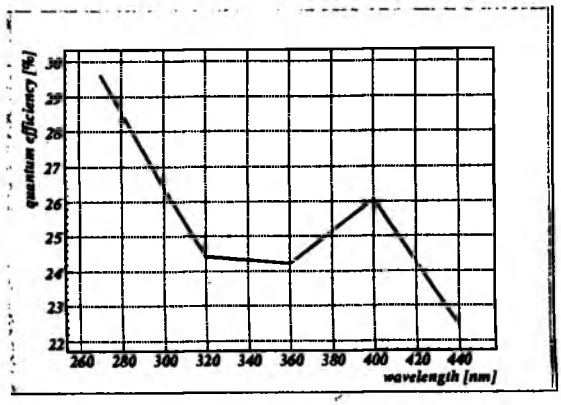

Fig. 26. *Quantum efficiency of the HPD photocathode given by the manufacturer.*

7.3 Spectrum measurement setup

The nitrogen fluorescence spectrum measurement was done in the Argonne National Laboratory, USA. The Van de Graaf accelerator of the Argonne Chemistry Division provides a high intensity electron beam (up to 10^{12} particles per bunch). The nominal energy of the electrons is 3 MeV but can be lowered to below 1 MeV if needed. The repetition rate is either 1 Hz – 1 kHz or a DC beam can be chosen.

The experimental setup is sketched in Fig. 27. The measurement was done using the same thin wall chamber as in Frascati and the same gas system. The spectrograph was placed away from the beam behind a concrete shielding to minimize the noise in the CCD and a 10 m long optical fiber was used to transport the signal from the chamber into the spectrograph. The measurement was done using a hard cladding multimode fiber BFH37-1500 (THORLABS) with broad range (300 – 1200 nm), 1500 μm core diameter and 0.37 numerical aperture. A spherical mirror was placed in the viewport in front of the fiber to enhance the light collection efficiency.

The spectrograph MS257 produced by L.O.T.-ORIEL with Andor CCD DV 420 was used to record the fluorescence spectra. The spectrograph, model 77700A, was equipped by a 1200line/mm grating blazed at 350nm (model 77742). Spectral resolution was 0.1nm. The CCD is formed by 1024 × 255 pixels of 26 × 26 μm^2 each. It was cooled down to −50 °C. The system has a reciprocal dispersion of 3.2 nm/mm, which – together with the 26 mm width of the CCD allows to record 85 nm interval at a time. Therefore the fluorescence region was measured in two parts 284 – 369 nm and 344 – 429 nm. The overlapping region was used to crosscheck the calibration.

The spectral response was calibrated using lines of a mercury pencil lamp (ORIEL 60635) and then refined by including the most prominent fluorescence lines.

The spectral sensitivity of the system was determined using a NIST[1] calibrated halo-

[1] National Institute of Standards and Technology

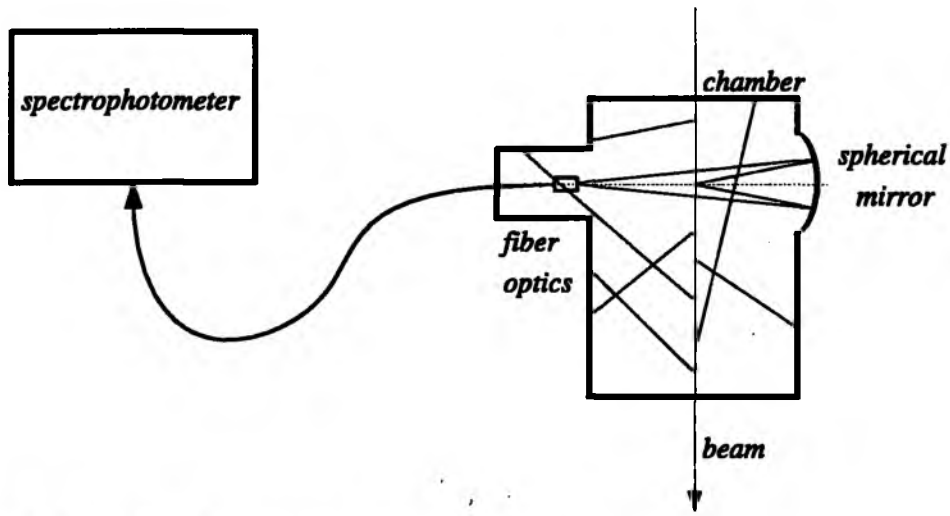

Fig. 27. *Setup for the spectrophotometer measurements.*

gen lamp (ORIEL, 63350-M, 200W). The power radiated into a unit wavelength interval into 1 cm^2 located at the distance of 50 cm can be described by a function given by the manufacturer

$$I(\lambda) = \frac{\exp(A + \frac{B}{\lambda})}{\lambda^5}\left(C + \frac{D}{\lambda} + \frac{E}{\lambda^2} + \frac{F}{\lambda^3} + \frac{G}{\lambda^4}\right) \tag{36}$$

plotted in Fig. 28.

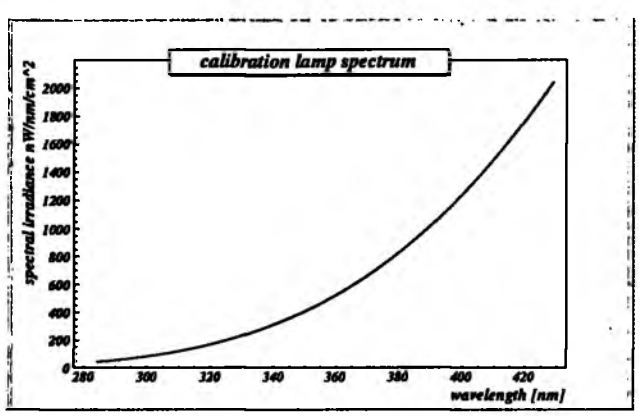

Fig. 28. *Spectrum of the calibrated lamp given by the manufacturer.*

The calibration was done in situ between the air fluorescence measurements. The lamp was placed at different positions along the beam to account for the spacial distribution of the fluorescence emission and the resulting spectra were suitably combined and compared to the original lamp spectrum to derive the final calibration factors. Comparison of lines in the overlapping region after calibration yields a 2% difference in the measured intensities, which was taken as an estimate of the systematic error of the relative calibration procedure.

8 Detector simulation

A complete simulation of the experimental setup was done using GEANT4.7.1.p01 simulation package [GEA04]. The main objectives of the simulations are:

- determination of the detector field of view and energy deposit.
- the determination of the geometrical factors for the absolute FLY measurement.
- understanding the systematic uncertainties of the experiment.

The structure of the whole simulation can be divided into two main parts. The first part are the input classes containing three main modules: the detector construction, the description of the primary particle and a list of physics processes and particles that will be taken into account during the simulation. These three classes are mandatory.

The second part represents a list of actions that have to be taken before or after each step, track, event or run, where the user is free to implement any operation that has to be taken during or immediately after the simulation procedure.

Detector construction

This class contains all the geometrical components present in the experiment as they were described in the previous chapter including the definition of the materials they are made of. The volumes included in their real dimensions and distances are: the cylindrical chamber with beryllium entrance and exit windows, the Čerenkov mirror, the filter, the aperture limits, baffles and the photocathode (see Fig. 29). The full response of the HPD is not simulated. Also implemented were the calorimeter, scintillator palette and the fiber profilometer.

Reflectivity of surfaces is also defined in this module as well as the indices of refraction of the transparent materials. The wavelength dependent index of refraction taken from the reference [ESO02] can be expressed as

$$(n_s - 1) \times 10^6 = 64.328 + \frac{29498.1 \times 10^{-6}}{146 \times 10^{-6} - (1/\lambda)^2} + \frac{255.4 \times 10^{-6}}{41 \times 10^{-6} - (1/\lambda)^2}, \qquad (37)$$

where n_s is the index of refraction of air at $p_s = 1013.25$ hPa, $T_s = 288.15$ K (15 °C) and the wavelength λ is expressed in nm. For other temperatures and pressures the refractive

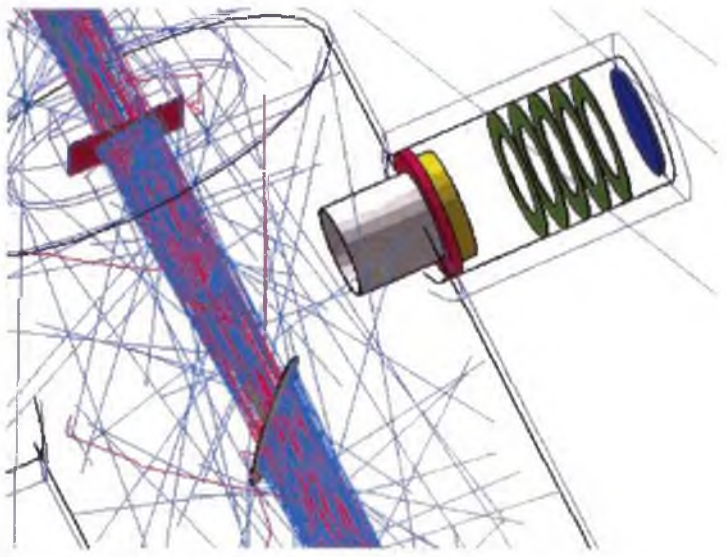

Fig. 29. *Geant4 simulation of the detector acceptance in fluorescence mode. Red trajectories represent negative particles - electrons, green trajectories are gamma photons and pale blue are optical photons.*

index of dry air n_d can be recalculated as

$$(n_d - 1) = (n_s - 1)\frac{p}{T}\frac{T_s}{p_s}. \tag{38}$$

Primary particle generation

The beam of primary particles is simulated from the point were the particles are leaving the beam pipe, i.e. right in front of the beryllium entrance window. The shape of the beam is adjusted so that it reproduces the profile measured at the profilometer for each type of measurement. Starting positions sampled from a uniform rectangle and a Gaussian divergence of 3 mrad were found to best reproduce the measured beam profile at lower intensities ($\sim 2000\,e^-$/pulse). Rectangular shape of the beam exiting the beam pipe is assumed because of the vertical and horizontal slits that are inserted into the beam to limit the number of particles.

Physics list

The AIRFLY scientific case requires simulations of energy losses and secondary particle production in the range from about 800 MeV down to the lowest possible energies. The particles present in the simulation are practically only electrons, positrons, gamma particles and optical photons (in GEANT4 considered as distinct from gamma).

The PENELOPE Physics package available within GEANT4, which claims to be valid from 250 eV up to 1 GeV, was found to be best suited for the purpose. PENELOPE [PEN06] stands for PENetration and Energy LOss of Positrons and Electrons.

The Monte Carlo simulation algorithm is based on a scattering model combining numerical databases with analytical cross section models.

The physics processes registered in the simulation include:

- for gamma
- G4PenelopeGammaConversion
- G4PenelopeCompton
- G4PenelopePhotoElectric
- G4PenelopeRayleigh

- for electrons and positron
- G4MultipleScattering
- G4PenelopeIonisation
- G4PenelopeBremsstrahlung
- G4PenelopeAnnihilation

- for optical photons
- G4OpBoundaryProcess
- G4Scintillation (Fluorescence)
- G4Cerenkov

Optical absorption and Rayleigh scattering can be neglected due to the small dimensions of the experiment. Cuts for production of secondary particles was set to 250 eV.

The scintillation class used to simulate the fluorescence process emits photons isotropically in proportion to the energy deposit sampled from a given spectrum. The scintillation yield was set to 19 photons per MeV of energy deposit, which leads to the production 4.17 ph/m/e^- between $300 - 400$ nm in a 1 m^3 of air. The relative fluorescence spectrum used in the simulation has been taken from the reference [Bun67].

8.1 Energy deposit in the field of view

In a thin target experiments such as AIRFLY it is important to take into account the fact that not all the energy lost by the passing particle is deposited inside the viewed volume. Depending on the energy, δ-electrons may carry away part of the energy. This effect becomes further enhanced when the pressure is lowered. At the first approximation, the energy deposit is proportional to the density and, if the temperature stays constant, also to the pressure. Deposit correction, i.e. deviation from this proportionality has to be determined and applied to each pressure point.

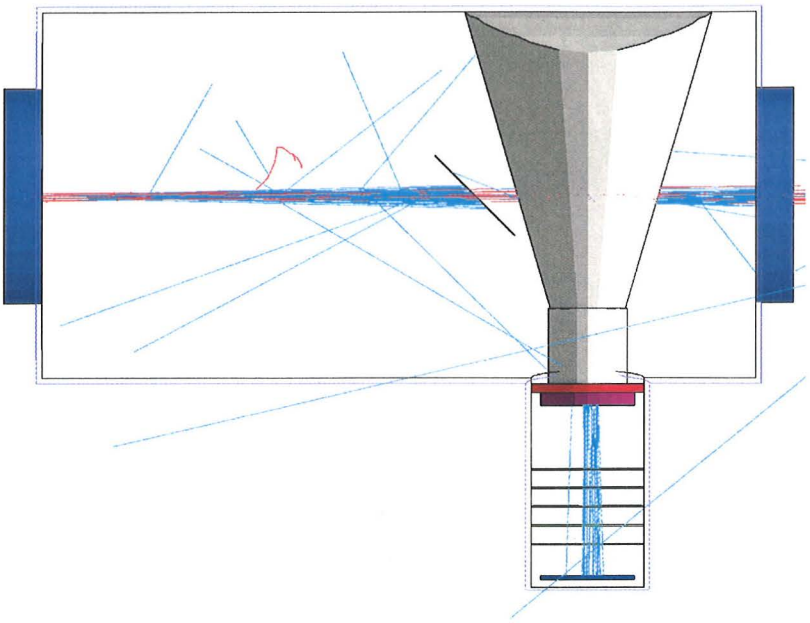

Fig. 30. *GEANT4 simulation of the detector field of view (the grey shaded region).*

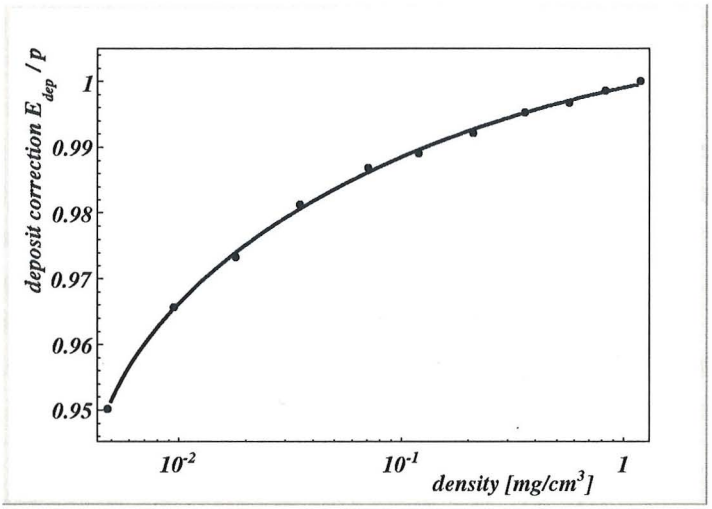

Fig. 31. *Simulation of the dependence of energy deposit on the density inside the chamber at* 350 MeV *(points) and the elliptical arc fit (solid line).*

The field of view volume (see Fig. 30) was obtained as an envelope of all starting points of the photons that were able to pass the geometrical acceptance and reach the photocathode. The energy deposit is then calculated as the sum of all the energy deposited inside this volume by primary and secondary particles at each pressure step. The resulting

dependence can be approximated by an elliptical arc

$$\frac{E_{dep}}{p} = A + B\sqrt{R^2 - (\log\frac{p}{p_0})^2}, \tag{39}$$

where A, B, R, p_0 are fitted constants. Simulated data for 350 MeV together with the fitted function are plotted in Fig. 31.

8.2 Fluorescence and Čerenkov mode

The Čerenkov process is implemented in GEANT4 and, when registered, it is automatically invoked for all the materials for which the refractive index was defined. As this process is well known analytically, it can be used for calibrations and testing of the detector performance. Verification of the simulated geometry by comparison of the number of Čerenkov photons detected in the simulation and in the real experiment will be given in chapter 10.

The Čerenkov light is well collimated within a few degrees around the beam so that by inserting a 45° mirror practically all the light is redirected into the detector, whereas the fluorescence is emitted isotropically and consequently only a very small part of photons reaches the photocathode. Distributions of arrival directions on the photocathode in the two modes are shown in Fig. 32. For the absolute measurement method, which relates the fluorescence emission to the Čerenkov production, these geometrical factors have to be simulated. (The method is discussed in detail in section 11.4.)

In typical conditions relevant for the absolute measurement, in 1 million of electrons sent, 2.46 Čerenkov photons are created per electron passing the 6 cm path between the black screen and the mirror (see Fig. 20. The mirror reflectivity takes away 16 % of the photons, the filter transmittance reduces the number of photons to 0.0610 per electron and after the quantum efficiency inclusion 0.0148 photons per electron are detected.

In the fluorescence case only 6×10^{-4} ph/e$^-$ generated in the field of view have the correct geometry to reach the photocathode and only 1.971×10^{-5} ph/e$^-$ pass the filter transmittance and quantum efficiency cuts.

The ratio of fluorescence to Čerenkov signal simulated at 18 °C, 993 hPa and 350 MeV will be

$$R_{sim} = 1.330 \times 10^{-3}. \tag{40}$$

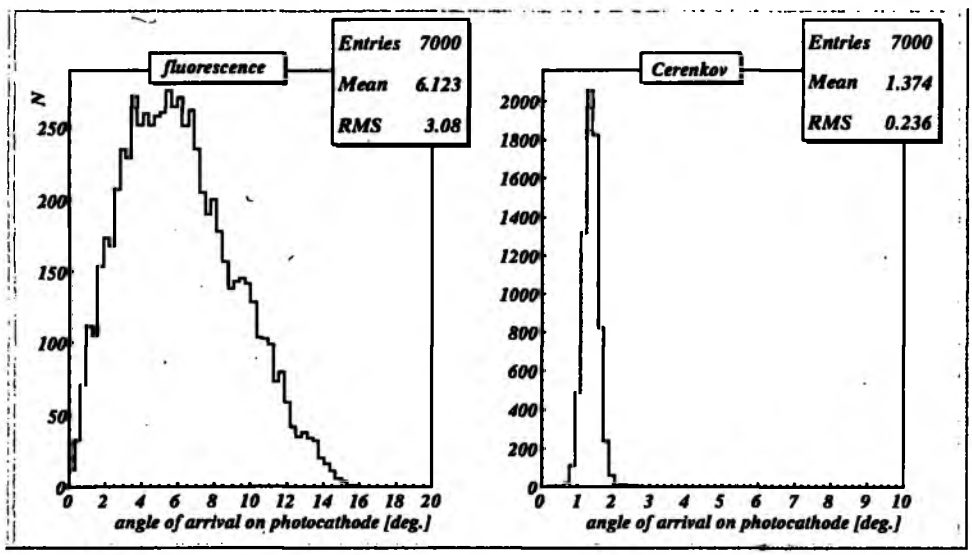

Fig. 32. *Simulated distribution of photon arrival directions on the photocathode.*

8.3 Study of systematic effects

Systematic uncertainties such as beam position and shape, slight misalignment of the components (mirror, detector), etc. influence the resulting absolute fluorescence yield. These effects have been studied in simulations, when the nominal values were altered by a realistic amount. In the Čerenkov mode a large effect was found when the mirror was placed at 46° instead of 45°. It amounts to 4.3 %. Prolongation of the path, where the photons are produced by 1 mm augments the number of detected photons by 1.7 % as would be expected from purely geometrical considerations. Effects, such as moving the photocathode closer or further away from the beam by 1 mm or even displacing it by 2 mm along the beam have a small value (< 1 % of the detected photons). Beam related effects, such as 1 mm larger beam or a beam moved downwards by 5 mm with respect to the center of the field of view were also found to have a negligible impact on the detected Čerenkov signal.

A large systematic effect on the ratio of fluorescence to Čerenkov light could be caused by a photocathode nonuniformity. As the photocathode coverage in the two cases is quite different (see Fig. 33) a radially distributed decrease in efficiency would strongly influence the fluorescence signal, while the amount of detected Čerenkov light would alter only slightly. Results of two calibration measurements that will be described in sections 10.2 and 10.3, namely the number of measured Čerenkov photons per electron and the linearity of the Čerenkov pressure dependence allow for only a small nonuniformity on the edges of the photocathode. The model inserted into the simulation has a uniform central part, 17.5 mm in diameter. Then the efficiency decreases linearly down to 50 % at the edge of

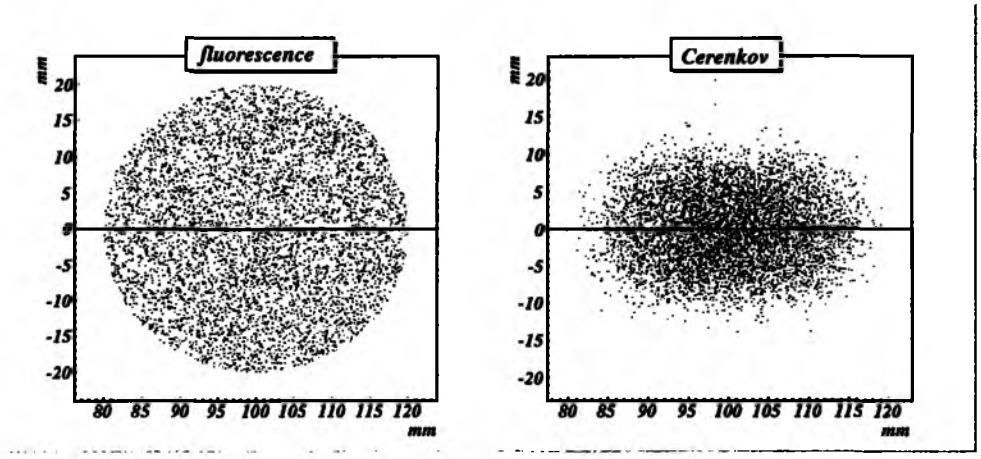

Fig. 33. *Simulated distribution of arrival points on the photocathode.*

the photocathode (20 mm diameter). This kind of nonuniformity would cause a 5 % effect on the fluorescence to Čerenkov ratio.

9 Hybrid PhotoDiode

Hybrid photodiodes are low noise, high resolution devices using a solid state diode as a multiplication element instead of a dynode-based cascade multiplication. The idea of using semiconductor as a signal translator was patented in the U.S. already 1954 (patent no. 2,691,076). The first HPD's, i.e. phototubes with reverse biased silicon diodes were produced in 1965 [Kal66]. In 1971 Beaver and McIlwain obtained a US patent for an HPD with an array of 38 diodes called *Digital multichannel Photometer*. Devices also using the proximity focusing mechanism were the 512-element-array DIGICON tubes developed in 1980-ties [Har82] for astronomical applications. DIGICON tubes were used in The Faint Object Spectrograph (1990-1997) of the Hubble Space Telescope [Jor99].

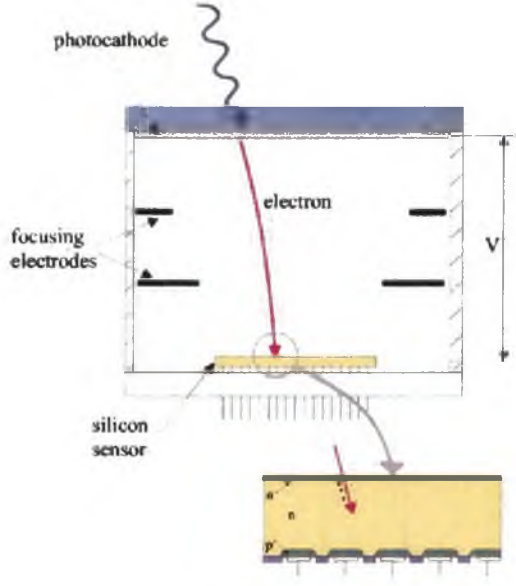

Fig. 34. *Schema of the principle of operation of HPD [Jor99].*

In high energy physics the idea of an HPD was practically reinvented in 1987 by De Salvo while looking for a photodetector operable in strong magnetic fields [DeS87]. The first multipixel array inside a vacuum tube ISPA (Imaging Silicon Pixel Array) was developed at CERN in 1994. It had 16×64 pixels and was used for the readout of scintillating fibers. Presently, HPDs are commercially available form DEP (Delft Electronics

Products), Hamamatsu or INTEVAC. Special large area HPDs are being developed in CERN for the LHCb-RICH detector [Gys01]. Another area of employment of HPDs is astrophysics (Atmospheric Čerenkov Telescopes).

9.1 Principle of operation

Hybrid photodiode is essentially a vacuum tube with a photocathode deposited on the inner side of a transparent entrance window. Photoelectrons emitted by the photocathode are accelerated in a potential of about 15 kV directly onto a silicon detector. The electric field can be shaped by electrodes in order to fit the image of the photocathode to the silicon chip. Each photoelectron penetrating the depleted region of the semiconductor PN junction produces about 3500 electron-hole pairs, i.e. the gain of the HPD is

$$G = (\Delta V - E_0)/W_{e-h},$$

where $W_{e-h} = 3.6\text{eV}$ is an average energy needed for creation of an electron-hole pair in silicon and E_0 is energy ($\sim 1 - 2\,\text{keV}$) lost in non-active material of the silicon sensor. Thanks to the non-multiplicative character of the charge amplification the variation of the HPD gain is given by

$$\sigma_G = \sqrt{GFn}$$

where $F \sim 0.1$ is the Fano factor for silicon and n is the number of photoelectrons. These fluctuations are generally small so that the energy resolution of the HPD is given by the noise of the readout electronics.

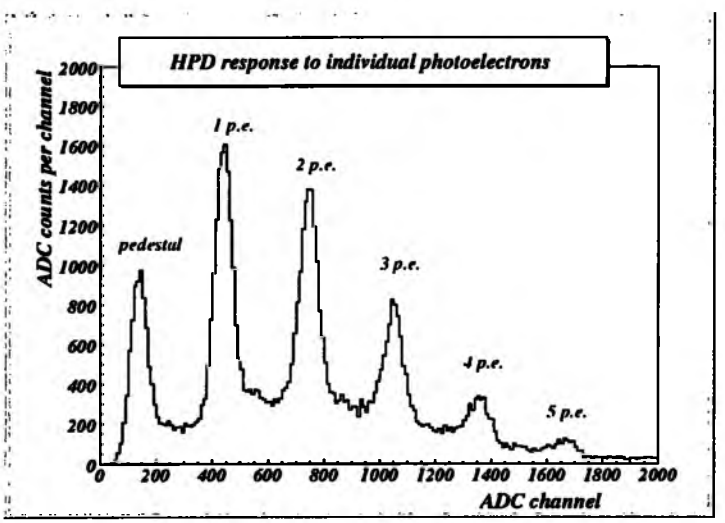

Fig. 35. *Example of an HPD response to individual photoelectrons.*

Another feature that affects the resolution has to be taken into account. Electrons bombarding the silicon with the energy of $\sim$ 15keV have a probability $\alpha \sim 0.2$ to backscatter into the vacuum depositing only part of their energy in the silicon. This effect gives rise to the continuum background on the low energy side of each peak as can be seen in Fig. 35. For a large average number of photoelectrons this effect practically prevents the individual photon counting.

Consequently, when modeling the HPD response, the supposedly Poisson distribution of the number of photoelectrons created by each beam bunch has to be modified to account for the backscattered part.

9.2 Model of detector behavior

Probability distribution function (p.d.f.) of the energy deposited by one photoelectron (and thus ADC response) is called *Single electron response (SER)* and denoted $r(\eta; a)$, where η is the deposited energy relative to the response of a fully absorbed photoelectron and a represents a set of detector dependent parameters. Schematic view of SER is shown in Fig. 36. Fully absorbed electrons constitute the forward peak, while backscattered electrons deposit only part of their original energy and contribute to the backscatter lobe.

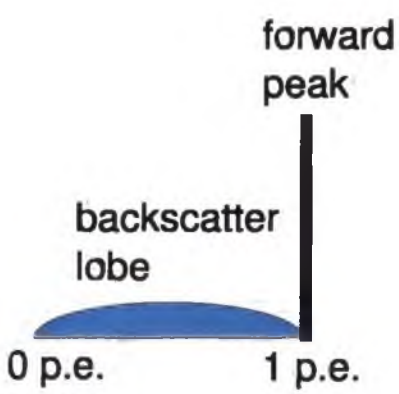

Fig. 36. *Schematic view of a single photoelectron response.*

The response of an HPD to Poisson-distributed photoelectrons was described by Tabarelli [Tab97] and it is given here for completeness.

One can assume that HPD is a linear device in the generated signal, e.g. each photoelectron generates a signal independently of others. Under this hypothesis a p.d.f. of two photoelectron response $r_2(\eta; a)$ is obtained by convolution

$$r_2(\eta; a) = \int r(y; a)\, r(\eta - y; a) \mathrm{d}y. \qquad (41)$$

Analogically a response of k photoelectrons has a p.d.f.

$$r_k(\eta; a) = \int r_{k-1}(y; a)\, r(\eta - y; a) \mathrm{d}y. \qquad (42)$$

As the number of photoelectrons generated on a photocathode follows the Poisson statistics, i.e. the probability that k photoelectrons are generated is

$$P(k) = e^{-\mu} \frac{\mu^k}{k!},$$

the total response has the p.d.f

$$\sum_{k=0}^{\infty} e^{-\mu} \frac{\mu^k}{k!} r_k(\eta; a) \tag{43}$$

The signal has to be further convoluted with the response of the readout electronics $g(\eta; b)$, where b is a set of parameters describing the function. The response is generally described by a Gaussian distribution. The resulting p.d.f. reads

$$s(\eta; \mu, a, b) = \sum_{k=0}^{\infty} e^{-\mu} \frac{\mu^k}{k!} r_k(\eta; a) \star g(\eta; b). \tag{44}$$

Direct evaluation of convolutions, moreover k-fold convolutions in an infinite sum is extremely demanding in terms of computing time. This difficulty can be elegantly overcome by evaluation of the convolutions in the Fourier domain. Let us define the Fourier transformation of $s(\eta; \mu, a, b)$ as

$$S(\omega; \mu, a, b) = \int e^{-i\omega\eta} s(\eta; \mu, a, b) \mathrm{d}\eta \tag{45}$$

and denote

$$R(\omega; a) = \int e^{-i\omega\eta} r(\eta; a) \mathrm{d}\eta \ , \quad G(\omega; b) = \int e^{-i\omega\eta} g(\eta; b) \mathrm{d}\eta \tag{46}$$

Substituting (44) into (45), as there exists an integrable mayorant it is possible to change the order of summation and integration and make use of the fact that a Fourier transformation of a convolution is a product of Fourier transformations. That is in our case

$$\int r_k(\eta; a) \star g(\eta; b) \ e^{-i\omega\eta} \mathrm{d}\eta = R^k(\omega)\, G(\omega) \tag{47}$$

and thus

$$\begin{aligned} S(\omega; \mu, a, b) &= \sum_{k=0}^{\infty} e^{-\mu} \frac{\mu^k}{k!} \ R^k(\omega) \ G(\omega) = e^{-\mu} \underbrace{\left(\sum \frac{\mu^k}{k!} \ R^k(\omega) \right)}_{\exp(\mu R(\omega))} G(\omega) \\ &= e^{\mu(R(\omega)-1)} G(\omega) \end{aligned} \tag{48}$$

The resulting p.d.f. is obtained by inverse Fourier transform. By this procedure the laborious numerical calculation of the convolutions and of the infinite sum is avoided.

Single Electron Response function

Next, we need to introduce a suitable parameterization of the SER function. SER is composed of two parts — a forward part r_f and a backward part r_b — in the following way:

$$r(\eta) = \alpha r_b(\eta) + (1 - \alpha) r_f(\eta) \tag{49}$$

where α denotes the backscattering probability.

For the backscattering part the model proposed by Damkjaer [Dam82] is adopted. The model was obtained by analysis of the experimental response of a silicon surface barrier detector to monoenergetic electrons. The expression can be written as

$$r_b(\eta) = \begin{cases} A_1 \dfrac{\sin^2(a_1\pi(1-\eta))}{1+a_2\exp(-28.5\eta^2)} & \eta \leq 1, \\ 0 & \eta > 1, \end{cases} \tag{50}$$

where a_1, a_2 are parameters to be determined from the fit and A_1 is a normalization factor adjusted so that the $\int r_b(\eta)\mathrm{d}\eta = 1$.

For the forward peak Damkjaer suggested a Gaussian shape. Tabarelli generalized the model in the following way

$$r_f(\eta) = A_2 \begin{cases} \left(1+\left(\dfrac{\eta-1}{\sigma_{SER}}\right)^2/a_3\right)^{-(a_3+1)/2} & \eta \leq 1, \\ \exp\left(-\dfrac{(\eta-1)^2}{2\sigma_{SER}^2}\right) & \eta > 1, \end{cases} \tag{51}$$

where σ_{SER} is a width of the Gaussian and a_3 broadens the peak on the low energy side. For large values of a_3 the distribution converges to the Gaussian while for small a_3 the curve is asymmetric with a low energy tail. A normalization factor A_2 is chosen so that $\int r_f(\eta)\mathrm{d}\eta = 1$.

Width of peaks is dominantly governed by electronic noise $g(\eta; b)$, which is modeled by a Gaussian of width σ_{PED}.

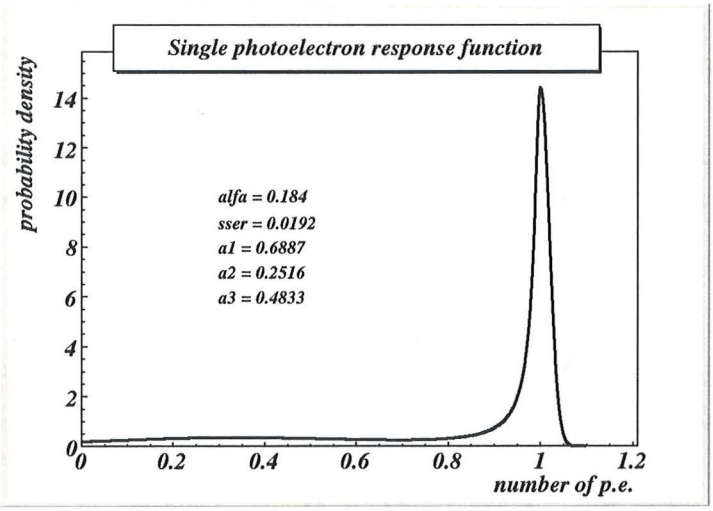

Fig. 37. *Best fit of the single photoelectron response for our HPD.*

Finally we need to describe a relation between the number of photoelectrons η and ADC channels Sig_{ADC} determined. As it is supposed that this relation is linear, we use an expression

$$Sig_{ADC} = Sig_{PEDE} + \frac{\eta}{f_{CONV}}, \tag{52}$$

where Sig_{PEDE} and f_{CONV} are the last parameters to be determined. Sig_{PEDE} is a position of the pedestal and $\frac{1}{f_{CONV}}$ is a distance between subsequent forward peaks in ADC channels.

All together we have the following nine parameters to determine: mean number of photoelectrons μ, parameters of the SER function a_1, a_2, a_3, α and σ_{SER}, pedestal width σ_{PED} and transformation parameters Sig_{PEDE} and f_{CONV}.

Maximum likelihood approach

To find an optimal set of parameters we need to quantify how a particular set of parameters differs from the optimal one. Let us suppose that we have n ADC channels and let us denote s_i a theoretical probability that the value i is measured. Obviously, it holds that

$$\sum_{i=1}^{n} s_i = 1.$$

Performing N measurements gives y_i realizations of the value i,

$$\sum_{i=1}^{n} y_i = N.$$

Probability that for a given theoretical probabilities $\{s_i, i = 1..n\}$ a particular realization $\{y_i, i = 1..n\}$ is obtained is

$$P(y_i; s_i) = \binom{N}{y_1, y_2, \dots y_n} \prod_{i=1}^{n} s_i^{y_i}, \tag{53}$$

where a combination number is introduced

$$\binom{N}{y_1, y_2, \dots y_n} = \frac{N!}{y_1!\, y_2!\, \dots y_n!}.$$

We applied the Maximum Likelihood approach, i.e. conversely for a given realization $\{y_i\}$ we find parameters (e.g. SER parameters, μ etc.) governing $\{s_i\}$ so that $P(y_i; s_i)$ is maximal. For practical reasons, instead of maximizing $P(y_i; s_i)$, we minimize an expression

$$-\log P(y_i; s_i) = -\log \binom{N}{y_1, y_2, \dots y_n} - \sum_{i=1}^{n} y_i \log s_i \ .$$

For reasons clarified later, the term

$$-\log\binom{N}{y_1, y_2, \ldots y_n} - \sum_{i=1, y_i>0}^{n} y_i \log \frac{y_i}{N}$$

independent of the theoretical probabilities s_i is subtracted, the symbol $y_i > 0$ means that only indices i with $y_i > 0$ are included in the sum. A final form of a minimized function is

$$L(s_i; y_i) = \sum_{i=1, y_i>0}^{n} y_i \log \frac{y_i}{N s_i} \,. \tag{54}$$

It is interesting to note the relation between the Maximum Likelihood and a χ^2 approach. We use an expansion of a logarithm into a Taylor series

$$\log(x + \Delta) = \log x + \frac{\Delta}{x} - \frac{\Delta^2}{2x^2} + \frac{\Delta^3}{3x^3} - \ldots$$

It is convenient to put $x = \frac{y_i}{N}$ and $\Delta = s_i - \frac{y_i}{N}$ (as the mean of y_i is Ns_i). Then $\log s_i$ can be expressed as

$$\log s_i = \log \frac{y_i}{N} + \frac{s_i - \frac{y_i}{N}}{\frac{y_i}{N}} - \frac{(s_i - \frac{y_i}{N})^2}{2(\frac{y_i}{N})^2} + \ldots \tag{55}$$

Substituting (55) into rearranged expression of (54)

$$L = \sum_{i=1, y_i>0}^{n} y_i [\log \frac{y_i}{N} - \log s_i]$$

we get

$$L = \sum_{i=1, y_i>0}^{n} y_i \log \frac{y_i}{N} - \sum_{i=1, y_i>0}^{n} y_i \left[\log \frac{y_i}{N} + \frac{s_i - \frac{y_i}{N}}{\frac{y_i}{N}} - \frac{(s_i - \frac{y_i}{N})^2}{2(\frac{y_i}{N})^2} + \ldots\right] \tag{56}$$

It is obvious, that the constant term of the logarithm expansion cancels out. The linear term vanishes because of $\sum s_i = 1$ and $\sum y_i = N$. The first non-vanishing term is the quadratic one

$$L_2 = \sum \frac{(Ns_i - y_i)^2}{2y_i}, \tag{57}$$

which can be identified with a χ^2 sum (because the variance of y_i distribution is equal to its mean, which can be estimated by y_i).

A subsequent term in the series (56)

$$L_3 = -\sum \frac{(Ns_i - y_i)^3}{3y_i^2}$$

is suppressed with respect to L_2 by a factor proportional to

$$\frac{Ns_i - y_i}{y_i} \approx \frac{1}{\sqrt{y_i}}.$$

This confirms a statement that for a large N, maximum likelihood converges to χ^2. However, in our case values of y_i are moderate so it is not desirable to apply such a simplification. Using the form (54) of $L(s_i; y_i)$ it is possible to eliminate a large constant term $\sum y_i \log(y_i/N)$, which would deteriorate numerical calculations.

Mean of the distribution

For a larger number of photoelectrons the individual peaks become to overlap as for a very large μ the Poisson distribution tends to the Gaussian. In this case the spectrum cannot be reliably fitted because the parameters μ, f_{CONV}, α become strongly correlated. It is necessary to find a robust characterization of the distribution consistent in both modes.

The mean of the experimental and also of the model distribution is a convenient candidate. For the experimental data we define the mean as

$$\langle s \rangle_{exp} = \sum_{i=1}^{n} i \frac{y_i}{N}. \tag{58}$$

For the model

$$\langle s \rangle_{mod} = \int s(\eta)\, \eta \, \mathrm{d}\eta, \tag{59}$$

and using the relation (52) we can transform from the units of p.e. into ADC channels to compare with the experimental data (58).

$$\langle s \rangle_{ADC} = Sig_{PEDE} + \frac{\langle s \rangle_{mod}}{f_{CONV}}$$

The mean of the model can be calculated analytically. Derivation of the characteristic function (45) gives (we can exchange the order of derivation and integration as there exists an integrable mayorant)

$$i\frac{\mathrm{d}S}{\mathrm{d}\omega}(0) = \int s(\eta)\ \eta\ \mathrm{d}\eta \tag{60}$$

From (48) we have in our case

$$\frac{\mathrm{d}S}{\mathrm{d}\omega} = S(\omega)\mu R'(\omega) + \exp(\mu[R(\omega) - 1])G'(\omega).$$

As a consequence of the normalization of $s(\eta)$ and $r(\eta)$ it holds that $S(0) = R(0) = 1$, and analogically to (60) is

$$iR'(0) = i\frac{\mathrm{d}R}{\mathrm{d}\omega}(0) = \int \eta r(\eta)\mathrm{d}\eta = \langle r \rangle \quad , \quad iG'(0) = i\frac{\mathrm{d}G}{\mathrm{d}\omega}(0) = \int \eta g(\eta)\mathrm{d}\eta = \langle g \rangle$$

express the mean of SER and the mean of electronic noise, respectively. So we finally get

$$\langle s \rangle_{mod} = \langle g \rangle + \mu \langle r \rangle.$$

The noise distribution is generally supposed to be symmetric, so $\langle g \rangle = 0$. The mean of SER $\langle r \rangle$ has to be integrated numerically.

The final expression for calculation of the mean out of the fitted parameters reads

$$\langle s \rangle_{ADC} = Sig_{PEDE} + \frac{\mu \langle r \rangle}{f_{CONV}}. \tag{61}$$

For the correct parameter set the model mean value $\langle s \rangle_{ADC}$ has to be close to the experimental $\langle s \rangle_{exp}$.

Estimation of the Poisson distribution

Many of the measured distributions have Poissonian statistics, therefore it is convenient to derive the expresion for the estimate of the mean value and its statistical error.

Suppose that P_μ is a Poisson distribution with an uknown mean value μ. There are N samples $\{k_i, i = 1..N\}$ of this distribution and it is desirable to estimate μ by the Maximum Likelihood approach.

Probability of realization of a particular set of samples $\{k_i\}$ is given by the expression

$$P(k_i;\mu) = \prod_{i=1}^{N} P_i(k_i;\mu), \qquad \text{where} \qquad P_i(k_i;\mu) = \mathrm{e}^{-\mu} \frac{\mu^{k_i}}{k_i!}. \tag{62}$$

The Maximum-Likelihood estimate $\hat{\mu}$ of an uknown mean μ maximizes the probability (62) as a function of μ. As the logarithm is a monotone function, an extreme of $P(k_i;\mu)$ is reached for the same value μ as the extreme of $\log P(k_i;\mu)$, so the probability $P(k_i;\mu)$ is maximal when

$$\left. \frac{\partial \log P(k_i;\mu)}{\partial \mu} \right|_{\mu=\hat{\mu}} = 0. \tag{63}$$

The term $\log P(k_i;\mu)$ can be simplified as

$$\log P(k_i;\mu) = \log \prod_{i=1}^{N} P_i(k_i;\mu) = \sum_{i=1}^{N} \log P_i(k_i;\mu) = -N\mu + \sum_{i=1}^{N} k_i \log \mu - \sum_{i=1}^{N} \log(k_i!).$$

The derivative is then

$$\frac{\partial \log P(k_i;\mu)}{\partial \mu} = -N + \sum_{i=1}^{N} k_i \frac{1}{\mu},$$

which is equal to zero for

$$\hat{\mu} = \sum_{i=1}^{N} \frac{k_i}{N}.$$

The samples k_i are random quantities, thus $\hat{\mu}$ is a random quantity as well and it is possible to calculate its mean value $\mathrm{E}\,\hat{\mu}$ and variance $\mathrm{var}\,\hat{\mu}$:

$$\mathrm{E}\,\hat{\mu} = \sum_{i=1}^{N} \frac{\mathrm{E}\,k_i}{N} = \sum_{i=1}^{N} \frac{\mu}{N} = \mu,$$

where it holds that $\mathrm{E}\,k_i = \mu$. This states that the estimate $\hat{\mu}$ is unbiased.

From the definition of variance it can be derived that

$$\mathrm{var}\,\hat{\mu} = \mathrm{E}(\hat{\mu}^2) - (\mathrm{E}\,\hat{\mu})^2 = \sum_{i,j=1}^{N} \frac{\mathrm{E}\,k_i k_j}{N^2} - \mu^2. \tag{64}$$

The samples k_i are mutually independent, therefore

$$\mathrm{E}\,k_i k_j = \begin{cases} \mathrm{E}\,k_i^2 = \mathrm{var}\,k_i^2 + (\mathrm{E}\,k_i)^2 = \mu + \mu^2 & \text{for } i = j \\ \mathrm{E}\,k_i k_j = \mathrm{E}\,k_i\,\mathrm{E}\,k_j = \mu^2 & \text{for } i \neq j \end{cases}$$

Substituing this into (64) leads to

$$\begin{aligned} \mathrm{var}\,\hat{\mu} &= \sum_{i=1}^{N} \frac{\mathrm{E}\,k_i^2}{N^2} + \sum_{i,j=1;i\neq j}^{N} \frac{\mathrm{E}\,k_i k_j}{N^2} - \mu^2 = \sum_{i=1}^{N} \frac{\mu+\mu^2}{N^2} + \sum_{i,j=1;i\neq j}^{N} \frac{\mu^2}{N^2} - \mu^2 = \\ &= N\frac{\mu+\mu^2}{N^2} + N(N-1)\frac{\mu^2}{N^2} - \mu^2 = \frac{\mu}{N} \end{aligned} \tag{65}$$

Standard deviation of the estimate $\hat{\mu}$ given as the square root of variance will then be

$$\sigma = \sqrt{\frac{\mu}{N}}. \tag{66}$$

Relative error of the estimate $\frac{\sigma}{\mu} = \frac{1}{\sqrt{\mu N}}$ scales down with the growing number of measurements N.

9.3 Fitting procedure

At this point we need to find a set of parameters so that the model function best describes the experimental data, i.e. to minimize a function of merit that quantifies the agreement between the model and data. It is natural to use the logarithmic likelihood (54) as the merit function but further limitations may be added in order to better localize the minimum.

Direct minimizing methods widely used, such as Simplex or conjugate gradient, are only able to go downhill towards the nearest minimum of the function. In our case the minimized function has many parameters with many local minima, where the conventional fitting routines get trapped. Therefore a new method was adopted capable of taking a step

back and jump out of a local minimum. Next objective was to use an open source library, which would make the code freely available to all users. The fitting routine fulfilling these requirements is the Simulated annealing, part of the GNU Scientific Library [GSL06].

Simulated annealing approach

Simulated annealing is a generalization of a Monte Carlo method for examining the equations of state and frozen states of n-body systems [Met53]. The concept is based on the manner in which liquids freeze or metals recrystallize in the process of annealing. A melt, initially at high temperature and disordered, is slowly cooled so that at any time the system is approximately in a thermodynamic equilibrium. As cooling proceeds, the system becomes more ordered and approaches a "frozen" ground state at $T = 0$. Hence the process can be thought of as an adiabatic approach to the lowest energy state.

The original Metropolis scheme was that an initial state of a thermodynamic system was chosen at energy E and temperature T, holding T constant the initial configuration is perturbed and the change in energy $\mathrm{d}E$ is computed. If the change in energy is negative the new configuration is accepted. If the change in energy is positive it is accepted with a probability given by the Boltzmann factor $\exp(-\mathrm{d}E/kT)$. This processes is then repeated sufficient number of times to give a good sampling statistics for the current temperature, and then the temperature is decremented and the entire process repeated until a frozen state is achieved at $T = 0$.

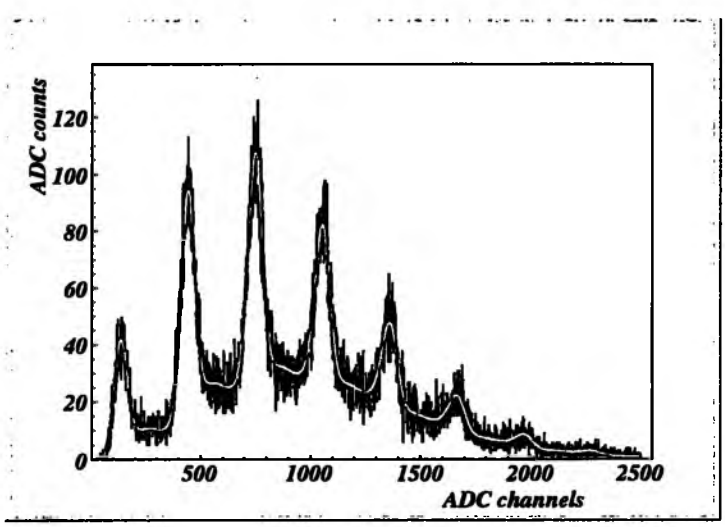

Fig. 38. *An example of HPD signal fitted by the Simulated annealing routine.*

By analogy with this physical process, each step of the SA algorithm replaces the current solution by a random "nearby" solution, chosen with a probability that depends on the difference between the corresponding function values and on a global parameter T

(called the temperature), that is gradually decreased during the process. The dependence is such, that the current solution changes almost randomly when T is large, but increasingly "downhill" as T goes to zero. The allowance for "uphill" moves saves the method from becoming stuck at local minima.

The current state of a thermodynamic system is analogous to a point in the parameter space of the fitted function. The current energy of the thermodynamic system is analogous to the current value of the function of merit, and ground state is analogous to the global minimum of the merit function. The major difficulty in implementation of the algorithm is that there is no obvious analogy for the temperature T with respect to a free parameter in the minimization task. It is crucial to select an appropriate "cooling scheme", i.e. initial and final temperature, the course of temperature decrease, number of iterations at each temperature. If the initial temperature of the system is too low or cooling is done insufficiently slowly the system may become quenched forming defects or freezing out in metastable states (ie. trapped in a local minimum energy state). Typical temperature decrease functions are $T(t) = T_0/\log t$, $T(t) = T_0/t$ or $T(t) = T_0 \exp(-t)$, where T is temperature and t is time. In our case the exponential decrease of temperature was adopted. An example of the HPD spectrum fitted by the Simulated annealing if shown in Fig. 38.

The GNU Scientific Library (GSL) is a numerical library for C and C++ programmers. It is free software distributed under the GNU General Public License. Apart from the Simulated annealing, the library provides a wide range of mathematical routines such as random number generators, special functions, least-squares fitting, etc. GSL package is a standard component of UNIX-like systems so the code is ready to run on majority of machines without the necessity of installing any additional software.

10 Calibration measurements

10.1 Properties of the optical components

Filter Transmittance

The angular dependence of the transmittance of the 337 nm interference filter was measured using the Lambda EZ210 UV/Vis Spectrophotometer at thirteen different incident angles between 0° and 20° in the wavelength interval 315 – 350 nm with 0.1 nm steps. Lambda EZ210 contains two silicon photodiodes. The deuterium source light is splitted by half mirror - one part of the beam passes through the sample into the first detector and the second one is driven directly to the second detector. The transmittance is then given as the ratio of transmitted versus reference signal. The results obtained are presented in Fig. 39 superimposed on top of a schematic nitrogen spectrum. The filter transmittance was also measured by another laboratory. Comparison of the two results is shown in Fig. 40. The small difference is probably caused by nonuniformity of the filter. A 2 % variation of the transmittance over the surface at 0° of incidence, at 337.1 nm was found.

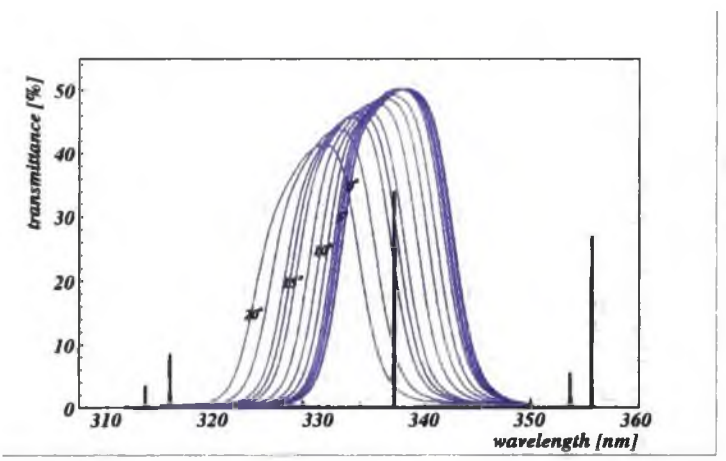

Fig. 39. *Measured filter transmittance at 13 angles between* 0° *and* 20°.

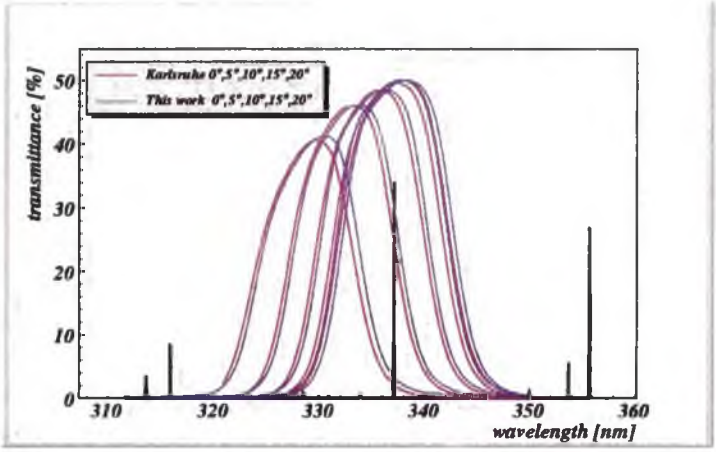

Fig. 40. *Filter transmittance - comparison of measurements from different laboratories.*

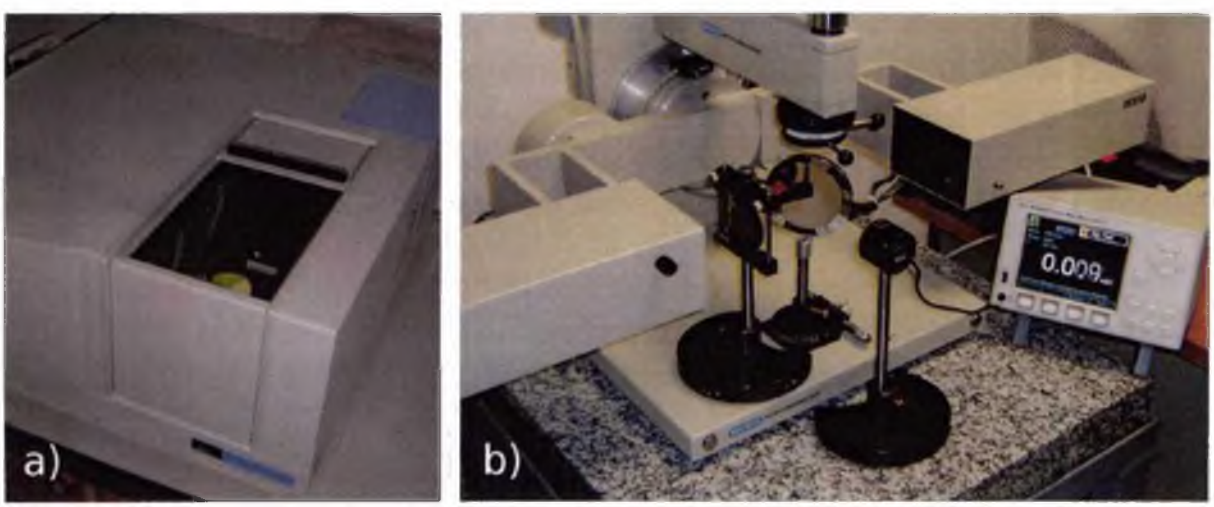

Fig. 41. *Filter measurement setup with Lambda EZ210 (a), mirror reflectivity measurement setup (b).*

Mylar mirror reflectivity

The reflectivity of the mylar mirror at 45° was measured in the simple setup sketched in Fig. 42. Xenon lamp was used as a light source with continuous spectrum. The light beam was well collimated into 2 mm spotsize at the level of the detector. The 337 nm narrow band interference filter, described in the previous subsection was used to select the desired part of the spectrum. A dual channel optical powermeter 2935T-C equipped with a detector head 918D-UV-OD3 (Newport, USA) was used. The silicon diode sensitive area was 1 cm^2. The ratio obtained for the reflected to direct light power was (84 ± 1) %. The reflectivity changes slightly, within the measurement precision, between 40° and 50° angle of incidence.

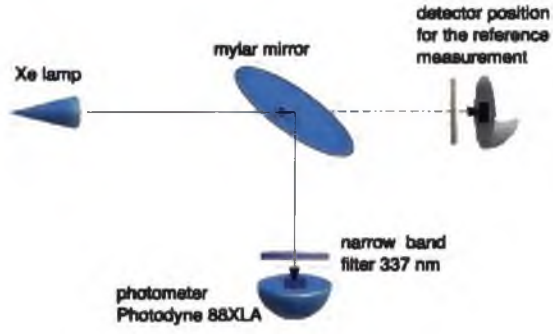

Fig. 42. *Experimental setup for the measurement of the mirror reflectivity.*

Estimation of the mylar thickness

The mylar transmittance was also measured (see Fig. 43, which allows to determine the optical thickness of the passed layer from the interference pattern. For any two successive maxima k and $k+1$ at wavelengths λ_1 and λ_2 it holds that $2dn = k\lambda_1$ and $2dn = (k+1)\lambda_2$, where $n = 1.65$ (DuPont) is the index of refraction and d is the thickness of the mylar. In our case the thickness was estimated at 15 microns.

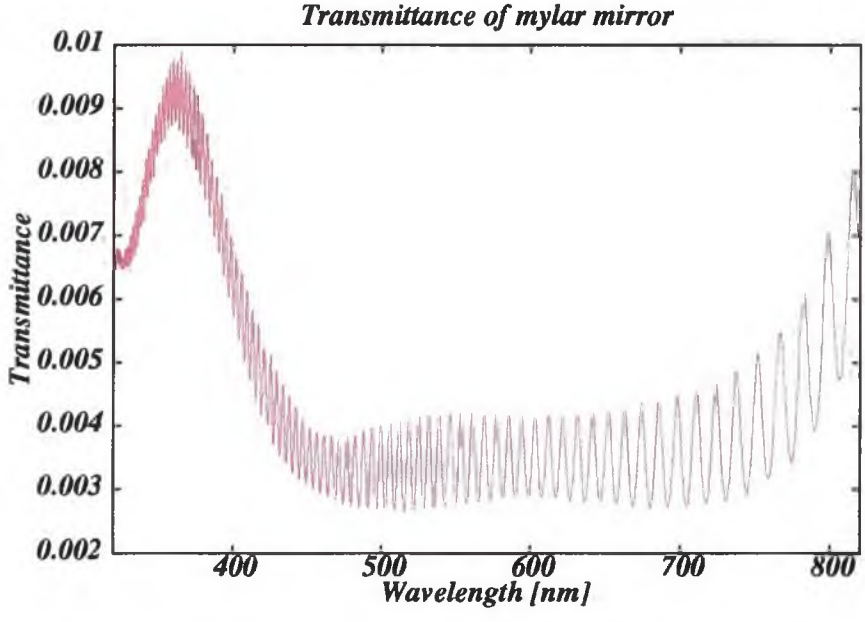

Fig. 43. *Measured transmittance spectrum of the mylar mirror.*

10.2 Čerenkov signal versus calorimeter

The number of Čerenkov photons detected per 350 MeV primary electron was experimentally measured. The measurement was done in pure nitrogen which has a slightly

higher index of refraction than air. The beam intensity was reduced to the point where it was possible to see individual electrons in the calorimeter and also single photoelectrons in HPD. The HPD signal was analyzed by fitting the backpulse model using the Simulated-Annealing method to the data. An example of data histogram from the calorimeter and corresponding signal in HPD are shown in Fig. 44. The background was estimated at 0.0021 p.e./bunch.

The calorimeter signal was analyzed in the following way: number of hits in each individual peak was multiplied by the corresponding number of electrons, summed up and divided by the number of bunches. Another approach is to fit a Poisson distribution into the number of hits for each peak. Average of three consecutive run yields 0.0158 ± 0.0003 photoelectrons/e^-.

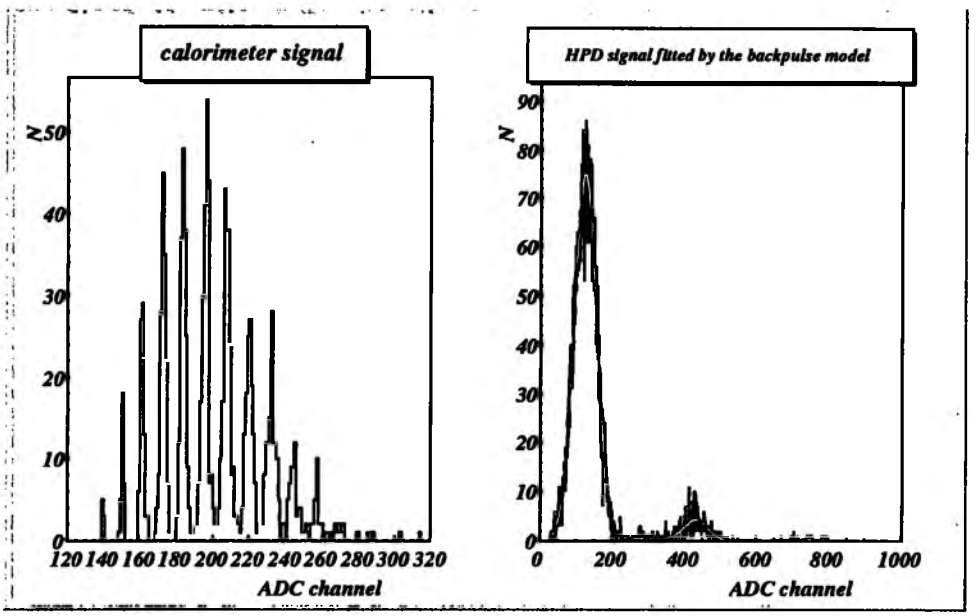

Fig. 44. *Calorimeter and the corresponding Čerenkov signal detected by HPD.*

This result can be used to verify the detailed simulation of the setup including the measured mirror reflectivity and filter transmittance Fig. 45. The filter transmittance is interpolated between the angles and wavelengths measured. The quantum efficiency of the HPD was set to the value reported by the manufacturer (24.3% at 337nm). The beam profile was adjusted to reproduce the response of the fiber profilometer signal in the real data. According to the simulation the average number of Čerenkov photons detected per a 350 MeV primary electron is 0.0152.

The agreement is fairly good, within two standard deviations.

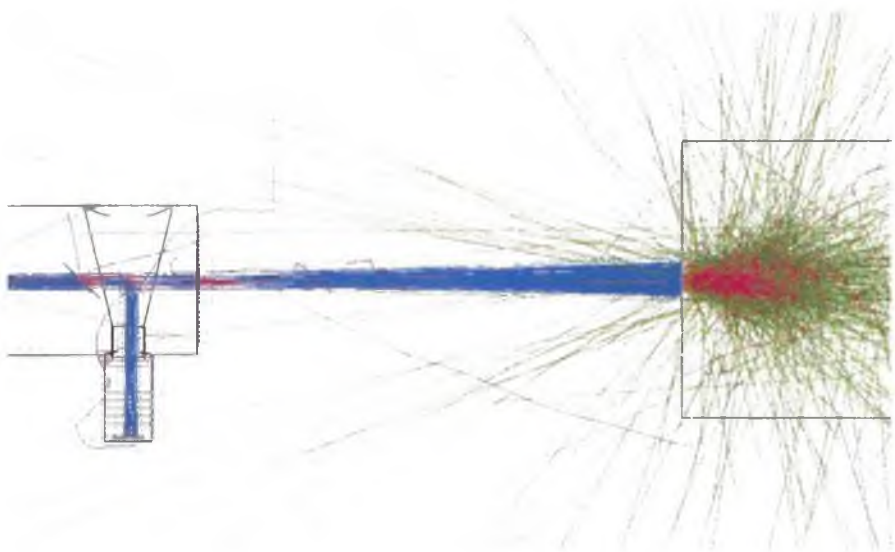

Fig. 45. *Geant4 simulation of the* AIRFLY *experiment in the Čerenkov mode.*

10.3 Čerenkov pressure dependence

This study was done to understand the detector systematic uncertainties, namely the photocathode uniformity. As the pressure decreases the Čerenkov light-cone becomes narrower and also the multiple scattering of electrons becomes smaller making the Čerenkov light spot covering a smaller part of the photocathode. The measured dependence of the Čerenkov signal on the pressure is shown in Fig. 46. A nonlinearity for high pressures would indicate that some Čerenkov photons are lost on the way to photocathode. Also a nonuniformity of the photocathode would spoil the linearity of this plot. From the good linearity of the Čerenkov pressure dependence Fig. 46 it is possible to deduce that the part of Čerenkov light falling outside of the photocathode is negligible and the nonuniformity, if any, should be limited to the very edges of the photocathode.

10.4 Čerenkov conversion

In the determination of the absolute fluorescence yield the aime is to compare the fluorescence and the Čerenkov yield. This method will be discussed in detail in chapter 11. The objective is to measure the two effects in the same configuration and beam intensity, switching between the two cases by insertion of a remotely controlled mirror into the chamber at 45° to the beam, thus redirecting the Čerenkov light into the detector. This section deals with the experimental determination of the Čerenkov conversion factor from ADC counts to photoelectrons.

As the Čerenkov signal strongly dominates over the fluorescence, it will not be possible to distinguish individual photoelectrons in the ADC histograms in both configurations.

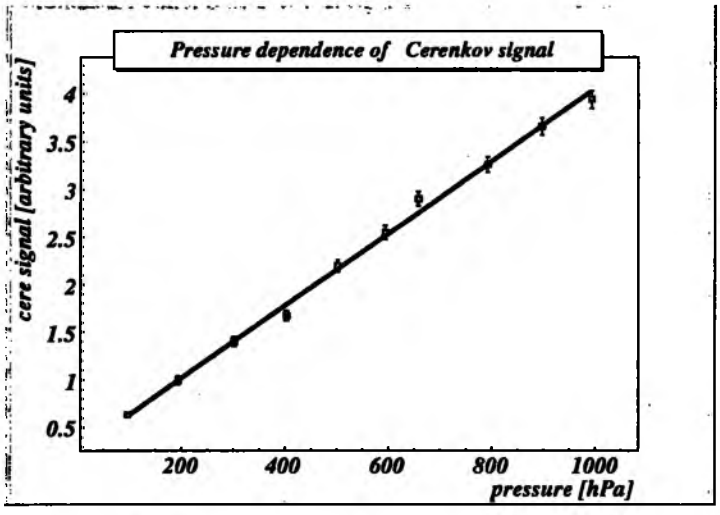

Fig. 46. *Dependence of the Čerenkov signal on pressure.*

For high N_{pe} the Poissonian distribution tends to a Gaussian and therefore fitting of the individual photoelectron peaks is no longer possible. However, N_{pe} can be determined from the mean of the distribution $\langle s \rangle_{ADC}$ (introduced in (61)) provided that the conversion factor $\frac{\langle r \rangle}{f_{conv}}$ is known. In order to improve the signal to noise ratio of the fluorescence it was necessary to maximize the dynamic range of the HPD by changing the high voltage. The fluorescence data were taken at the highest possible and the Čerenkov data at the lowest possible high voltage applied to HPD.

Consequently it was necessary to determine the conversion factor from ADC counts to photoelectrons $\frac{\langle r \rangle}{f_{conv}}$ as a function of high voltage. This can be done by two methods.

The first procedure is the following. LED is used as a stable light source and the intensity is adjusted so that individual photoelectrons are visible. At the high voltage used for the fluorescence measurement the N_{pe} is determined. While keeping the N_{pe} constant the $\langle s \rangle_{ADC}$ is measured at several high voltage values.

In the lower part of the high voltage range, where the peaks can no longer be clearly resolved the light intensity was raised to simulate the Čerenkov light intensity and the dependence was measured to the lowest high voltage point. The two series are plotted in Fig. 47, the low voltage points were scaled down to match the higher voltage points. Second order polynomial fit accounts for the slight nonlinearity of the plot and yields 44.6 ADC/photoelectron at the high voltage used for the Čerenkov measurement.

Another way is to use the Čerenkov signal from the beam with two different intensities monitored by the scintillation palette. Low intensity beam gives the HPD signal at the high voltage used in the fluorescence mode with individual photoelectron peaks. High intensity signal measured with the high voltage set to the value used in the Čerenkov mode yielding the signal in ADC counts. For the ratio of the HPD and scintillator signals

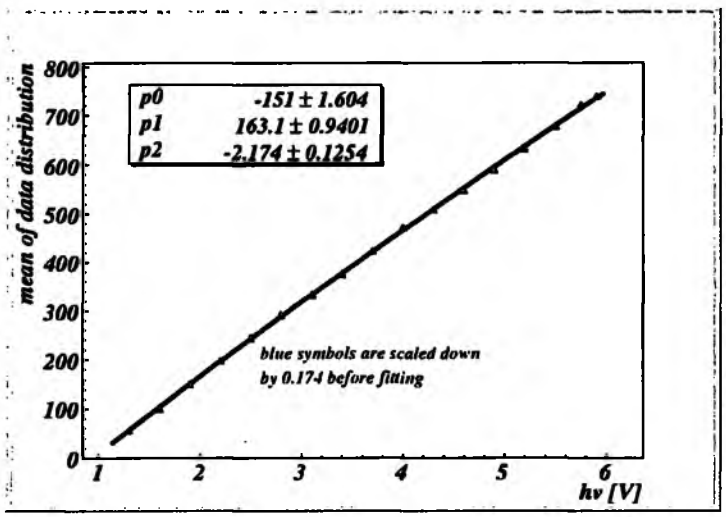

Fig. 47. *Dependence of the mean of the data distribution on the HPD high voltage.*

it holds

$$\frac{Sig_{cere}[adc]/Cf_{cere}}{Sig_{fluo}[p.e.]} = \frac{Pal_{cere}}{Pal_{fluo}}$$

where Sig_{cere} is the HPD signal in Čerenkov mode measured in ADC counts and Sig_{fluo} is the signal at fluorescence like intensity in photoelectrons, Pal_{cere} and Pal_{fluo} are the corresponding beam intensities measured by the scintillator and Cf_{cere} is the conversion factor from ADC counts to photoelectrons in the Čerenkov mode. The measurement was done several times resulting in an average conversion factor of 42.1 ADC/photoelectron.

Averaging the two numbers yields a conversion factor $Cf_{cere} = 43.4 \pm 1$ ADC/photoelectron.

11 Results and discussion

The following three sections describe the results of the relative measurements of the 337 nm line fluorescence yield dependence on pressure, temperature and primary energy. The photon counting method was used but the FLY is given in arbitrary units.

11.1 Pressure dependence

The pressure dependence was measured in LNF, Frascati in the range of 4 to 1000hPa in dry air (78% nitrogen, 21% oxygen, 1% argon) and at 18°C. The electron beam energy was set to 350MeV and the intensity was about 2000 particles per bunch. A typical signal was about 0.05photoelectrons/e^-, the background level reached 10% of the signal. Results are plotted in Fig. 48.

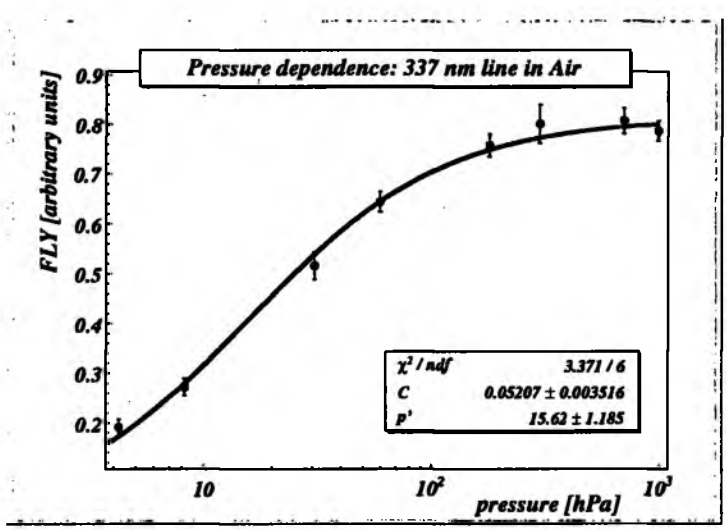

Fig. 48. *Pressure dependence of the* 337 nm *line in air.*

The number of photoelectrons was obtained by the simulated annealing backpulse fitting method discussed in chapter 9, the background was subtracted and the signal was normalized for the beam intensity by the signal from the plastic scintillator. Further, the values have to be corrected for the changing energy deposit due to the limited field of view. The relevant correction function was shown in Fig. 31 in the simulation chapter. The same correction can be used for the measurements in nitrogen because the energy

deposit in air and nitrogen is very similar. The errors were calculated using the following formula (derivation of the statistical error of a Poisson distribution was done in chapter 9)

$$\sqrt{\frac{N_{pe}}{N_{trig}} + \frac{Bkg}{N_{trigbkg}} + (2\% N_{pe})^2},$$

where N_{pe} is the number of photoelectrons measured, Bkg is the level of background (i.e. with the shutter closed), N_{trig} and $N_{trigbkg}$ refer to the number of bunches measured for each signal and background. The last term corresponds to the systematic error, which includes the fact that the signal and the background data were taken one after the other so that the level of background may change, also the beam position and shape may change slightly from run to run. Some uncertainty is introduced by the HPD fitting method and also inaccuracies in the simulation of the energy deposit have to be taken into account. These effects have been estimated to amount to 2 %.

The data were fitted by the model for Y_{fl} valid for constant temperature

$$Y_{fl}(p) = \frac{Cp}{1 + \frac{p}{p'}}, \tag{67}$$

presented in the section 6.2.

Comparison of our results with the previous experiments is given in the following table. An alternative way of deriving the p', used in reference [Walo6] is to measure the decay time of the 2P(0,0) level depending on the pressure. This method does not require a correction on the changing energy deposit.

$p'_{2P(0,0)}$ (hPa)	Bunner [Bun67]	Nagano [Nago4]	Waldenmaier [Walo6]	This work
$Air(FLY)$	$20^{+2.6}_{-6.6}$	19.2 ± 0.7	–	15.6 ± 1.2
$Air(lifetime)$	–	–	15.30 ± 0.13	–

Tab. 5. *Comparison of measurements from several experiments.*

A value of $p' = 18.7 \pm 1.3$ hPa, comparable to the first two experiments in Tab. 5 was obtained for this work, when the correction on the changing energy deposit was not applied.

11.2 Temperature dependence

The temperature dependence of FLY was measured in the range from −35 to 18.5 °C using the thick-wall chamber cooled by liquid nitrogen.

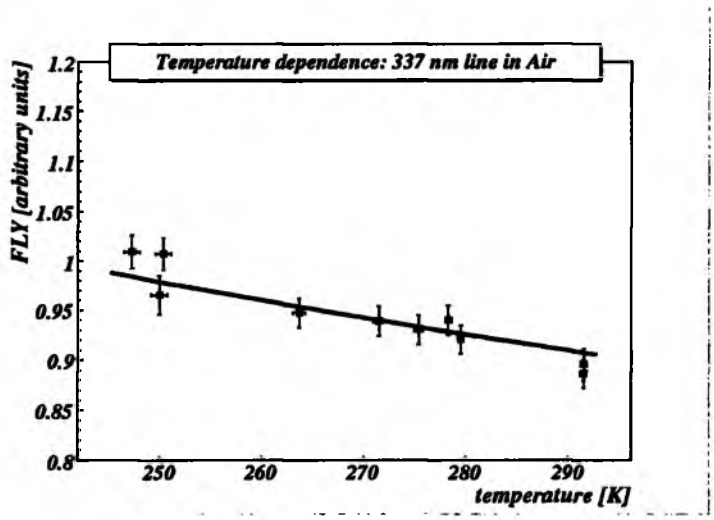

Fig. 49. *Temperature dependence of the* 337 nm *line in air.*

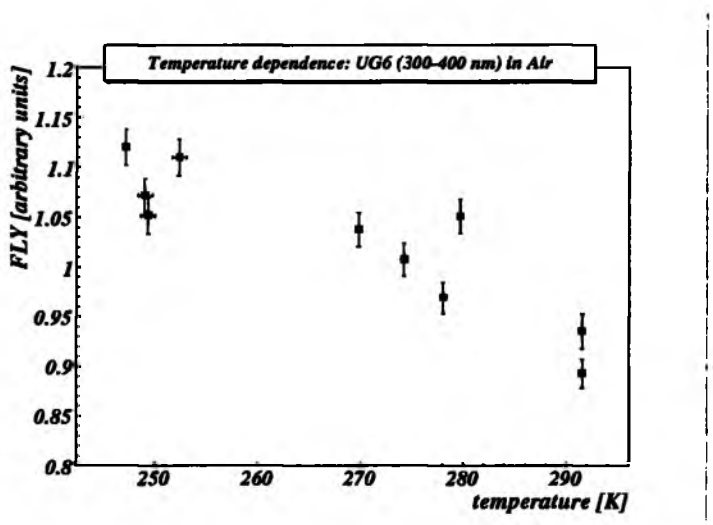

Fig. 50. *Temperature dependence of the region* 300 – 400 nm *(UG6 filter) in dry air.*

This temperature interval corresponds to altitudes from ground level up to about 9 km. The electron beam energy was set to 173 MeV to allow higher intensity of the beam. The same dry air was used as in the pressure measurement.

This measurement was done using the 337 nm interference filter and also UG6 filter (300 – 400 nm). The chamber was cooled down to the lowest achievable temperature and the measurement was done during the spontaneous reheating. Measurement of one temperature point took typically several minutes – the change of temperature during this time is represented by the error-bars in x-direction in Fig. 49 and Fig. 50. The model fitted to the data in Fig. 49

$$Y_{fl}(T) = \frac{C\rho_0}{1 + \sqrt{\frac{T}{T_0}}\frac{p_0}{p'(T_0)}} \tag{68}$$

was derived from (67) and the state equation under the assumption of constant density. The values $\rho_0 = 1.205\,\mathrm{mg\,cm^{-3}}$, $p_0 = 1000\,\mathrm{hPa}$, $T_0 = 18°\mathrm{C}$ refer to the nominal conditions. The characteristic pressure $p' = 15.6\,\mathrm{hPa}$ derived in the previous measurement was used. Constant C is the only fitted parameter to match the scale of the model and the data. Statistical and systematic errors were derived in the same way as in the case of pressure dependence measurement. The agreement is fairly good. In the case of UG6 filter the mixture of lines with different characteristic pressures cannot be fitted by a simple model.

The measurement was done for the first time, therefore a comparison with other experiments is not possible.

11.3 Primary energy dependence

The dependence of FLY on the primary particle energy was measured in pure nitrogen in the range 50 to 420 MeV. The beam multiplicity was kept approximately constant at the individual energy points. The UG6 filter was used to study the dependence over the whole fluorescence spectrum. The result is plotted in Fig. 51. The points were scaled down to relate to the restricted energy loss curve corresponding to our field of view. Errors were derived in the same way as for the pressure dependence measurement. Gas impurity presents an additional source of systematic error.

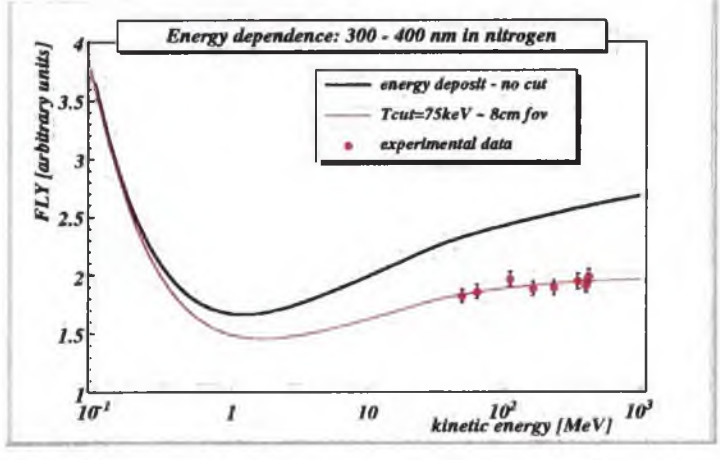

Fig. 51. *Dependence of FLY in nitrogen on the primary particle energy in the region* 300 – 406 nm.

The relative FLY exhibits proportionality to the energy deposit.

11.4 Absolute fluorescence yield

The idea is to measure the absolute fluorescence emission of the most prominent line – 2P(0,0) 337 nm by a special technique and then to measure the whole spectrum using the spectrophotometer and normalize it to this one line in order to determine the absolute yield in the whole fluorescence region.

A new technique is introduced for the determination of the 337 nm line absolute fluorescence yield that has the advantage of reducing the systematic error due to the detector calibration. The principle is to compare the measured FLY to a well known process – the Čerenkov emission. By remotely inserting a thin mylar mirror at an angle of 45° into the beam the Čerenkov light is redirected into the detector and fully dominates over the fluorescence (see Fig. 52). The absolute value of FLY is then determined as a ratio of the signal measured in the fluorescence to Čerenkov configurations from the following equations:

$$\begin{array}{cccccccccc} \underbrace{N_{337}(fluo)} & = & \underline{Y_{fl}} & \times & \underbrace{Geom_{fluo}} & \times & \underbrace{T_{filter} \times QE_{337}} & \times & \underbrace{N_{e^-}} \\ \overbrace{N_{337}(cere)} & = & \overbrace{Y_{cere}} & \times & \overbrace{Geom_{cere}} & \times & \overbrace{T_{filter} \times QE_{337}} & \times & \overbrace{R_{mirror}} & \times & \overbrace{N_{e^-}} \end{array} \quad \begin{array}{c} measured \\ known \\ MC \\ \sim cancel \\ measured \\ relative \end{array} \tag{69}$$

The Čerenkov yield is known from the theory, the apparatus geometrical factors $Geom_{fluo}$ and $Geom_{cere}$ are derived from the full Geant4 simulation of the detector. Relative number of incident electrons is measured by the plastic scintillator. The filter transmittance T_{filter} and the detector quantum efficiency QE_{337} are identical in both configurations and therefore cancel. The mylar mirror reflectivity R_{mirror} was measured and reported in the previous chapter.

In the simulation, the fluorescence yield was set to 19photons/MeV deposited in a step sampled from the spectrum of Bunner [Bun67]. This number leads to 4.74 photons/m/e^- at 350 MeV in 1 m^3 of air or 1.24 photons/m/e^- at 337.1 nm line in the same volume (4.17 photons/m/e^- between 300 – 400 nm). The 337.1 nm line then forms 26.2 % of the total number of photons. As the filter transmittance strongly depends on the incidence angle and the distributions of incident angles in the fluorescence and Čerenkov case differ significantly these effects have to be included in the simulation of the geometrical factor. The analytical formula for the Čerenkov process is included in the GEANT4 [GEA04].

The resulting FLY of the 337 nm line is derived as

$$Y_{fl} = \underbrace{\frac{N_{337}(fluo)}{Sig_{337}(cere)} \times Cf_{cere}}_{R_{meas}} \times \frac{N_{e^-}(cere)}{N_{e^-}(fluo)} \times \frac{1}{R_{sim}} \times Y_{init}, \tag{70}$$

where $N_{337}(fluo)$ is the measured fluorescence signal in photoelectrons, $Sig_{337}(cere)$ is the measured Čerenkov signal in ADC counts and Cf_{cere} is the conversion factor from

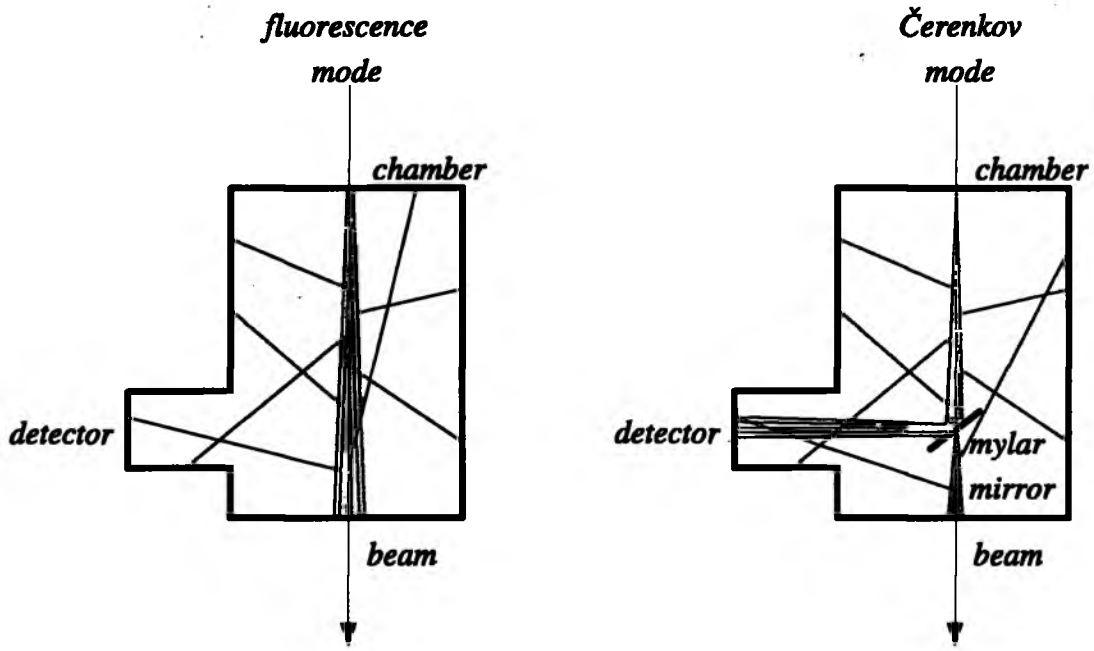

Fig. 52. *Setup for the measurement of the absolute FLY. Remotely controlled mirror allows to switch between Čerenkov and fluorescence modes without beam interruption.*

ADC counts to photoelectrons derived in the previous chapter. The ratio $\frac{N_{e^-}(cere)}{N_{e^-}(fluo)}$ is measured by a fast scintillator. The ratio of fluorescence to Čerenkov signals obtained from simulations $R_{sim} = 1.330 \times 10^{-3}$ is proportional to the Y_{init} (which enters the simulation). The measured ratio $R_{meas} = 1.10 \times 10^{-3}$.

The preliminary absolute fluorescence yield derived at 993 hPa and 18 °C is

$$19\,\text{ph/MeV} \times 26.2\,\% \times 1.10/1.330 = 4.12\,\text{ph/MeV}\,. \tag{71}$$

The quantity 19ph/MeV and the relative spectrum is contained also in the simulated ratio R_{sim} and the two occurrences cancel, therefore the resulting FLY does not depend on the choice of initial values. The value for FLY of the 337 nm line at sea level reported by Bunner [Bun67] is 4.32 ph/MeV deposited. The two results are in fairly good agreement.

The ratio of the fluorescence yield in nitrogen and air measured at the 337 nm line was found to be

$$\frac{Y_{fl}(337)_{N_2}}{Y_{fl}(337)_{Air}} = 7.75. \tag{72}$$

Discussion of systematic errors

Many tests and simulations were done in order to understand the systematic uncertainties of the absolute measurement. The measured background was very small – about

(0.006 ± 0.001) p.e./bunch and amounted to about 10 % of the fluorescence signal. In the Čerenkov case the background is negligible so the uncertainty introduced by the background subtraction is 2 %. The beam intensity normalization is a relative quantity. The statistical error is negligible. The uncertainty of 1 % assigned to this aspect accounts for the possible nouniformity in the plastic scintillator response.

The HPD fitting method uncertainty stems from the fact that the merit function has a broad minimum causing that a slight change in the fitted parameters will lead to a slightly different number of photoelectrons but the quality of the fit will stay the same. This effect was estimated at 3 %. HPD calibration, mirror reflectivity and filter transmittance were already discussed in the previous sections. Systematic effect caused by a slight misalignment of the detector components was studied in simulations (see section 8.3). The photocathode nonuniformity is currently under study. The photocathode coverage differs significantly between the fluorescence and Čerenkov case so any radial nonuniformity could influence the ratio in a substantial way. Therefore the largest systematic error was assigned to it. The effects taken into account are summarized in table Tab. 6.

background subtraction	2%
beam intensity normalization	1%
beam position and spotsize	1%
geometry (misalignment)	4%
HPD fitting method	3%
HPD calibration (ADC/p.e.)	2.3%
simulation (model)	2%
45° mirror reflectivity	1.2%
337 nm filter transmittance	2%
photocathode uniformity and angular dependence	5%

Tab. 6. *Systematic errors of the absolute fluorescence yield measurement.*

Contamination by the 333.9 nm line is below 1 %. Also the contribution of transition radiation from the mirror was found to be negligible.

Statistical error amounts to 1.5%. It was derived in the following way. The whole data set was divided into k parts and each part was analyzed separately. Standard deviation of the results thus obtained should be a factor $1/\sqrt{k}$ larger with respect to the standard deviation of the average. Values $k = 5$ and 10 were used to verify that measurements follow the statistical distribution expected.

As the contributing uncertainties are uncorrelated they were added in quadrature and the resulting error to be assigned to the absolute intensity of the 337 nm line is 8.5 %.

11.5 Nitrogen spectrum

The fluorescence spectrum was measured in the spectrometer setup described in the previous chapters. Electron beam of 3 MeV was operated in DC mode and the average beam current of 10 μA. The spectral response and spectral sensitivity calibration was performed using the mercury and halogen lamp measurements described in chapter 7. The background level was estimated in the regions where no lines were observed and then linearly interpolated to the regions with lines. The calibrated and background subtracted spectrum obtained for dry air with argon (78 % nitrogen, 21 % oxygen, 1 % argon) at 800 hPa and the temperature 20 °C (293 K) is shown in Fig. 53.

The lines that could be resolved are listed in Tab. 7 together with their intensity relative to the 337 nm line.

The line intensities were obtained by integration of the CCD counts in an interval around each line. In some cases, where the lines are close together, a part of the rotational band will be assigned to the previous line. For spectroscopic purposes the correct procedure would be to try to extract the contamination of other lines and assign it to the correct one. However, for the fluorescence detection technique the quantity of interest is the amount of light emitted into a certain wavelength interval. Therefore the adopted procedure was to divide the spectrum into intervals of about 2nm around the main lines and the integration was done within these intervals.

Typically about 2 % difference was found in the intensities of the lines in the overlapping region. This can be attributed to a small beam intensity change between the first and the second part of measurement. The ratio of the common line intensities was used to correspondingly normalize the second measured range.

The bulk of the data was obtained by summing eleven consecutive runs taken at the same conditions. Statistical error was than found by separate analysis of each of the eleven runs (standard deviation of the values obtained). The intensities found for each individual line were histogrammed and RMS of the distribution was used as the estimate of the statistical error.

To obtain the total error given in Tab. 7 a common systematic error of 3.5 % was added in quadrature. This accounts for the absolute lamp calibration uncertainty (2.5 %), the difference of the mercury lamp line intensities observed in the overlapping regions (2 %) and the uncertainty related to the spacial distribution of the fluorescence light and the corresponding calibration procedure.

Absolute Fluorescence Yield at 300 – 406 nm

To derive the absolute fluorescence yield in the wavelength region used by the fluorescence detectors the relative line intensities in this region have to be summed up and

wavelength [nm]	system	(ν', ν'')	intensity I_λ/I_{337} [%]
296.2	$2P$	(3, 1)	5.43 ± 0.43
297.7	$2P$	(2, 0)	2.87 ± 0.23
302.1	Gaydon-Herman	(6, 2)	0.46 ± 0.12
308.2	Gaydon-Herman	(5, 2)	1.47 ± 0.14
311.7	$2P$	(3, 2)	7.42 ± 0.32
313.6	$2P$	(2, 1)	10.94 ± 0.41
315.9	$2P$	(1, 0)	39.32 ± 1.4
326.8	$2P$	(4, 4)	0.81 ± 0.09
328.3	Gaydon-Herman	(0, 3)	3.85 ± 0.14
330.9	$2P$	(2, 2)	2.14 ± 0.11
333.9	$2P$	(1, 1)	4.07 ± 0.17
337.1	$2P$	(0, 0)	100
346.3	Gaydon-Herman	(0, 4)	1.81 ± 0.09
350.1	$2P$	(2, 3)	2.87 ± 0.16
353.7	$2P$	(1, 2)	21.32 ± 0.77
357.7	$2P$	(0, 1)	67.33 ± 2.36
365.9	not identified		1.12 ± 0.06
367.2	$2P$	(3, 5)	0.49 ± 0.15
371.1	$2P$	(2, 4)	4.98 ± 0.22
375.5	$2P$	(1, 3)	17.93 ± 0.65
380.5	$2P$	(0, 2)	27.30 ± 1.0
391.4	$1N$	(0, 0)	30.70 ± 1.08
394.3	$2P$	(2, 5)	3.43 ± 0.2
399.8	$2P$	(1, 4)	8.60 ± 0.34
405.9	$2P$	(0, 3)	8.35 ± 0.3
414.2	$2P$	(3, 7)	0.51 ± 0.11
420.1	$2P$	(2, 6)	1.78 ± 0.13
423.7	$1N$	(1, 2)	1.07 ± 0.07
427.0	$2P$	(1, 5)	7.25 ± 0.25
427.8	$1N$	(0, 1)	4.82 ± 0.17

Tab. 7. *Emission lines resolved in the nitrogen spectrum.*

normalized according to the absolute FLY determined for the 337 nm line. For the value derived in the previous section, FLY in the wavelength region $300 - 406$ nm amounts to 15.74 ph/MeV. In order to be comparable to other experiments this value can be expressed in the units of photons/m/e^- at 350 MeV, at atmospheric pressure and 293 K

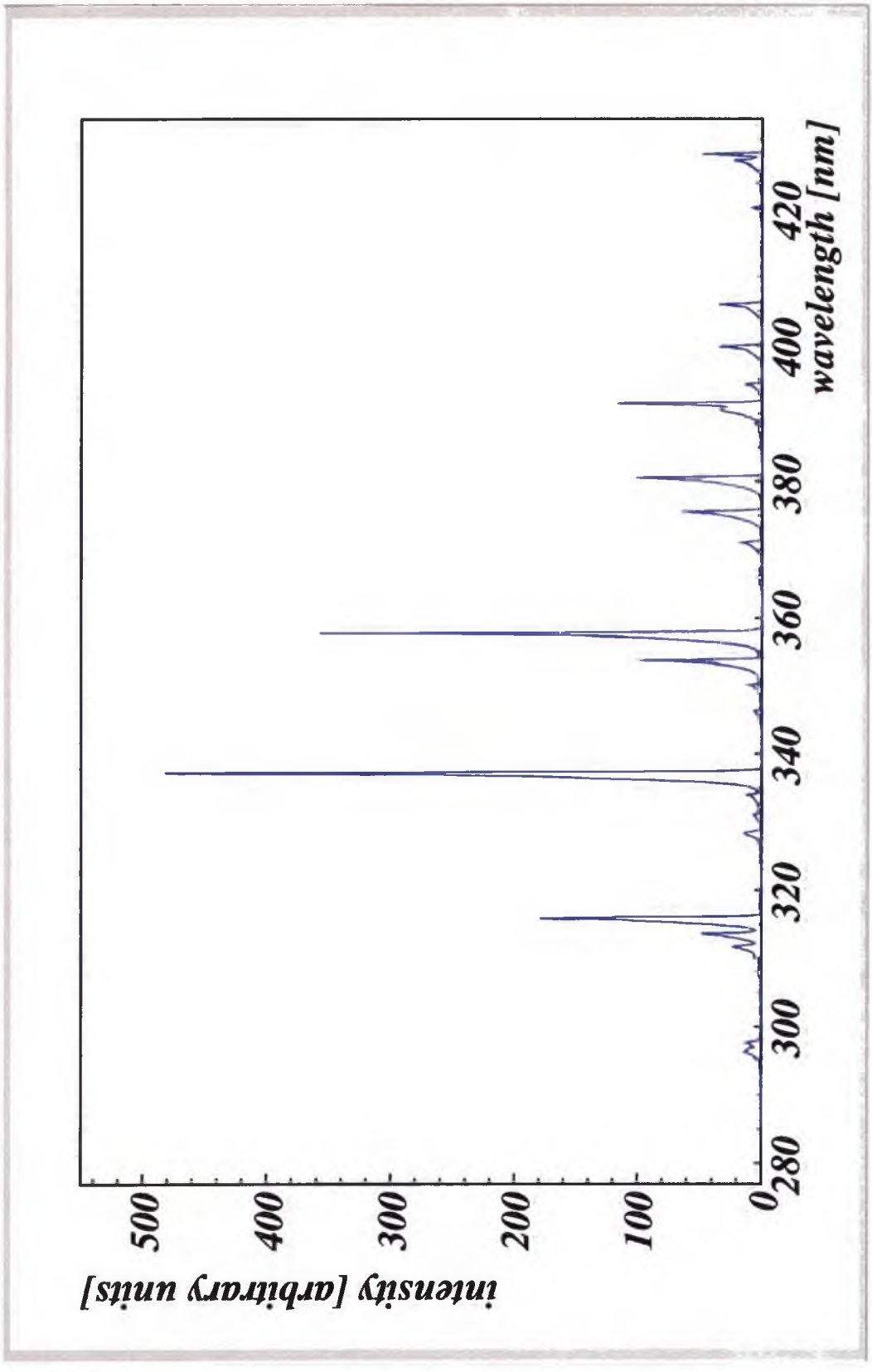

Fig. 53. *Measured nitrogen spectrum at 800 hPa in ultrazero air (79% nitrogen, 21% oxygen). Measured relative intensities together with the total error are given.*

simply by multiplication by the relevant density and energy loss. At $\rho = 1.205\,\mathrm{mg/cm^3}$ and $\mathrm{d}E/\mathrm{d}x(350\,\mathrm{MeV}) = 2.567\,\mathrm{MeV/g\,cm^2}$ (ESTAR) the FLY would be

$$Y_{fl}(1012\,\mathrm{hPa;\,air}) = 4.86\,\mathrm{photons/m/e^-} \tag{73}$$

Errors of all the lines were regarded as uncorrelated and therefore could be added in quadrature. The resulting total error amounts to 9.15%.

Comparison with other experiments is given in Fig. 54. The scale on the right was adjusted so that the energy loss curve meets the data point of AIRFLY.

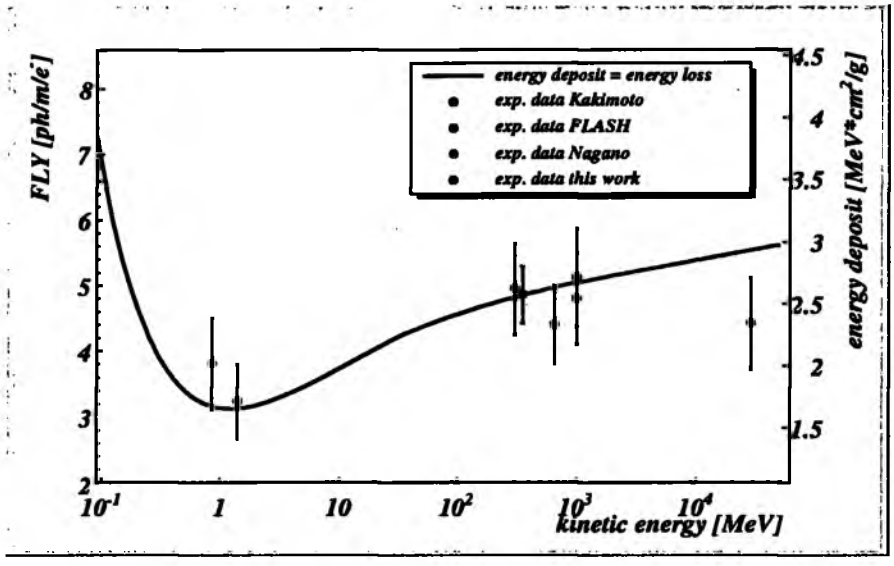

Fig. 54. *Absolute fluorescence yield in the region 300 - 406 nm (UG6 filter) given by Nagano et al. [Nag04], Kakimoto et al. [Kak96] and Belz et al. [Bel06] and this work.*

11.6 Implications on the cosmic ray energy spectrum

At this point it is possible to asses the impact that the results presented would have on the measured cosmic ray energy spectrum. The model used so far in the analysis of the Auger fluorescence detector data is the fluorescence model given by Nagano [Nag04]. The main difference was found for the absolute fluorescence yield of the 337 nm line. Minor effects can be contributed by the other lines from the 300 – 406 nm region. Alteration of the energy spectrum due to the smaller p' is more complicated, however it is expected to be small.

The absolute fluorescence yield of 300 – 406 nm reported by Nagano at 0.85 MeV is 3.81 ph/m/e$^-$ (at 20 °C and 1 atm) The value obtained for this work is 15.74 ph/MeV deposited (at 350 MeV). Supposing that the fluorescence yield per deposited energy is

constant, this value can be simply multiplied by the density of air at 20 °C and 1 atm and by the energy loss of 0.85 MeV electrons in air $\mathrm{d}E/\mathrm{d}x(0.85\ \mathrm{MeV}) = 1.677\ \mathrm{MeV/g\,cm^2}$. The resulting value $3.18\,\mathrm{ph/m/e^-}$ is about 20 % lower then the absolute fluorescence yield given by Nagano.

The shift of 20 % in the absolute fluorescence yield would translate directly into the increase of the primary energy estimation. The Fig. 55 shows the cosmic ray energy spectrum of the AUGER experiment as it was presented on the ICRC 2005 [Somo5] together with the results of the surface array AGASA. The black points indicate the 20 % shift in energy.

The energy spectrum of HiRes (another major fluorescence detector) will not be affected by the presented results as this experiment has been using the model of Kakimoto, which is in good agreement with this work.

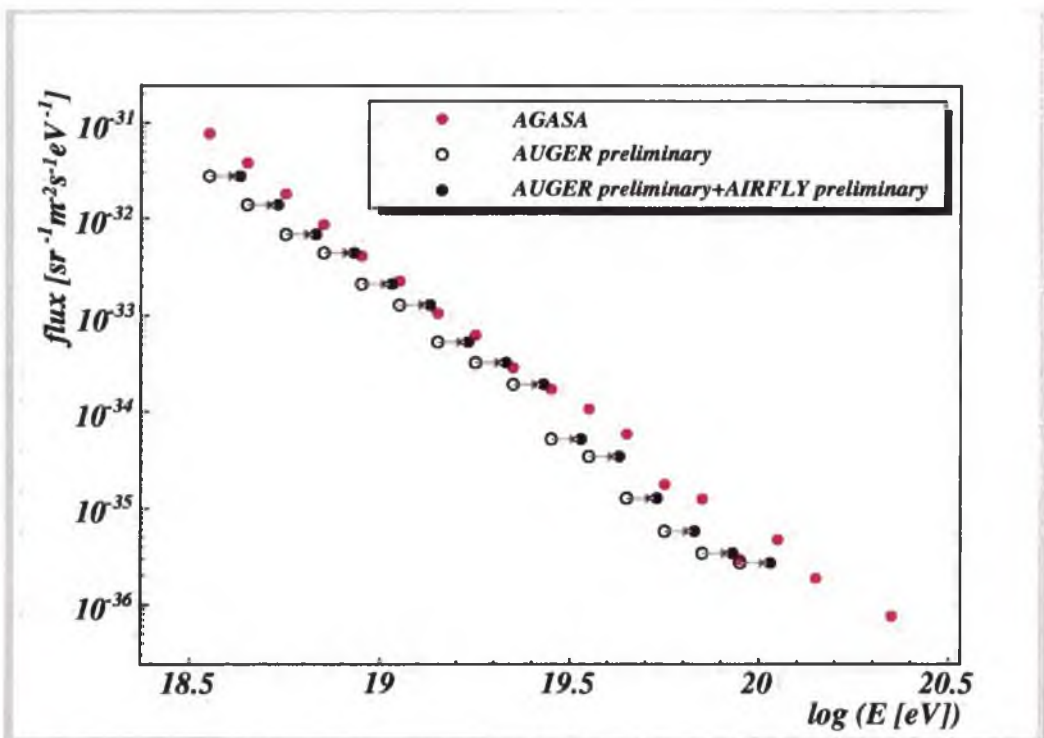

Fig. 55. *Estimate of the effect of 20% energy shift on the cosmic ray energy spectrum.*

11.7 Pressure dependence of the nitrogen spectrum

Last measurement included here presents the dependence of the whole fluorescence spectrum on the varying pressure as is illustrated in Fig. 56. The measurement was performed in artificial air (79 % nitrogen, 21 % oxygen) at 13 pressure points.

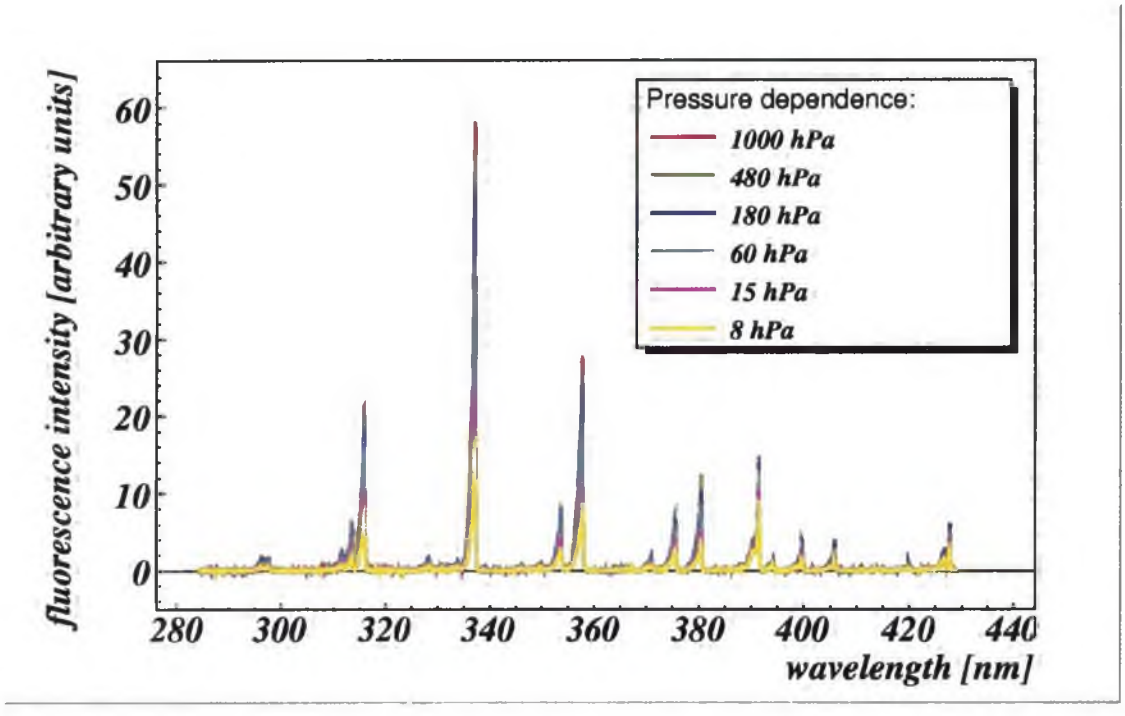

Fig. 56. *Pressure dependence of the total measured spectrum.*

Using the ratios of the individual lines to the 337 nm line at each pressure point it is possible to derive the characteristic pressure p'_λ for each line. The advantage of this method is that, as the lines are being populated at the same time, systematics due to variations of the beam intensity or different integration times are eliminated.

The intensity ratios for 14 strongest lines belonging to four vibrational systems are plotted in Fig. 57, Fig. 58, Fig. 59 and Fig. 60. The fitted function reads

$$\frac{I_\lambda}{I_{337}} = C \frac{1 + \frac{p}{p'_{337}}}{1 + \frac{p}{p'_\lambda}}, \tag{74}$$

where the characteristic pressure $p'_{337} = 15.6\,\mathrm{hPa}$ is set to the value derived in section 11.1.

Lines originating in the same vibrational level should feature the same pressure dependence, i.e. their p' should be the same. This statement has been verified for the four

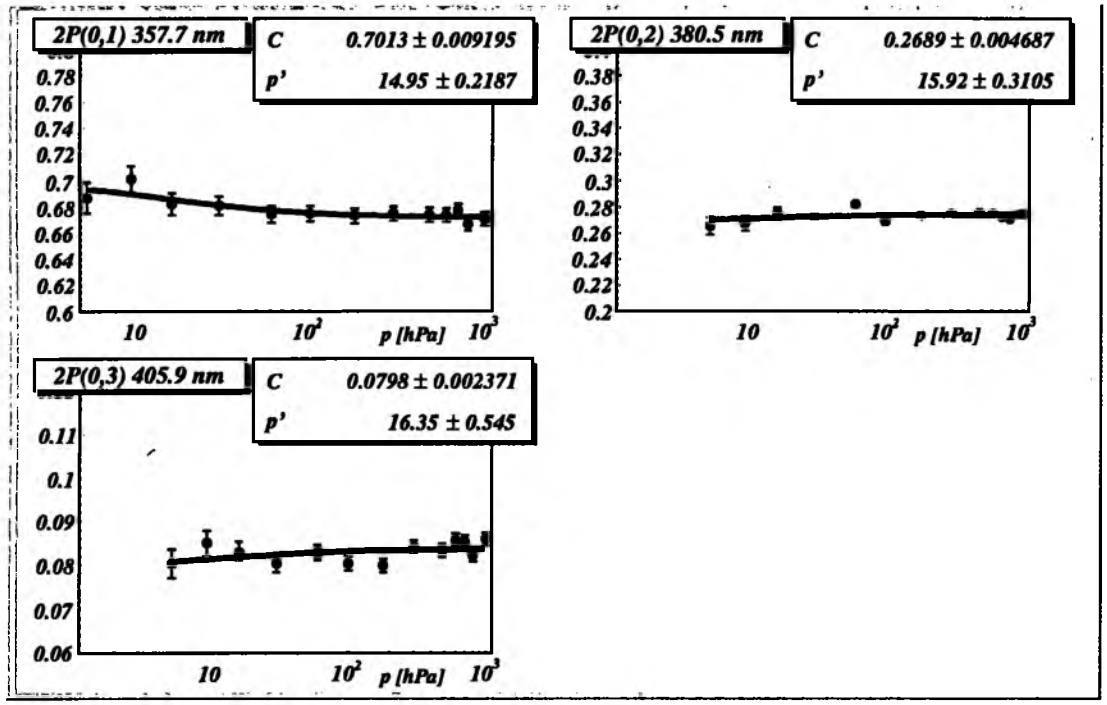

Fig. 57. *Pressure dependence of the ratios of 2P(0,ν) lines (zeroth vibrational level) to the 2P(0,0) line.*

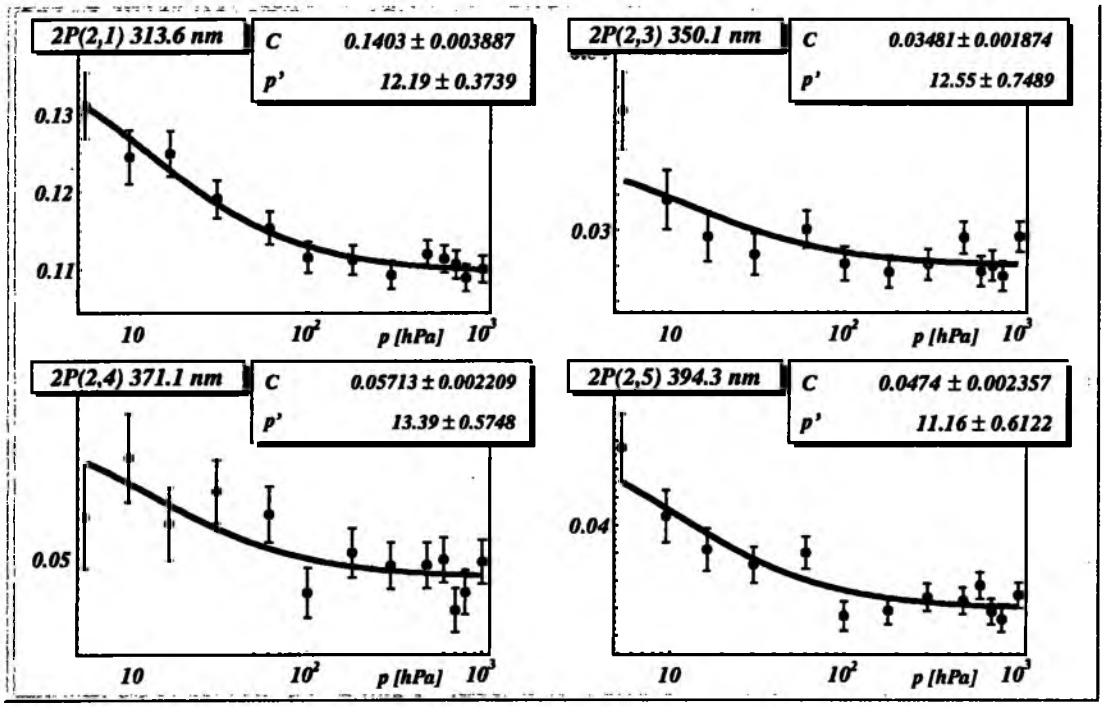

Fig. 58. *Pressure dependence of the ratios of 2P(2,ν) lines (second vibrational level) to the 2P(0,0) line.*

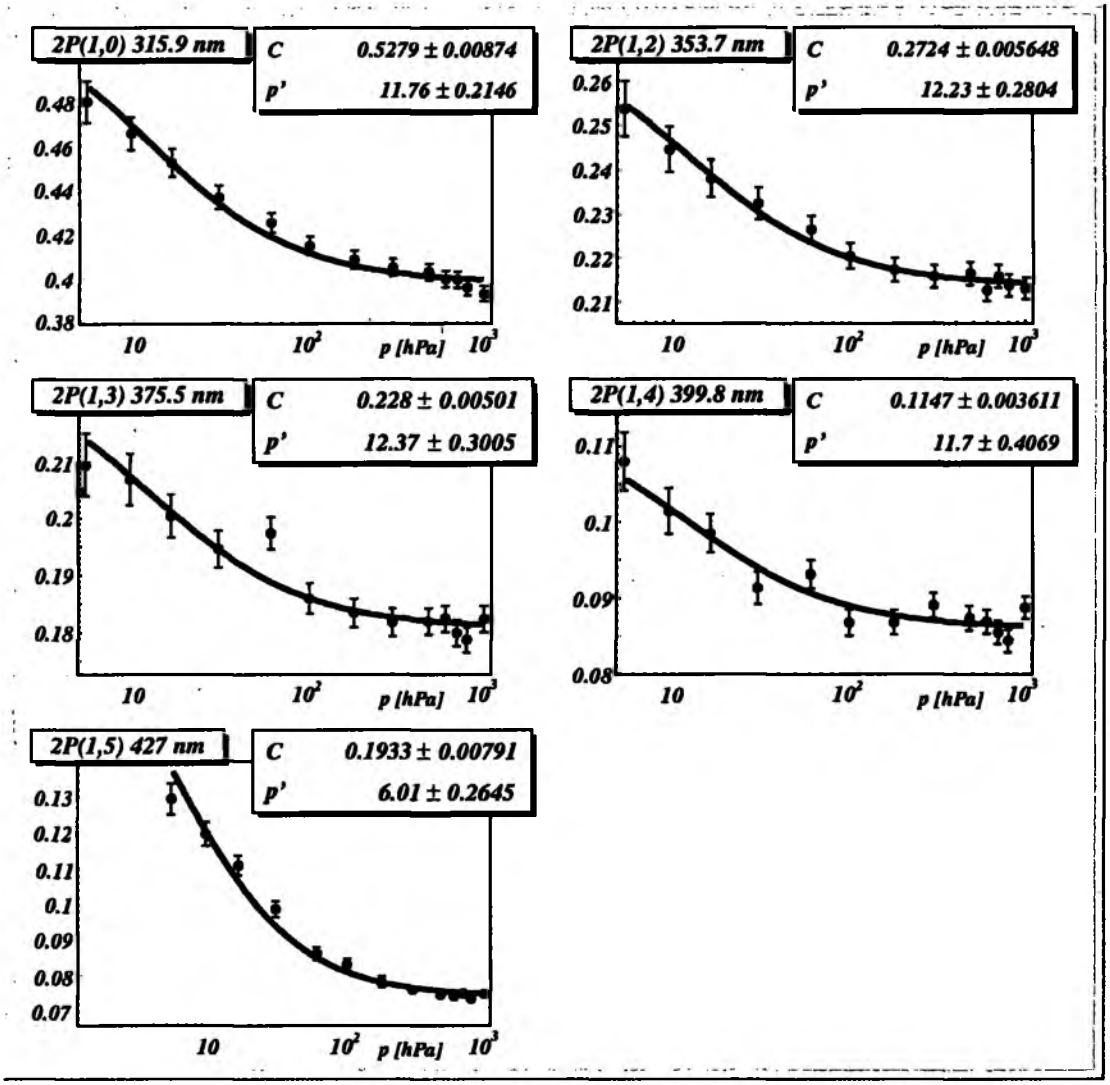

Fig. 59. *Pressure dependence of the ratios of 2P(1,ν) lines (first vibrational level) to the 2P(0,0) line.*

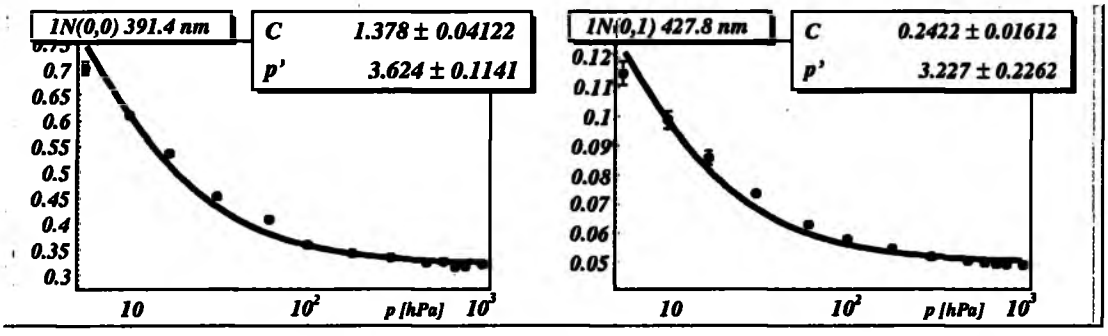

Fig. 60. *Pressure dependence of the ratios of 1N(0,ν) lines (zeroth vibrational level) lines to the 2P(0,0) line.*

vibrational systems shown. The resulting characteristic pressures agree within the error stated apart from the 2P(1,5) 427 nm line, which is strongly contaminated by the rotational levels of the nearby line 1N(0,1) 427.8 nm. For spectroscopic purposes the two lines should be separated to derive correct value for each line. However, in the determination of the air shower fluorescence intensity it is desirable to characterize the pressure dependence in a certain wavelength interval, rather than for each line.

12 Conclusions

Air fluorescence technique is one of the two major methods of detection of the cosmic ray air showers. Recent technological progress has helped to improve the precision of the detection to the extent that the largest systematic error presently comes from the limited knowledge of the details of the fluorescence emission. Experiment AIRFLY has been set up to verify the fluorescence parameters used so far and to improve the precision of measurements to meet the requirements of the future fluorescence detectors.

This work presents an analysis of a subset of data from the AIRFLY experiment taken in LNF Frascati, Italy and ANL Argonne, USA.

Frascati measurements include: measurement of the pressure dependence of the 337 nm line in air in the range 4 – 1000 hPa, temperature dependence of the 337 nm line and of the 300 – 400 nm region in the range −35 °C to 18.5 °C, dependence on the energy of the primary particle in nitrogen in the range 50 – 420 MeV and the absolute fluorescence yield of the most prominent line in the spectrum (337 nm). Measurement of the air fluorescence spectrum between 290 – 430 nm was performed in Argonne.

Great attention was given to the analysis of the function of the principal photodetector – the Hybrid Photo Diode starting from the modeling of the response to individual photoelectrons and ending by the implementation of the fitting algorithm.

Total Monte-Carlo simulation of the experiment was performed in GEANT4. Parameters of the experimental setup as well as the beam properties were varied in order to optimize the experimental setup and to estimate the systematic errors. The geometrical factors involved in the absolute fluorescence yield determination were simulated.

The dependence on the pressure was found to agree with the model dominated by collisional quenching with the characteristic pressure $p'_{337} = 15.6$ hPa. This value is then used to determine characteristic pressures of other lines from the spectrum.

Temperature dependence was measured for the first time and was found to agree with the theoretical expectation. In the range of temperatures relevant for the air shower measurements the decrease of air fluorescence with increasing temperature amounts to $\sim 10\,\%$.

In the energy range measured the fluorescence yield was found to be proportional to the energy deposit.

A new method was used to determine the absolute fluorescence of the 337 nm line, in which the fluorescence yield is compared to a well known process – the Čerenkov radiation.

The value $Y_{fl} = 4.12 \pm 0.35$ ph/MeV of energy deposit was obtained at 993 hPa and 18 °C. In nitrogen this value would be 7.75 times larger.

The whole spectrum was measured using 3 MeV continuous beam. In the range 290 – 430 nm 30 lines were resolved.

In the range observed by the fluorescence detectors, i.e. 300 – 406 nm the lines were normalized by the 337 nm line absolute yield and summed up. The resulting fluorescence yield is 15.74 ± 1.44 ph/MeV of energy deposit. The total error amounts to 9.15 %.

This value, expressed at photons per metre per electron at the sea level, 20 °C and 0.85 MeV yields 3.18 ph/m/e^-, which is about 20 % lower with respect to the Nagano value currently used by the Auger collaboration.

In order to take into account correctly all the new measurements the Auger data have to be reanalyzed with the new values, however an estimate can be made that the 20% shift in energy of the showers will bring the spectrum of Auger closer to the AGASA measurement.

Future prospects

Future effort of the AIRFLY collaboration will be directed at the final verification of the results presented here. The systematic error quoted can be reduced by a better beam stability. The photocathode nonuniformity is planned to be eliminated by the insertion of an integrating sphere in front of HPD so that the photons arriving to the photocathode would be uniformly distributed in both (Čerenkov and fluorescence) cases.

Bibliography

[Abb05] Abbasi R.U. et al. (The HiRes Collaboration): Phys. Lett. B619, 271 (2005)

[Abr04] Abraham J. ... Bohacova M., ...(The Auger Collaboration): NIM A 523, 50 (2004)

[And33] Anderson C. D.: Phys. Rev. 43, 491 (1933)

[Aug38] Auger P., Ehrenfest P., Maze R., Daudin J., Robley, Freon: Rev. Mod. Physics 11, 288-291, 1938

[Aug41] Auger P.: Rayones cosmiques, Presses universitaires de France, Paris 1941

[Bar62] Barrow G.M.: Introduction to molecular spectroscopy, McGraw-Hill, New York, 1962

[Bel06] Belz et al.: Astropart. Physics 25, 129-139 (2006)

[Bet34] Bethe H. A., Heitler W.: Proc. Roy. Soc. A146, 83 (1934)

[Bla48] Blackett P. M. S.: Per. Conf. Gassiot Comm. Phys. Soc., p. 34 Physical Society, London (1948)

[Bru73] Brunet H.: Doctoral thesis, Toulouse 1973

[Bun67] Bunner A.N.: Doctoral thesis, Cornell 1967

[Cah89] Cahn R.N., Goldhaber G.: The Experimental foundation of particle physics, Cambridge University Press 1989

[Cer34] Čerenkov PA.: Dokl. Acad. nauk SSSR, (1934-1938)

[DaO64] Davidson G., O'Neil R.: Jour. of chemical physics 41, (1964) 3946-3955

[Dam82] Bethe Damkjaer A.: NIM 200, (1982) 377-381

[DeS87] De Salvo R.: Cornell University, preprint, CLNS87-92 (1987)

[ESO02] http://www.ls.eso.org/lasilla/sciops/2p2/E2p2M/FEROS/Projects/ADC/references/refraction/index.html

[Fer49] Fermi E.: Phys. Rev., Vol. 75, No. 8, 1169-1174, 1949

[Fie66] Fiedler E.: private communication (1966)

[Fon96] Fons T.J., Schappe R.S., Lin C.C: Phys. Rev. A, Vol. 53, 2239-2247, 1996

[Fra37] Frank I. M., Tamm I.: Dokl. Akad. Nauk, SSSR, 14 (3), 109 (1937)

[GEA04] GEANT4, http://geant4.web.cern.ch/geant4/

[Goc11] Cockel A.: Physik. Zeitschrift XII, (1911)

[Gai77] Gaisser T.K., Hillas A.M.: Proc. 15th ICRC (Plovdiv), 8, 353. (1977)

[Gai90] Gaisser T. K.: Cosmic Rays and Particle Physics, Cambridge University Press, 1990

[Gil92] Gilmore F., Laher R.R, Espy P.J.: Jour. Phys. Chem. Ref. Data 21, p. 1005 (1992)

[Goro6] Gorbunov D.S., Tinyakov, P.G., Tkachev I.I., Troitsky S.V.: JCAP 01, 025, (2006)

[Gre56] Greisen K.: Prog. Cosmic Ray Phys. 3, 1956

[Gre66] Greisen K.: Phys.Rev. Lett., Vol. 16, No. 17, 1966

[GSLo6] GNU Scientific Library, http://www.gnu.org/software/gsl/

[Gyso1] Gys t.: NIM A 465, 240-246, (2001)

[Har82] Harms R. et al: NASA CP-2244 (1982) 55

[Her50] Herzberg G.: Molecular spectra and molecular structure I, Van Nostrand, New York, 1950

[Hes12] Hess V.: Physik. Zeitschr, 13, 1084-1091, (1912)

[Hes68] Hesser J.E.: J. of Chemical Physics 48, 6 (1968)

[Hil72] Hillas A.M.: Cosmic rays, Pergamon Press 1972

[Hil82] Hillas A.M.: J.Phys. G, Vol.8, 1461-1473, (1982)

[Hil84] Hillas A.M.: Ann.Rev. Astron. Astrophys. 22 :425-444, (1984)

[Hil91] Hillas A.M.: Proceedings of the International Symposium on Astrophysical Aspects of the Most Energetic Cosmic Rays, World Scientific 1991

[Hir70] Hirsh M.N., Poss E., Eisner P.N.: Phys. Review A 1, 6, (1970)

[Jel58] Jelley J.V.: Čerenkov radiation and its application, Pergamon Press 1958

[Jor99] Joram C.: Nuclear Physics B - Proceedings Supplements V78 (1999) 407

[Kak96] Kakimoto F., Loh E.C., Nagano M., Okuno H., Teshima M., Ueno S.: NIM A 372, 527-533, 1996

[Kal66] Kalibjian R.: IEEE Trans. on Nuclear Science, V.12, N.4 (1965) 367

[Kew96] Kewley L.J., Clay R.W., Dawson B.R.: Astropart. Physics 5, 69-74, 1996

[Kleo4] Kleifges M.: private communication (2004)

[Kle29] Klein O., Nishina Y.: Zeit. f. Phys., 52 (1929) 853

[Law91] Lawrence M.A., Reid R.J.O., Watson A.A.: J. Physics G, Vol. 17, 733-757, 1991

[Leo94] Leo W.R.: Techniques for Nuclear and Particle Physics Experiments, Springer-Verlag, 1994

[Lin63] Linsley J.: Phys. Rev. Lett., Vol. 10, 1963

[Lof77] Lofthus A., Krupenie P.H.: Jour. Chem. Ref. Data, Vol. 6, No.1 1977

[Long2] Longair M.S.: High Energy Astrophysics, Cambridge University Press (1992)

[Mal29] MalletP.: C.R. Acad. Sci., Paris (1929) 188, 445

[Mazo3] Mazzitelli G., Valente P.: NIM A 515/3, (2003) 516-534

[Met53] Metropolis N., Rosenbluth A., Rosenbluth M., Teller A., Teller, E.: J. Chem. Phys. 21, 1087-1091 (1953)

[Mil47] Millikan R.A.: Electrons, Protons, Photons, Neutrons, Mesotrons and Cosmic Rays, The University of Chicago Press, 1947

[Nag00] Nagano M.,Watson A.A.: Rev. Mod. Physics, Vol. 72, No. 3 , 2000

[Nag03] Nagano M., Kobayakawa K., Sasaki N., Ando K.: Astropart. Physics 20, p. 293-309 (2003)

[Nag04] Nagano M., Kobayakawa K., Sasaki N., Ando K.: Astropart. Physics 22, p. 235-248 (2004)

[NMR92] Press W. H., Teukolsky S. A., Vetterling W. T., Flannery B. P.: Numerical Recipes in C, Second Edition, Cambridge University Press 1992

[Qui96] Quinn J. et al: Ap. J. Lett. 456 (1996) 83

[Pen65] Penzias A.A., Wilon R.W.: Astrophys. Journal 142, 419 (1965)

[PEN06] PENELOPE, http://www.nea.fr/html/dbprog/peneloperef.html

[Per53] Pernegr J., Petržílka V., Tomášková : Kosmické záření,, ČSAS Publishing 1953

[PDG04] Review of Particle Properties, Physical Review, D50, 1173 (1994)

[Ris04] Risse M.: Acta Phys.Polon. B35, 1787-1797 (2004)

[Ros52] Rossi B.: High-energy Particles, MIT 1952

[Ros66] Rossi B.: Cosmic rays, G. Allen & Unwin, London 1966

[Sch02] Schlickeiser R.: Cosmic Ray Astrophysics, Springer 2002

[Som05] Sommers P., (Pierre Auger Collaboration), Proceedings of 29^{th} ICRC, Pune 2005

[Tab97] Tabarelli de Fatis T.: NIM A 385 (1997) 366-370

[TDR02] Technical Design Report, http://tdpc01.fnal.gov/auger/org/tdr/index.html

[USA76] U.S. Standard Atmosphere, U.S. Government Printing Office, Washington, D.C., 1976

[Wal06] Waldenmaier T.: Doctoral thesis, Karlsruhe 2006

[Win86] Winn M.M., Ulrichs J., Peak L.S., McCusker C.B.A., Horton L.: J. Phys. G, Vol. 12, 653-674, 1986

[Wul10] Wulf Th.: Physik. Zeitschr. 11, 811-813, 1910

[Zat66] Zatsepin G., Kuzmin V.: JETP Lett. 4, p. 78-80 (1966)